Development and Experimental Validation of Dynamic Bayesian Networks for System Reliability Prediction

by

Kaihua Zhang

A dissertation submitted in partial fulfillment
of the requirements for the degree of
Doctor of Philosophy
(Naval Architecture and Marine Engineering)
in The University of Michigan
2020

Doctoral Committee:

Associate Professor Matthew D. Collette, Chair
Professor John Allison
Professor Pingsha Dong
Associate Professor Kevin Maki
Associate Professor David Singer

Kaihua Zhang

kaihua@umich.edu

ORCID iD: 0000-0003-4122-2112

ACKNOWLEDGEMENTS

Foremost, I would like to express my deepest gratitude to my advisor Dr. Matthew Collette for continuously supporting my Ph.D. research, for his mentorship, patience, and motivation which significantly helped me all the time of research. Dr. Collette is not only my advisor but also my role model. He is positive, calm, and confident, which has brought invaluable influence to me in my development. Dr. Collette has been tremendously supportive in my experiment exploration, graduate study, and career opportunities. I'm always thinking that I'm extremely lucky working with Dr. Collette for four years. I could not have imagined having a better advisor for my Ph.D. study.

I would like to extend my sincere thanks to the rest of my thesis committee: Dr. John Allison, Dr. Kevin Maki, Dr. Pingsha Dong, and Dr. David Singer for their insightful comments and brilliant suggestions. I'm also grateful to Dr. John Lasecki for his help in conducting the fatigue experiment. Besides, I would like to recognize the support of Dr. Paul Hess of the Office of Naval Research, code 331.

Last but not least, I would like to thank my wife for standing strong beside me and making me look forward to new adventures and challenges. I would also like to thank my parents for supporting me throughout my life.

TABLE OF CONTENTS

CHAPTER

LIST OF FIGURES

Figure

LIST OF TABLES

<u>**Table**</u>

LIST OF ABBREVIATIONS

BN Bayesian Network
DBN Dynamic Bayesian Network
OON Object-oriented Networks
EDM Electrical Discharge Machining
FEA Finite Element Analysis
CV Computer Vision
UV Ultraviolet
CCD Charge-coupled Device
RGB Red, Green, and Blue
FPS Frame per Second
SDK Software Development Kit
DIC Digital Image Correlation
NI National Instrument
DAQ Data Acquisition System
ROI region of interest
CPT Conditional Probability Table
GUI Graphical User Interface
SIF Stress Intensity Factor
RMSE Root Mean Squared Error

ABSTRACT

Vessels and marine structures are subjected to degradation during their service, jeopardizing structural safety and shortening their service life. Numerical models of such structural systems are developed and relied on to simulate and ensure system integrity. Such numerical models are the essential part of digital twins representing complex marine structures and providing enhanced forecasts of risk and lifecycle performance. Digital twins also require data fusion from observations or experiments to improve the numerical model agreement with the real-world structure. Due to the infeasiblity of full-scale testing of marine structures, scale experiments are developed but few of them reflect many of the properties of large and complex marine structures. Thus, an experiment must be designed to mimic the multiple degradation process and retain structural redundancy so that a single element failure will not remove all load carrying capacity. Dynamic Bayesian networks (DBN) expand the Ordinary Bayesian networks (BN) with slices representing the state of the system at different time intervals. DBN can model the degradation process of structure but its performance has not been validated by experiments. Therefore, the PhD research designs an experiment to mimic the properties of marine structure and develops a corresponding numerical model based on DBN whose performance is evaluated by the designed experiment.

To mimic the interdependence, redundancy and component-to-system level performance of marine structures in degradation, a hexagon tension specimen with four propagating fatigue cracks, one on each corner, is designed and tested. The applied loading cycles and corresponding crack lengths are recorded as the major time-varying data of degradation state. Two new methods of measuring crack length are developed based on computer vision and digital image correlation. A standard eccentrically-loaded single edge crack tension specimen is designed and tested to validate the performance of the developed computer vision-based method for measuring crack length. The results of the hexagon experiment demonstrate that the designed specimen successfully simulates the interaction among cracks and structural redundancy. To complement the test specimen, a DBN is constructed to predict the crack length with input observations. The network models the time-varying process of degradation with sequential slices. The task is divided into several steps including the first two steps as modeling single crack propagation with simulated observations, two cracks propagation considering dependence evaluated via simulated observations. The dependence among components are controlled by hyperparameters and are integrated into complex system behavior to reflect the structure from the component level to the system level. Then a DBN model is developed for four cracks propagation with dependence modeled by hyperparameters using Object-oriented Networks (OON) technology and evaluated by data gathered from the hexagon experiment. Finally, the dependence between crack length and stress is modeled in the fourth model based on the technology named Temporal Clone which is also evaluated via experimental data. The experimental data and developed numerical models provide support and guidance in the exploration of digital twin models.

CHAPTER I

Introduction

Structural degradation of vessels and marine structures during their service can jeopardize structural safety and shorten their service lives. Owing to the lack of a physical prototype to test degradation phenomena, efforts are made to develop the numerical models of vessels and marine structures to describe the aging of real-world structural systems and assist in making decisions for maintenance. Such numerical models are known as digital twins representing the complex marine structures and providing an enhanced forecast of risk and lifecycle performance. Digital twins fuse data from observations, experiments or data generated by numerical models to make the model agree with the real-world structure. Numerical models are highly relied upon by engineers, while the common method for validating and evaluating numerical models is using small sets of model-generated data. Usually, the generated data is not independent from the numerical models, which questions the validity of numerical models in real world. Thus, independent experimental data is critical for evaluating the numerical models in digital twin approaches.

Experimental testing of marine structures have been conducted in the past decades in several sub-areas. Individual components of marine structures are tested commonly, determining the component strength and properties. Numerous components experiments can be found, including collapse tests on stiffened panels *Gordo and*

Soares (2008), corrosion experiments on steels plates *Saad-Eldeen et al.* (2016a), fatigue evaluation on welded structural joints of ships *Garbatov and Soares* (2012). Even if sufficient data is gathered to establish component strength, experiments of single component do not consider the interdependence of components which is critical in real-world complex structural systems. Some larger experiments are also conducted though with less frequency, including the assessment of corroded box-girders *Saad-Eldeen et al.* (2013), even larger full scale experiments. However, the cost and time span make testing expensive; especially at large scale. Thus, it would be ideal to design a lab-level experiment reflecting many of the properties of large and complex marine structures. The designed experiment should not only mimic the multiple degradation process to explore the interactions among components, but also retain structural redundancy so that a single component failure will not remove all load carrying capacity.

Building numerical models of actual marine structures is challenged by uncertainties in the as-built condition. The uncertainties can come from various areas such as shipyard-to-shipyard differences, material qualities, and manufacturing variances. To handle such uncertainties, Bayesian networks (BN) have been explored to model the degradation of complex marine structures considering interactions among components. *Abaei et al.* (2018) applied BN on assessing reliability of marine floating structures and predicting the optimum design point of the mooring system. *Bhandari et al.* (2017) modeled the pitting degradation of ocean structures with BN. Numerous approaches have been developed based on BN, however, the majority of them have not been validated or evaluated by independent experimental data. Thus, the true applicability of this approach for real structures is not yet known.

In this work, the challenge of evaluating digital twin models is handled by designing and conducting a laboratory-level experiment reflecting the complex marine structural system. The labotory experiment can not only reduce time consumption but also mimic important system-level properties of real-world marine structures such as inter-dependence and structural redundancy. A system-level model is proposed and developed based on dynamic Bayesian network (DBN) modeling of the designed experiment. The performance of the proposed model is evaluated by the experimental data independent of the numerical model.

1.1 Motivation

Modeling structural degradation is critical for predicting structure performance and providing guidance towards inspection, maintenance and decision making. Numerical models are developed and relied on for simulating the degradation of marine structures, and serve as an essential part of the digital twin concept. Digital twin approaches are promising in enhancing lifecycle performance and forecasting risks. Many twins are attempting to model structural behavior at the system level rather than focusing on a single component. Beside the numerical model simulating complex marine structures, digital twins also fuse data into numerical model from real-world observations to increase the agreement between the numerical model and the actual structure. However, most of the proposed models are evaluated on self-generated data, which is usually dependent on the model, making the model performance less convincing. While a many experiments have been conducted, the majority of them focus on individual components of marine structures. Far fewer tests have been carried out on larger structure systems which however are expensive and usually time-consuming. The challenge exists in designing a laboratory-level experiment with acceptable expense and short time span reflecting important properties of real-world complex marine structures in degradation process such as dependence among components, components-to-system behavior, and structural redundancy. This work explores the design and fabrication of such a specimen tested in a laboratory-level experiment.

Numerical models in the marine structure area are challenged by uncertainties. Extended efforts have been conducted on building models from individual component probabilistic modeling to BN approaches. Traditional probabilistic methods only focus on analyzing the performance of individual components while BN brings us the capability of modeling structural behavior on a system level. Ordinary BN have been expanded to DBN by adding repeating time slices which are suitable for modeling crack propagation and other structure deterioration process. The first challenge left with us is modeling system behavior considering dependence and redundancy rather than modeling an individual component. Few DBN have been explored for system-level prediction and problems with dependence quantification and state-space explosion make the challenge even harder. This work explores the numerical model simulating the system-level structural deterioration based on DBN. The second major challenge is evaluating the performance of model with independent data leading to the development of an independent experiment under the concept of digital twins.

1.2 Research Overview

Digital twin approaches contain a numerical model simulating an actual structure and fuses data from observations to increase the agreement between model and structure. Based on digital twin, a laboratory-level deterioration experiment is designed and conducted to mimic the properties of real-world complex marine structures with affordable expense and time consumption. The deterioration is characterized as the growth of multiple fatigue. The crack growth and according applied cycles are recorded for the purpose of evaluating digital twin formulations on their ability to correctly track the experimentally-observed degradation. Additionally, two new methods for measuring crack length are developed and evaluated.

A numerical model is developed for modeling the deterioration in the laboratory-level experiment. Rather than modeling single component, the numerical model simulate the system-level behavior of complex structural system and make evidence-based prediction for crack propagation. The performance of developed numerical model is evaluated and validated by the independent experimental data.

1.3 Research Contribution

In this PhD research, a novel laboratory-level experiment is designed and conducted. A DBN approach is used to construct a corresponding numerical model of the degrading system. The experiment reflects common properties of complex marine structural system such as component dependence, component-to-system behavior, and structure redundancy. The numerical model simulates the crack propagation in system level and the performance is evaluated by the independent data collected from the designed experiment. The primary contribution of this PhD research can be summarized as follows:

1. A hexagon-shaped specimen with four propagating cracks is designed and tested in a laboratory-scale experiment. The specimen reflects important properties of complex structural system including crack dependence and structure redundancy. The specimen is applied with tension cycles and the test is under displacement control. The applied loading cycles and corresponding crack lengths are recorded as the major time-varying data of degradation state. Two approaches for measuring crack length are developed based on computer vision and Digital Image Correlation (DIC) technologies. A standard eccentrically-loaded single edge crack tension specimen is designed and tested to validate the performance of the developed computer vision based method for measuring crack length. Strain gauges integrated into a data acquisition system are deployed to monitor the structure strain state and assist in understanding the degradation process. Five sets of hexagon specimens have been tested with the data be-

ing documented for supporting the exploration of digital twin approaches. The test results demonstrate that the designed experiment successfully mimics the desired properties of complex marine structures.

2. A new numerical model is developed based on DBN to simulate the system-level deterioration. The task is divided into several steps. First, a single crack propagation with simulated evidence and two crack interaction considering component dependence with simulated evidence are investigated. The component dependence is modeled by a system-level hyperparameter and the performance is evaluated with generated evidence. Based on this, a system-level network is developed for modeling crack propagation in the hexagon experiment. The network is built in *Hugin* based on Object-oriented Networks (OON). The model is updated with dependence between crack length and stresses constructed on a *Hugin* technology called Temporal Clone. The models of hexagon specimen are evaluated by independent data collected from the test. The developed numerical model demonstrates strong capabilities in making accurate predictions of the growth of multiple fatigue.

CHAPTER II

Background

2.1 Introduction

The designed experiments and numerical model simulating the degradation process in the experiments are based on digital twin approaches and BN. This chapter aims to introduce the concept of digital twin and BN including the construction, quantification, inference approaches, and proposed extensions to DBN.

2.2 Digital Twins

The development of computer and simulation technology over the past decades as well as the increasing capability of collecting data leads to the emergence of digital twin approaches, *Schleich et al.* (2017) and *Schirmann et al.* (2018). Digital twin contains one or more numerical models simulating a real-world system of interest and fuses data from sensors or observations. With the data fusion, the agreement between numerical model and real-world system increases. Figure 2.1 demonstrated the concept of digital twin approaches, where M_1, M_2, M_3 and M_4 represent the numerical model for real-world system S_1, S_2. By fusing the gathered data, the difference between model and real-world system decreases to generate a more accurate prediction assisting decision making. The concept of digital twin guides the PhD

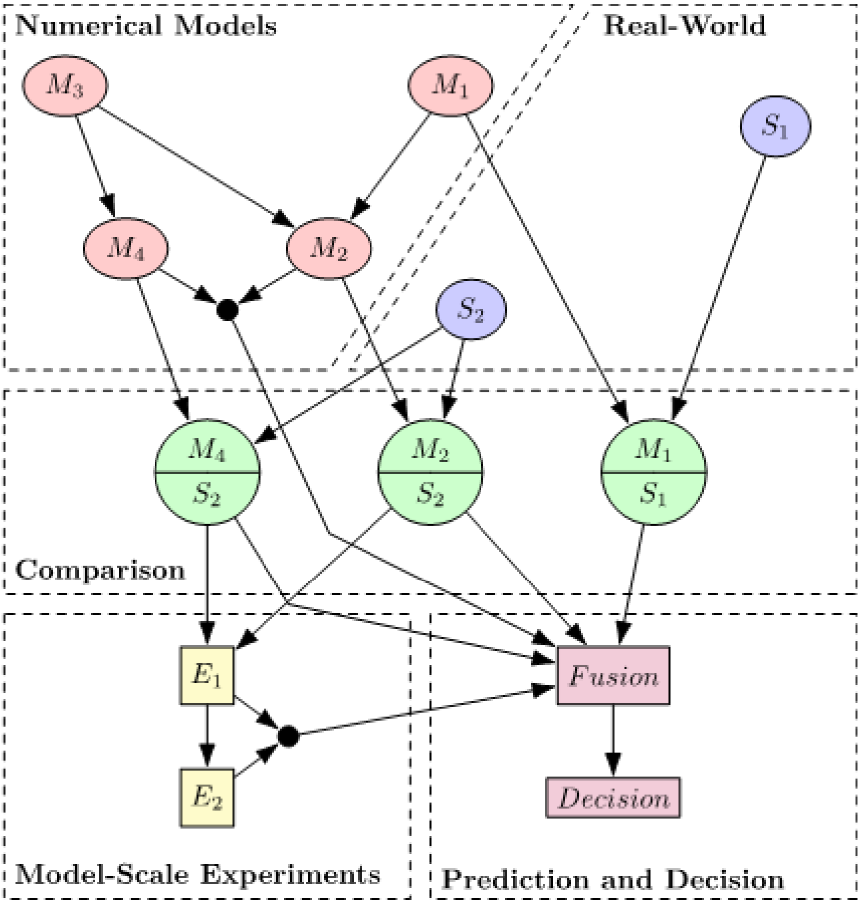

Figure 2.1: Concept of Digital Twin Approach, *Schirmann et al.* (2018)

research in designing laboratory-scale experiment and developing a numerical model for the experiment in terms of predicting structure degradation.

2.3 Bayesian Network

A BN is a probabilistic graphic structure allowing us to represent and reason about an uncertain domain *Korb and Nicholson* (2010). BN can handle the causal relationships between random variables and model complex structural systems dealing with diagnosis, updating and predictions *Weber et al.* (2012). The graphic structure of BN is a directed acyclic graph with nodes representing random variables and edges referring to conditional dependency. The conditional dependency is quantified by conditional probability distributions between two dependent nodes. The flow of condition dependence or the inference of Bayesian network is governed by the Bayes' Theorem describing the relationship of prior, conditional, and posterior probabilities:

$$P(A|B) = \frac{P(B|A)P(A)}{P(B)} \tag{2.1}$$

where A and B are nodes with causal relationship. $P(A)$ and $P(B)$ are marginal probabilities while $P(A|B)$ and $P(B|A)$ are conditional probabilities which are usually represented by a Conditional Probability Table (CPT).

Rewrite the Bayes' Theorem with chain rule as shown in Equation 2.2, the joint probability of random variables can be obtained, from which the marginal probability of a desired node can be acquired by summing over the states of its parent nodes as demonstrated in Equation 2.3, where random variables x_1 and x_2 are the parent nodes to random variable x_3. Figure 2.2 illustrates the structure of the network containing x_1 and x_2 as parent nodes and x_3 as child node.

$$P(x_1, x_2, ..., x_n) = P(x_1)P(x_2|x_1)P(x_3|x_2, x_1)...P(x_n|x_{n-1}, ..., x_2, x_1) \tag{2.2}$$

$$P(x_3) = \sum_{x_1}\sum_{x_2} P(x_1, x_2, x_3) = \sum_{x_1}\sum_{x_2} P(x_1)P(x_2|x_1)P(x_3|x_2, x_1) \tag{2.3}$$

In the following section, an example of BN is provided in terms of constructing, quantifying, and updating in BN.

2.3.1 Construction

Figure 2.3 demonstrates a straightforward case of BN model named "Earthquake or Burglar" case. This example is taken from *Jensen and V.* (1996). The model

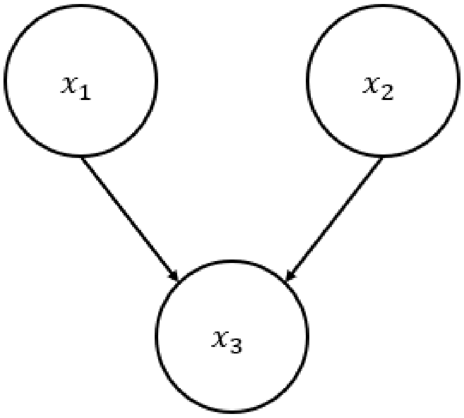

Figure 2.2: Illustration of Chain Rule of Bayesian Network

describes an alarm system which can be triggered by a burglary or an earthquake. The alarm system affects the probability of the homeowner receiving a call from John or Mary. Given the evidence that John or Mary calls, the probability of Burglar or Earthquake can be determined. Similarly, given the evidence that burglar or earthquake happens, the probability of John or Mary calling can be updated.

In the construction process of a BN, the state random variable is determined first by obtaining the desired variables. In this case, the random variables are built as nodes including "Burglar", "Earthquake", "Alarm", "John Call", and " Mary Call". With the determined random variables, the next step in constructing BN is finding the causal relationships between random variables. For example, since the alarm can be triggered by burglar or earthquake, two edges are built to connect parent nodes "burglar" and "earthquake" with child node "Alarm". To conclude, the structure of BN contains nodes and pointers representing random variables and causal relationships which is determined in the construction process of a BN.

2.3.2 Quantification

In a BN, each node contains a probability table indicating the probability of the random variable with respect to its possible states. Considering the structure

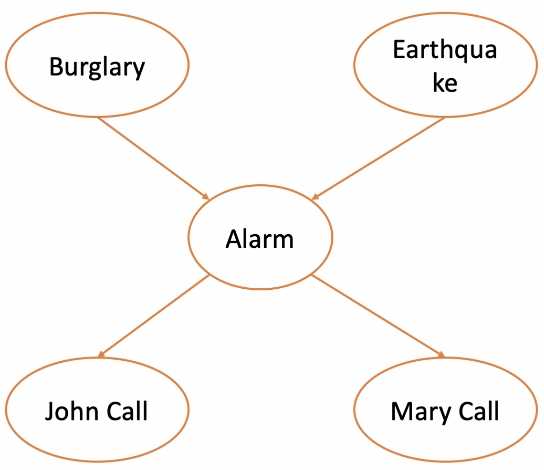

Figure 2.3: Structure of Bayesian Network for Burglary Case

of BN, two types of probability tables are used to quantify the model including a prior probability table and conditional probability table. Prior probability tables, associated with nodes having no parents, describes the probability of its states. Like the nodes “Burglary” in Figure 2.4 without any parent nodes, the probability table contains the states “T” and “F” with 50-50 chance. Conditional probability table (CPT) describes the probabilities of those random variables having parent nodes. CPT contains the states of each possible combination of parent nodes. For example, the node “Alarm” has a CPT as shown in Figure 2.4. Each column represents one combinations of its parent nodes. It should be noted that each column of CPT should sum up to 1 due to the mutual exclusive and exhausted definition of states.

After constructing and quantifying BN, the power of BN lies in updating, i.e. When the evidence is input into the network, for example, Mary makes the call, the marginal probabilities of the rest nodes will be updated accordingly. The following section includes more details of inference and updating in BN.

2.3.3 Inference in Bayesian Network

Several efficient inference methods have been developed for BN including exact and approximate inferences. The Junction Tree algorithm is one of the exact meth-

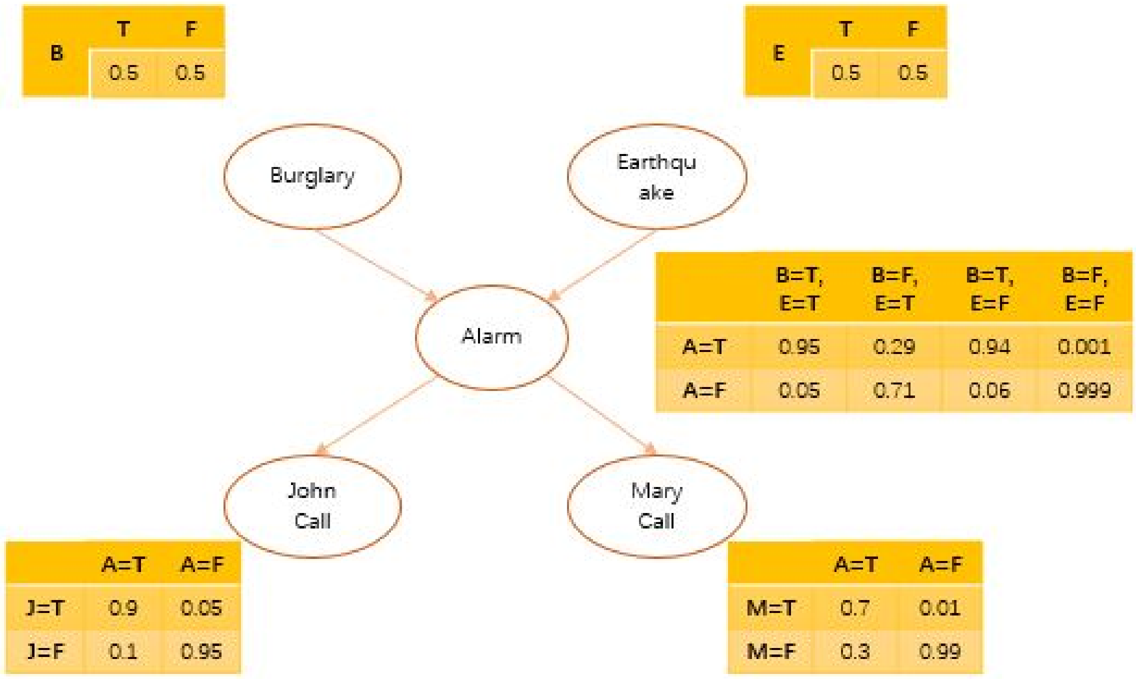

Figure 2.4: Bayesian Network and Potentials of Burglary Case

ods widely applied. Understanding the inference algorithm is important for tuning the Bayesian network for a better performance. The overall flow of Junction tree algorithm can be easily described, but few example cases have been studied to help understand the application of algorithm. Thus, in this section, the theory of Junction tree algorithm is described followed by a detailed example.

The Junction Tree algorithm can be divided into two parts in general: Junction Tree Construction and Message Passing, which comprise eight sub-steps as follows, *Korb and Nicholson* (2010):

1. Junction Tree Construction:

   (a) Moralize

   This step converts a directed graph to an undirected graph by removing the arrows; and "marries" the parents who have the same child by adding a chord

   (b) Triangulate

       Triangulate the moralized graph, which means every cycle of length greater than 3 possesses a chord

   (c) Construct Junction Tree

       Identify maximal cliques in the triangulated graph to form compound nodes; connect the nodes to construct the Junction Tree

   (d) Create Separators

       For every pair of connected compound nodes, add a separator between them serving as the intersection of the two compound nodes

2. Message Passing

   (a) Compute Parameters

       Assign the potentials to the nodes of Junction tree from CPTs and initialize the separators potentials to 1

   (b) Collect Evidence

       Select an arbitrary node as the root and start to collect evidence from leaf nodes. Leaf nodes usually connect with only one node

   (c) Distribute Evidence

       Pass the potential from the root node to leaves and the consistency of Junction Tree is reached

   (d) Marginal Probability

       Compute the marginal probability from the nodes' potentials

The message passing process is illustrated in Figure 2.5. Take node W as the leaf node while node V as root node. Then the forward pass updating process, from leaf node W to root node V, collects evidence from leaf nodes, which can be described as

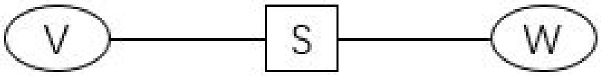

Figure 2.5: Bayesian Network Structure and Potentials

$$\phi_S^\star = \sum_{W/S} \phi_W \qquad \phi_V^\star = \frac{\phi_S^\star}{\phi_S}\phi_V \tag{2.4}$$

where $\sum_{W/S} \phi_W$ means summarizing ϕ_W over W to get $\phi_S^\star$ for updating ϕ_V, *Kahle et al.* (2008) and *Rosenberg* (2010).

Then the backward pass from root node V to leaf node W is,

$$\phi_S^{\star\star} = \sum_{V/S} \phi_V^\star \qquad \phi_W^\star = \frac{\phi_S^{\star\star}}{\phi_S^\star}\phi_V^\star \tag{2.5}$$

After conducting the two passes, local consistency is achieved described as,

$$\sum_{V/S} \phi_V^\star = \sum_{W/S} \phi_W^\star \tag{2.6}$$

The global consistency is achieved if Equation 2.7 is satisfied for any node V and W with intersection I,

$$\sum_{V/I} \phi_V = \sum_{W/I} \phi_W \tag{2.7}$$

In the following “Rain or Sprinkler” case, the Junction Tree algorithm is applied and explained according to the above steps. Four random variables are included in this model represented by nodes “Cloudy”, “Sprinkler”, “Rain”, and “Wet Grass”. The causal relationships are modeled by directed arcs indicating that the wet grass can be caused by sprinkler or rain which are affected by that if the weather is cloudy, *Murphy* (2001). Figure 2.6 shows the structure of this BN model along with their probability tables.

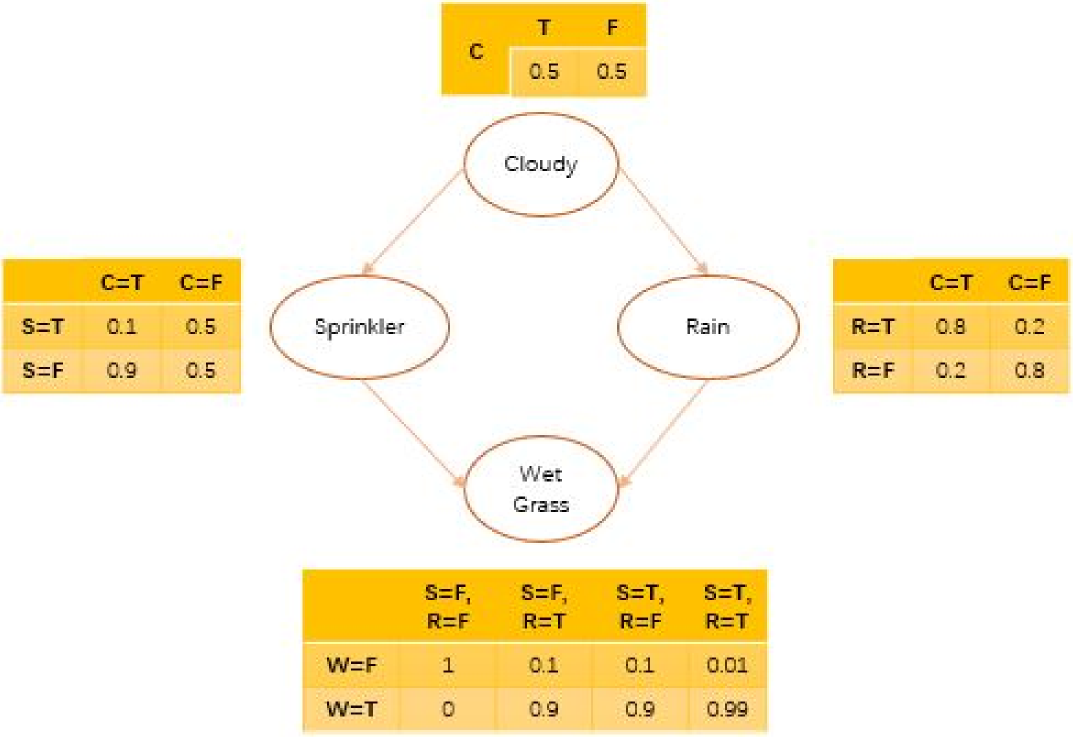

Figure 2.6: Bayesian Network and Potentials of Sprinkler Case

The process of generating Junction tree for the sprinkler case is demonstrated in Figure 2.7. Since the *sprinkler* node and *rain* node are parent nodes for *wetgrass* node, a chord is added when building moralized graph as shown in Figure 2.7(a). Then the maximal cliques are found as C, S, R and S, R, W with the intersection S, R as a separator, where C for *Cloudy*, S for *Sprinkler*, R for *rain*, and W for $WetGrass$.

Two types of evidences are investigated, the first one is a single observation that $wetgrass = T$, the second one involves two evidences which are $cloudy = T$ and $wetgrass = T$. Figure 2.8(a) and Figure 2.8(b) illustrate the collecting evidence process for evidence $wetgrass = T$. Due to the evidence, the probability of $wetgrass = F$ is removed. The dash node is the evidence node with $wetgrass = T$ as evidence, and the double-circled node is chosen as root node. The information flow is marked as

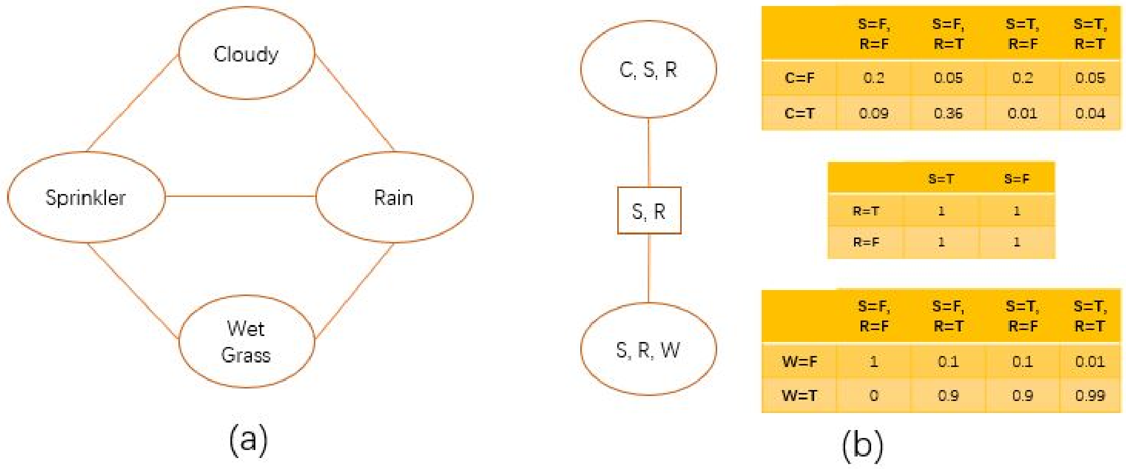

	S=F, R=F	S=F, R=T	S=T, R=F	S=T, R=T
C=F	0.2	0.05	0.2	0.05
C=T	0.09	0.36	0.01	0.04

	S=T	S=F
R=T	1	1
R=F	1	1

	S=F, R=F	S=F, R=T	S=T, R=F	S=T, R=T
W=F	1	0.1	0.1	0.01
W=T	0	0.9	0.9	0.99

Figure 2.7: Building Junction Tree of Sprinkler Case

red arrows. After the information reaches the root node, it is distributed backward as shown in Figure 2.8(c) and Figure 2.8(d).

Then the updated probabilities of *Cloudy*, *Sprinkler* and *Rain* can be acquired from the join probability $P(C, S, R)$ as follows. From the updated marginal probabilities, we can tell that if the grass is wet, the probability of being cloudy and having rain increases while the probability of using sprinkler decreases, which demonstrates the updating power of BN.

$$
\begin{aligned}
P(Cloudy = T) &= \frac{0 + 0.324 + 0.009 + 0.0396}{0 + 0.324 + 0.009 + 0.0396 + 0 + 0.045 + 0.18 + 0.0495} = 0.5758 \\
P(Cloudy = F) &= \frac{0 + 0.045 + 0.18 + 0.0495}{0 + 0.324 + 0.009 + 0.0396 + 0 + 0.045 + 0.18 + 0.0495} = 0.4242
\end{aligned}
\tag{2.8}
$$

$$
\begin{aligned}
P(Sprinkler = T) &= \frac{0.18 + 0.0495 + 0.009 + 0.0396}{0 + 0.324 + 0.009 + 0.0396 + 0 + 0.045 + 0.18 + 0.0495} = 0.4298 \\
P(Sprinkler = F) &= \frac{0 + 0 + 0.045 + 0.324}{0 + 0.324 + 0.009 + 0.0396 + 0 + 0.045 + 0.18 + 0.0495} = 0.5702
\end{aligned}
\tag{2.9}
$$

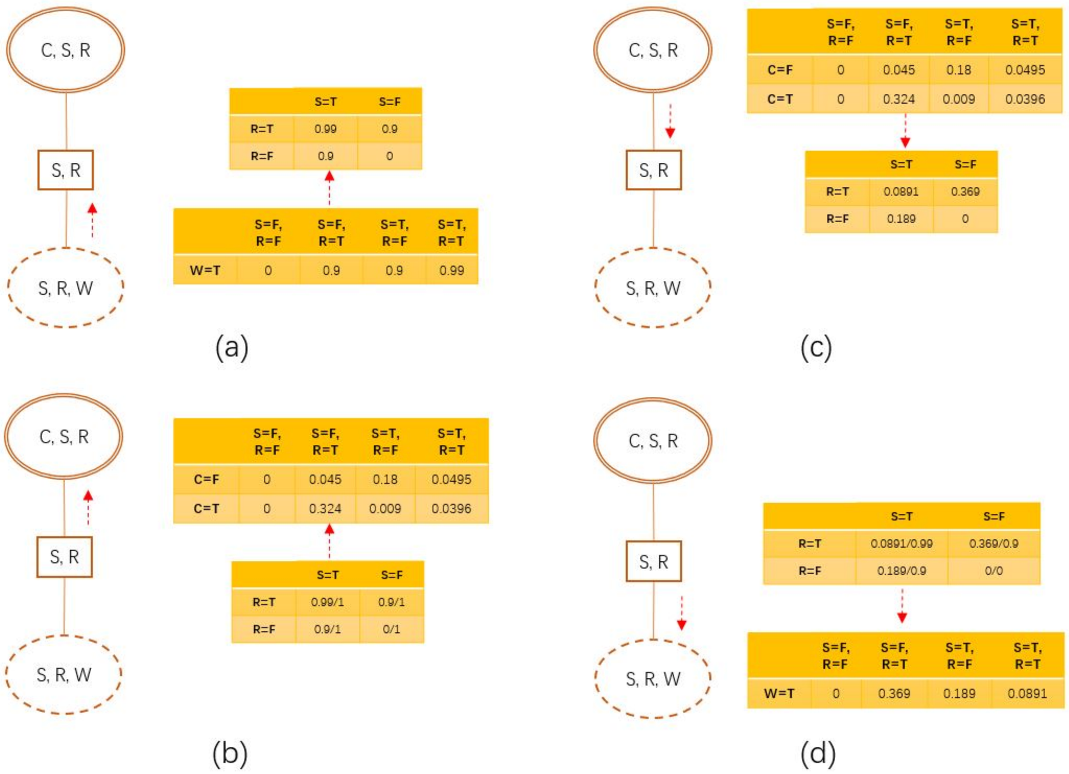

	S=T	S=F
R=T	0.99	0.9
R=F	0.9	0

	S=F, R=F	S=F, R=T	S=T, R=F	S=T, R=T
W=T	0	0.9	0.9	0.99

	S=F, R=F	S=F, R=T	S=T, R=F	S=T, R=T
C=F	0	0.045	0.18	0.0495
C=T	0	0.324	0.009	0.0396

	S=T	S=F
R=T	0.99/1	0.9/1
R=F	0.9/1	0/1

	S=F, R=F	S=F, R=T	S=T, R=F	S=T, R=T
C=F	0	0.045	0.18	0.0495
C=T	0	0.324	0.009	0.0396

	S=T	S=F
R=T	0.0891	0.369
R=F	0.189	0

	S=T	S=F
R=T	0.0891/0.99	0.369/0.9
R=F	0.189/0.9	0/0

	S=F, R=F	S=F, R=T	S=T, R=F	S=T, R=T
W=T	0	0.369	0.189	0.0891

Figure 2.8: Collecting and Distributing Evidence Process, case 2, evidence: "$wetgrass = T$" (information flow pass: (a)− >(b)− >(c)− >(d))

$$\begin{aligned} P(Rain = T) &= \frac{0.045 + 0.324 + 0.0495 + 0.0396}{0 + 0.324 + 0.009 + 0.0396 + 0 + 0.045 + 0.18 + 0.0495} = 0.7079 \\ P(Rain = F) &= \frac{0 + 0 + 0.18 + 0.009}{0 + 0.324 + 0.009 + 0.0396 + 0 + 0.045 + 0.18 + 0.0495} = 0.2921 \end{aligned} \tag{2.10}$$

For evidence $cloudy = T$ and $wetgrass = T$, Figure 2.9 demonstrates the process of collecting and distributing information which follows pass $(a)- > (b)- > (c)- > (d)$. Due to the observed evidence, the probabilities of $wetgrass = T$ and $cloudy = T$ are removed from tables, which means the potential of the cliques C, S, R and S, R, W is changed simultaneously according to evidence before updating. Then the collecting and distributing process is the same with the single evidence case as shown in Figure 2.9.

Then the updated probabilities of $Sprinkler$ and $Rain$ are acquired from the join probability $P(C, S, R)$ as follows. Compared to the case with single evidence

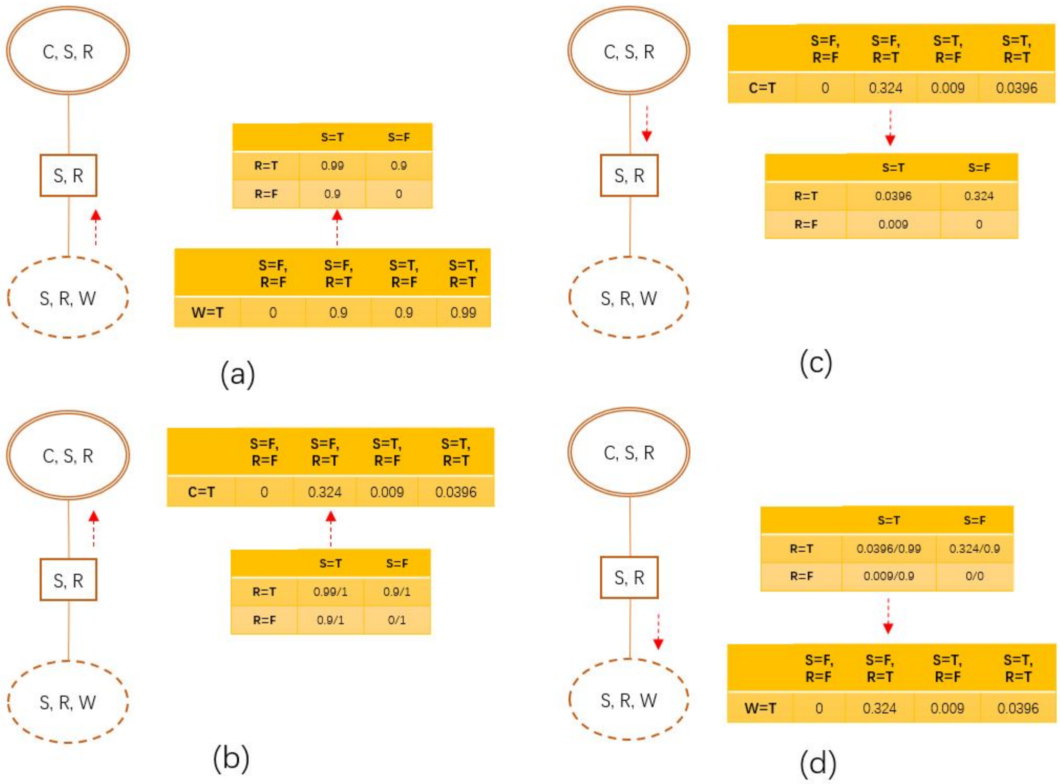

(a)

	S=T	S=F
R=T	0.99	0.9
R=F	0.9	0

	S=F, R=F	S=F, R=T	S=T, R=F	S=T, R=T
W=T	0	0.9	0.9	0.99

(b)

	S=F, R=F	S=F, R=T	S=T, R=F	S=T, R=T
C=T	0	0.324	0.009	0.0396

	S=T	S=F
R=T	0.99/1	0.9/1
R=F	0.9/1	0/1

(c)

	S=F, R=F	S=F, R=T	S=T, R=F	S=T, R=T
C=T	0	0.324	0.009	0.0396

	S=T	S=F
R=T	0.0396	0.324
R=F	0.009	0

(d)

	S=T	S=F
R=T	0.0396/0.99	0.324/0.9
R=F	0.009/0.9	0/0

	S=F, R=F	S=F, R=T	S=T, R=F	S=T, R=T
W=T	0	0.324	0.009	0.0396

Figure 2.9: Collecting and Distributing Evidence Process, Case 2, Evidence: "$Cloudy = T$", "$wetgrass = T$" (information flow pass: (a)− >(b)− >(c)− >(d))

$wetgrass = T$, the probability of raining increases to 0.9758 while the probability of using sprinkler decreases to 0.1304 which makes sense. The BN has more confidence that it is raining with the two pieces of evidence than a single pieces of evidence.

$$\begin{aligned} P(Sprinkler = T) &= \frac{0.009 + 0.0396}{0 + 0.324 + 0.009 + 0.0396} = 0.1304 \\ P(Sprinkler = F) &= \frac{0 + 0.324}{0 + 0.324 + 0.009 + 0.0396} = 0.8696 \end{aligned} \tag{2.11}$$

$$\begin{aligned} P(Rain = T) &= \frac{0.324 + 0.0396}{0 + 0.324 + 0.009 + 0.0396} = 0.9758 \\ P(Rain = F) &= \frac{0 + 0.009}{0 + 0.324 + 0.009 + 0.0396} = 0.0242 \end{aligned} \tag{2.12}$$

2.4 Dynamic Bayesian Network

Analyzing a dynamic system usually can be seen as working on time series data with real-time observations. Modeling of such systems requires Dynamic Bayesian network (DBN) developed from ordinary BNs by involving time. BNs can model the relations among variables in a specific time slot but cannot easily capture the evolvation of the system over time. DBN can model time series or dynamic process by expanding the BNs with slices representing the state of system at different time steps. In other words, a DBN can be constructed from a set of BNs that capture the instantaneous relationships between domain variables, together with a set of temporal dependencies that capture the dynamic behavior of the domain variables, *Dagum et al.* (1992). Figure 2.10 shows a general structure of DBN with slices at time $t-1$, t and $t+1$ referring to previous state, current state and future state respectively. In each slice, the instantaneous relationships between random variables ($X_{t-1} \to S_{t-1}$) are built similar to that in an ordinary BN. The edges between adjacent slices, known as temporal links, represent the transitions between nodes over time including the evolvation of the same node ($X_{t-1} \to X_t$) and different nodes ($X_{t-1} \to S_t$). For example, the current state of node X_t is affected by its previous state X_{t-1}. The current sate of node S_t is influenced by parents nodes X_t in current time slice and X_{t-1} in the previous time slice. Quantification of the DBN is similar to quantifying an ordinary BN except defining the transition matrix between time slices, i.e. $P(X_t|X_{t-1})$ is also required.

Since DBN contains discrete and static time slices representing the desired timesteps, DBN can be seen as static given a specific interested time point.The observations information is integrated in the past slices while the future slices represent a prediction based on observations in past. Due to the stactic property of DBN, the inference like Junction Tree applied to ordinary BNs in Section 2.3.3 can also be employed for the inference in DBN. The details of exact and approximate inference methods for DBN can be found in *Murphy* (1994).

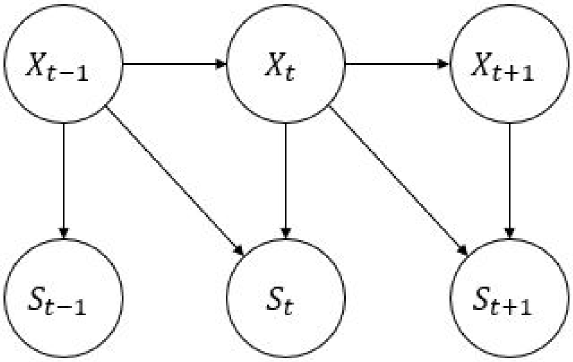

Figure 2.10: Concept of Dynamic Bayesian Network

2.5 Conclusion

Based on Bayes' rule, BNs introduced in this chapter offer evidence-based updating providing valuable predictions. Feeding evidence into BNs, the marginal probabilities of random variables are updated accordingly. This chapter describes the theory behind BNs, construction, quantification, and inference of BNs. Based on BNs, DBN are introduced which are suitable for modeling dynamic system such as the process of structure degradation. By inputting real-time observations into a DBN modeling crack growth, the structural characters can be updated and the predictions of future crack length can be updated accordingly.

CHAPTER III

Laboratory Level Experiment Mimicking Complex Structural System: Design, Deployment, and Analysis

3.1 Introduction

This PhD research focuses on two subject areas: experimental and numerical model, which serves as two essential parts of a digital twin. A digital twin contains models of real-world structures and fuses data from observations of the structures and scale experiment to pull the models into better agreement with the real world. Digital twin models have the promise of representing complex marine structures and providing enhanced lifecycle performance and risk forecasts. Experimentally verifying the updating approaches is necessary but rarely performed. Thus, the proposed work is designing an experiment and developing a numerical model updated by the experimental data. In this chapter, the design of experiment of a structural system with time-evolving degradation as well as the associated data collecting methods are presented. A fatigue crack growth mechanism is selected as a suitable degradation mechanism of the structure. A model of system reliability is constructed based on DBN in Chapter IV, which is evaluated by the data collected from the experiments described in this chapter.

In the following sections, a laboratory scale experiment of a four-crack hexagon-shaped specimen is presented, designed to mimic many of the properties of complex degrading marine structural systems, such as crack interaction, component interdependence, redundant load path and non-binary failure. The design of specimen, methods of measuring crack length, execution of the experiment and the collected data are presented and discussed.

3.2 Design

3.2.1 Introduction

In this section, the literature review of structure experiment is conducted followed by the design of specimen and grip. The fatigue testing system is introduced and the execution steps of the experiment is summarized.

3.2.2 Literature Review

In the past decades, experimental tests of marine structures have been conducted in several sub-areas. The most common tests focus on the components of marine structures, determining the component strength and properties. Numerous component experiments can be found in the literature, including compressive and collapse tests on stiffened panels *Gordo and Soares* (2008) and *Xu and Soares* (2013), strength analysis on deteriorated steels plates *Saad-Eldeen et al.* (2016a) and *Saad-Eldeen et al.* (2016b), and fatigue evaluation on welded ship structural joints *Garbatov and Soares* (2012). Experiments of single component do not consider critical properties of real-world complex structural system such as the interdependence of components. Some larger experiments are also conducted with less frequency, including the assessment of corroded box-girders *Saad-Eldeen et al.* (2013) and *Saad-Eldeen et al.* (2012). Full scale experiments of marine structure is very rare *Pohler et al.* (1979). However, the cost and time consumption make these testing expensive; especially at large scale. Thus, a laboratory scale experiment reflecting many of the properties of large and complex marine structures would be a major advantage in developing and testing digital twin approaches. The designed experiment should not only mimic multiple degradation processes to explore the interactions among components, but also retain structural redundancy so that a single component failure will not remove all load carrying capacity.

3.2.3 Design Concept

The motivation for the presented experiment is to conduct testing of a multiple-crack fatigue specimens representing the degradation characteristics of a more complex structural system. Such systems are currently the focus of digital twin approaches, where numerical models of real-world structures are fused data from observations of the structures and scale experiments to pull the models into better agreement with the real world. In the present experiment, the fatigue crack growth and maximum reaction force is recorded verses the applied cycles. The recorded data can not only be used for validating and evaluating the performance of a DBN but also as physical experiment results to support research into complex structural degradation.

The experiment is designed to evaluate system-level response of a complex structure in a laboratory level test mimicking the properties of real-world structure in degradation process. By keeping the experiment at lab scale, the cost and time associated with the test can be significantly reduced. Thus, while the specimen does not physically match any marine structure of interest, as a load-carrying system, the specimen reflects several system-level properties of more complex marine structures, including:

- Multiple components with redundant load paths

- Changing (degrading) properties over time
- Failure that are continuous, not binary intact/failed
- Allowing for periodic updating and inspections
- Contains a common system-level parameter to measure overall structural performance

3.2.4 Initial Specimen Design

Based on the desired properties, the designed structure must possess both multiple degradation process and redundancy so that a single element failure will not remove all load carrying capability to simulate the deterioration process of real-world marine structural system. A simple diamond structure was designed first with four pre-cracks on each arm as shown Figure 3.1. Four pre-cracks are designed based on ASTM standard E1290 *ASTM* (2008) to boost the initiation of cracks and restrict the crack propagation in desired areas. Due to the symmetric diamond shape, the four pre-cracks are equivalent at the beginning of experiment but one or two cracks are expected to be dominant as the applied load cycles increase. The specimen is preloaded to ensure the loaded cycles are in tensile. The experiment is conducted under displacement control with the reaction force at the maximum displacement treated as a stand-in for the capability of structure. The R ratio is decreasing with the reduction of the reaction force due to the propagation of cracks. The data gathered from the experiment are the number of applied cycles and corresponding maximum reaction force and crack length. Figure 3.2 demonstrates an Abaqus model of the diamond specimen built to calculate the Stress Intensity Factor (SIF) to ensure the initialization of cracks. The frame of diamond specimen without pre-cracks is machined by waterjet from sheets of ASTM A36 steel whose properties are shown in Table 3.1. The pre-cracks are machined by wired EDM with a 0.004 *inches* diameter wire for

Material	Young's modulus	Poisson's ratio
ASTM A36 steel, plate	200 GPa	0.26

Table 3.1: Parameters for ASTM A36 Steel Plate

high-resolution crack tips.

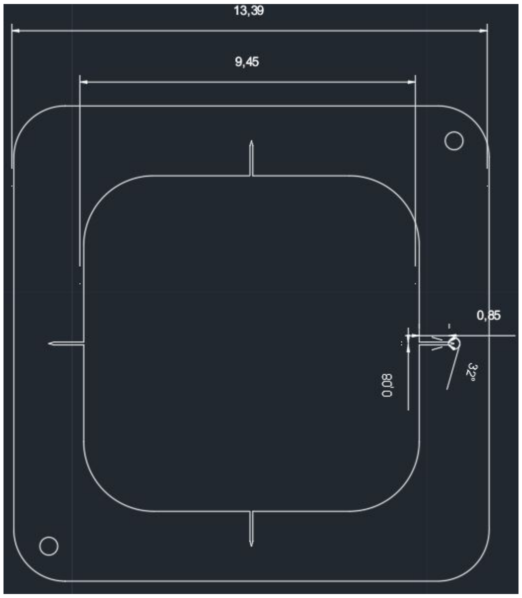

Figure 3.1: Diamond Specimen Design

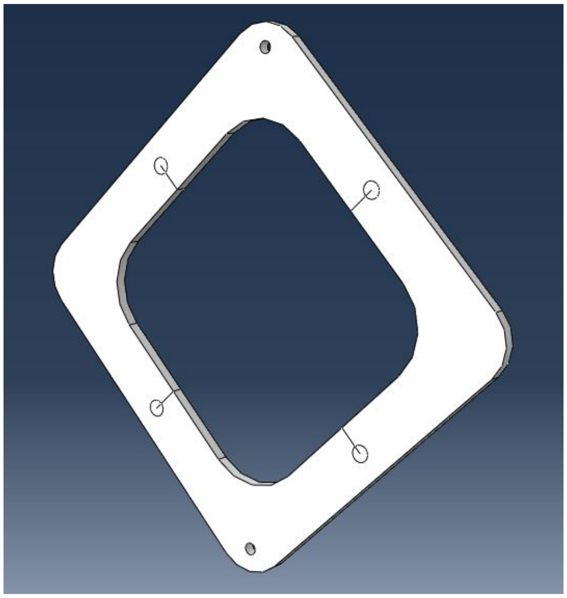

Figure 3.2: ABAQUS Model for SIF

According to the design of specimen and the data recorded in the experiment, several experiment requirements are summarized as follows,

1. The vertical test space should be larger than the diagonal of specimen
2. The number of cycles can be tracked
3. The displacement can be tracked to 0.01 mm accuracy applying displacement control with less than a 1 mm maximum displacement
4. The reaction force can be measured to $0.1kN$ accuracy

Based on the listed requirements, an MTS 810 material testing system, a multipurpose servohydraulic testing systems with 250 kN capability and ±75 mm stroke, is selected for performing the test. The 810 Material Testing System provides high stiffness, precision-aligned load frames with integral actuators delivering a broad array of testing capabilities for both low and high force static and dynamic testing. By selecting from a variety of force capacities, servovalve flow ratings, pump capacities, software, and accessories, the floor-standing 810 system can easily be configured to meet the fatigue test requirements. Figure 3.3 shows the MTS 810 material testing system mounted with diamond specimen.

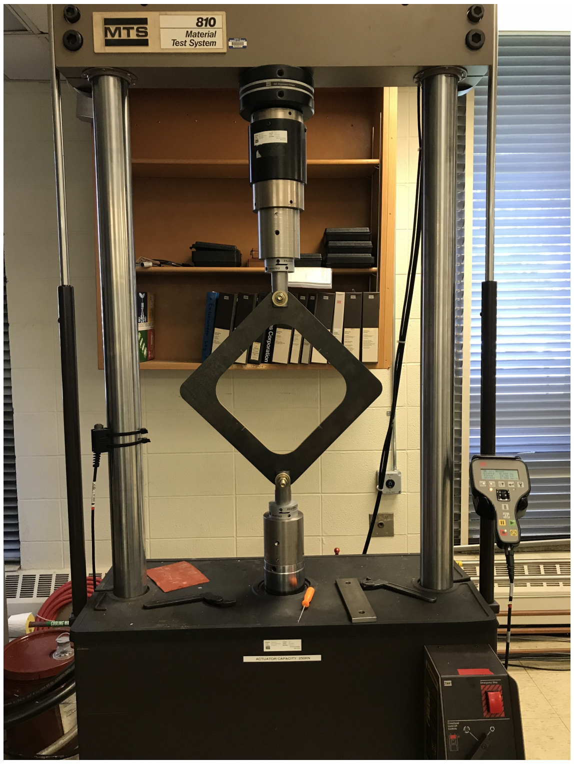

Figure 3.3: MTS 810 Material Testing System with Diamond Specimen

Unexpectedly, the cracks of diamond specimen didn't propagate even the number of cycles reached two million. The possible reason is that the SIF was designed to be above the material minimums but the actual material apparently had a much higher threshold SIF considering the variance of material quality. Thus, the design was revised and a hexagon shape specimen is proposed in the following section.

3.2.5 Revised Specimen Design

A modified design is proposed with a hexagon shape containing four pre-cracks at each corner based on ASTM standard E1290 *ASTM* (2008). The pre-cracks serve the same purposes as in the diamond shape specimen. Moreover, the pre-cracks have a 15 degree orientation which helps the propagated crack be straight as demonstrated in the CAD plot, Figure 3.4. Except the four corners where pre-cracks locate, the other corners are rounded to reduce stress concentration. The experiment is still conducted under displacement control and the specimen is preloaded to ensure the applied cycles are in tension. The test is conducted on MTS 810 material testing system with the crack length and reaction force measured every 100000 cycles. The test is conducted with frequency of 7 Hz.

An Abaqus model is built to find the required displacement and reaction force with respect to the desired SIF. Quadratic element C3D20 is used for the frame while C3D15 is employed for modeling the crack front. Under 0.65 mm displacement, the maximum reaction force is 22.05 kN and the SIF is 31.8 $Mpa\sqrt{m}$, which is capable to start crack propagation even if the material toughness is significantly above the grade minimums. The frame of hexagon specimen without pre-cracks is cut by waterjet from sheets of ASTM A36 steel. The pre-cracks are machined by wired EDM with a 0.004 *inches* diameter wire for high-resolution crack tips.

In order to mount specimen onto fatigue test machine, two grips were designed and manufactured. The grips contain two parts: the head and the threaded stud. The two parts are designed to connect together rather than a single machined part to reduce stress concentration between stub and head. The threaded stud part and the head part are mounted together and fastened by Loctite Threadlocker Red 271. Figure 3.6 shows the 3D sketch of the grip. The threaded stud fastens the grip onto test machine while a bolt going through the head part locks the specimen and grip together. The head part is machined from 1215 carbon steel; the threaded stud is

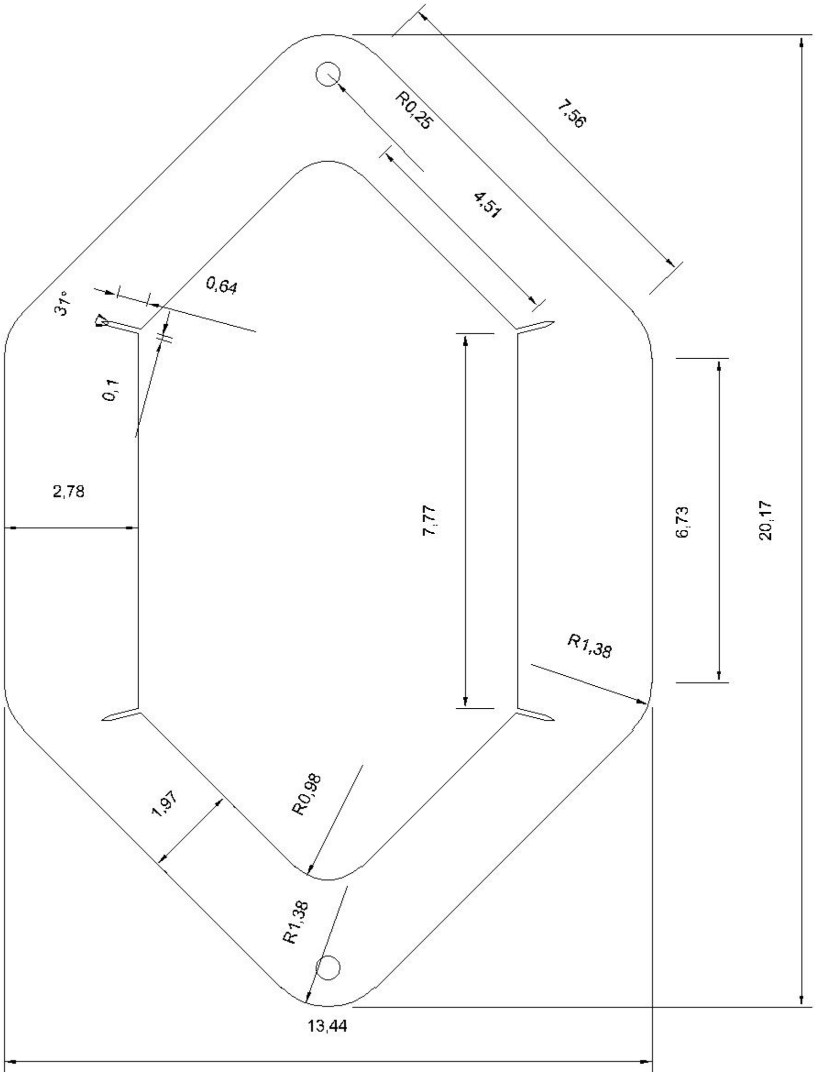

Figure 3.4: CAD Plot of Hexagon Specimen (unit: inch)

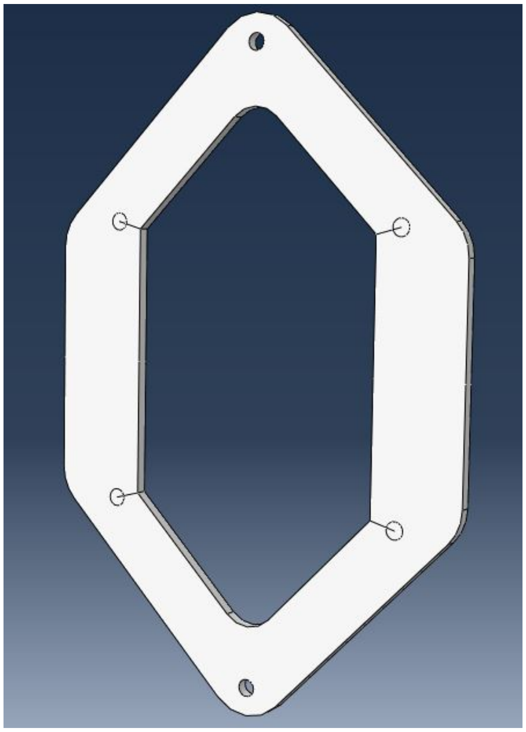

Figure 3.5: ABAQUS Model for SIF, Hexagon Specimen

B7 alloy steel purchased from Grainger, and the hex bolt is a grade 8 bolt with zinc plated surface. Two 1/16” thick PVC washers are placed between specimen and grip to center the specimen and ensure the reaction force is in-plane.

Owing to the symmetric shape, the four pre-cracks are equivalent at the beginning of the experiment but one or two cracks are expected to become dominant as the applied cycles increase, which reflects the interactions among components. The specimen is loaded in tensile cycles with a constant maximum displacement, and the reaction force at the maximum displacement is treated as a stand-in for the overall system capability of the structure. This force reduces over time as the cracks grow. The data gathered from the experiment is the number of applied cycles verses corresponding maximum reaction force and all four crack length. The methods developed for measuring crack length are explained in the following sections.

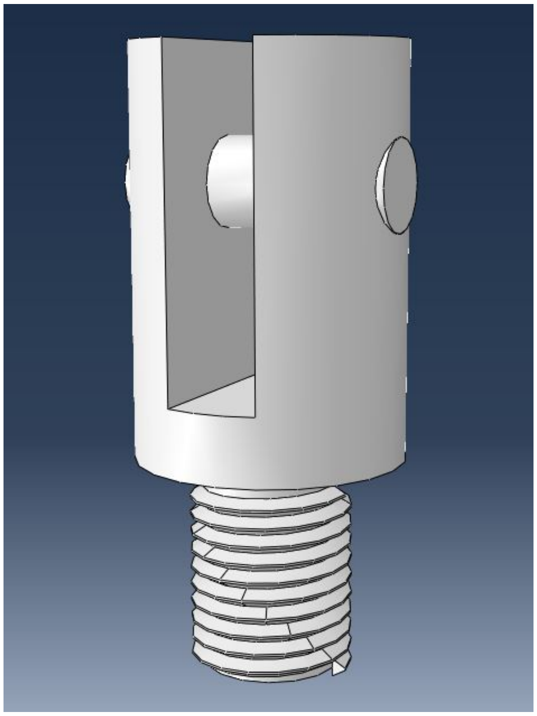

Figure 3.6: 3D Sketch of Grip

3.2.6 Testing Setup

The steps for setting up the testing is summarized as follows:

1. Mount grips onto MTS 810 testing machine
2. Launch MTS 810 software and open testing frame
3. Mount the hexagon specimen onto the top grip
4. Align the holes on bottom grip and hexagon specimen through MTS 810 software, fix the specimen with bolts
5. Setup the testing parameters in MTS 810 software including frequency, displacement, number of cycles, etc.
6. Preload the specimen and reset the reference point after preloading
7. Run the test for 100000 cycles, then stop the test for measurement and record the data

The test is conducted with frequency of 7 Hz. The designed hexagon specimen fails around 1 million cycles resulting in roughly 40 hours for conducting one test, which usually lasts for one week in practice.

3.3 Measuring Crack length - Computer Vision Method

3.3.1 Introduction

Three methods are employed to measure crack length during the experiment - measuring with a machinist scale, Computer Vision (CV) based method and Digital Image Correlation (DIC) method. Usually, it is not accurate enough to optically measure crack length with machinist scale, especially for cracks with curvature. Thus, the computer vision based methods is developed in this PhD research and applied in the hexagon experiment, providing a simple, low-cost and accurate method for measuring crack length on steel structures.

In the developed computer vision method, the crack is detected from images which are converted into a matrix containing intensity and then the crack length is measured on a pixel level. In order to have a accurate measurement, the noise haa to be filtered out with different strategies. The flowchart in Figure 3.7 summarizes the procedure of applying computer vision method onto an image. The first step is acquiring crack images with digital cameras which stores RGB images with the amount of red, green and blue colors on each pixel point. Since the colors are not helpful for detecting the cracks, the RGB image is transferred to a grayscale image in the second step. The pixel values of grayscale images indicates the amount of light at that pixel ranging from 0 (black) to 255 (white). In the third step, two filters are applied for smoothing the grayscale images and detecting cracks. Then noises are filtered out for a more accurate calculation of crack length on a pixel level. The last step is transferring the pixel-level crack length to real dimension. The following section presents the details of computer vision method including the steps, methodology, results, and discussion.

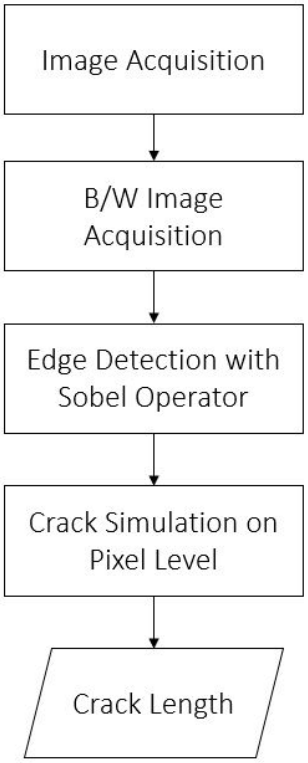

Figure 3.7: Flow Chart of Crack Length Capturing Process based on Computer Vision

3.3.2 Literature Review

During the past decades, measuring crack size has been investigated with different methods. The most conventional method is crack width gauge which basically is a scale containing transparent upper plate marked with a red crosshair cursor and a white bottom plate marked with measuring grid. The distance between cursor and grid can indicate the width of crack. However, this method is designed commonly for measuring crack width restricting its usage in measuring crack length; and error is introduced by observing the crack optically. Extending from the idea of a crack width gauge, a traveling microscope is developed for measuring crack length. Traveling microscopes contain a cast iron base holding a movable microscope. The microscope can eliminate the optical error in determining crack tip by using high magnification. It successfully monitored the fatigue crack propagation in polymer foams, *Saenz et al.* (2014). However, in our application, this device requires a removal of the specimen from testing machine for measurement, increasing the test time. For in-situ measurements on complex specimens, the microscope must be mounted on the specimen itself, and then if the crack grows in an unexpected direction incompatible with the initial mounting, the mounting must be changed during the experiment. Several other techniques have been developed involving acoustic wave reflection. Acoustic wave methods compose a transmitter and a receiver sending and receiving acoustic wave with designed frequency, *Resch et al.* (1985), *Kimoto et al.* (2006), *Longo et al.* (2010). The high-frequency component of the transmitted wave will be reflected from the discontinuities of structure like cracks and flaws. However, the complexity of the technology and specialized knowledge required to implement this technique limit the application in experiments. Digital image correlation method has also been explored to measure crack size which is reviewed in detail in Section 3.5. Thus, developing a practical and flexible method for measuring crack size in large scale tests is necessary.

3.3.3 Capture Images

A GoPro HERO4 camera with 12.0 Mega Pixel (MP) resolution is used to take PNG pictures at 4000 × 3000 dimension. A NEEWER 12.5X macro lens is mounted on GoPro camera to allow the GoPro image to focus on the small region around a growing crack. The camera is mounted on a flexible tripod that can be easily moved around the specimen to take images of all active cracks. In order to increase the contrast between structure surface and crack, the crack area is painted by Fluid Fluorescent Dye adapted from leak detection for traditional coolant systems. The Fluid Fluorescent Dye shows bright maize color under Ultraviolet (UV) lights. The UV dye is painted on the surface of structure when the crack is closed by removing the loading on the structure (e.g. pausing the fatigue test apparatus at zero or a low load value). After the crack is re-opened by re-applying displacement to the specimen, the crack is observable and recorded. The setup of capturing images is shown in Figure 3.8.

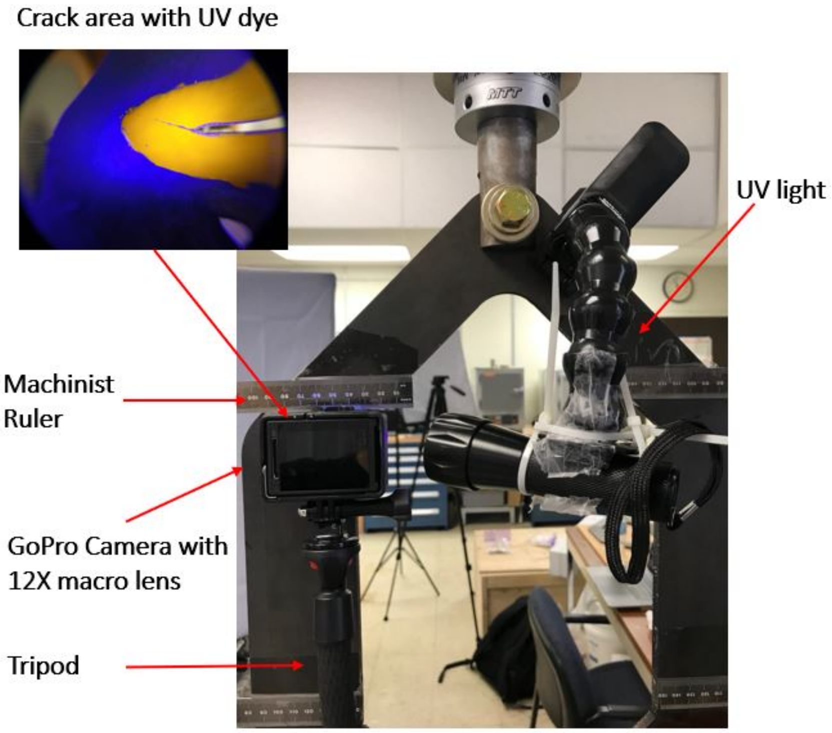

Figure 3.8: Setup of Capturing Images-Computer Vision Method

The detailed procedure for capturing crack images is summarized as follows:

1. Stop the test and remove the loading on structure
2. Clean the surface of crack growth regions
3. Mount the GoPro camera and UV light onto the crack location, adjust the distance between camera lens and specimen surface to make sure the lens is parallel to the specimen surface and the crack image is clear; turn on cameras and UV light to stand by
4. Paint the crack area with Fluid Fluorescent Dye

5. Apply the maximum displacement to the specimen and take pictures

3.3.4 Image Prepossessing

After capturing images, several preprocessing technologies of images are applied to prepare the images for cracks detection. The first prepossessing of images is transferring the RGB image to Grayscale for the convenience of applying filters. In this step, the information of colors stored in RGB image is substituted by the amount of light or intensity. Then, a Gaussian filter is implemented as the second prepossessing to smooth the image and reduce noises. Gaussian filter can enhance the image quality captured under poor or uneven lighting. In image possessing, the Gaussian filter is implemented as a window moving along the pixels, convolving the image with the Gaussian function. The Gaussian function in two dimension is shown in Equation 3.1, where x is the coordinate in the horizontal axis, y is the coordinate in the vertical axis and σ is the standard deviation of the Gaussian distribution, *Nixon and Aguado* (2012), *Shapiro and Stockman* (2001). Values are sampled from Equation 3.1 to build a convolution matrix applied on the Grayscale image. Figure 3.9 demonstrates a sampled convolution matrix averaging the pixel values by the weights shown in the matrix.

$$G(x,y) = \frac{1}{2\pi\sigma^2} e^{-\frac{x^2+y^2}{2\sigma^2}} \tag{3.1}$$

$$\frac{1}{16}\begin{bmatrix} 1 & 2 & 1 \\ 2 & 4 & 2 \\ 1 & 2 & 1 \end{bmatrix}$$

Figure 3.9: A 3 × 3 Sampled Convolution Matrix

3.3.5 Edge Detection

In order to detect cracks, a Sobel operator is applied to the processed image. The Sobel operator is a gradient operator approximating the gradient of image density. The Sobel operator composes two convolution matrices applied on the horizontal and vertical directions as shown in Figure 3.10. The two matrices measure gradient in each orientation of input image which can be combined following Equation 3.2 to calculate the gradient magnitude at each pixel. In Equation 3.2, G_x is the gradient on horizontal direction while G_y is the vertical gradient. The Sobel operator convolves the image with a small, separable, and integer-valued filter in the horizontal and vertical directions and is therefore relatively inexpensive in terms of computations *Sobel and Feldman* (1968).

$$|G| = \sqrt{(G_x^2 + G_y^2)} \tag{3.2}$$

$$\underset{G_x}{\begin{bmatrix} -1 & 0 & 1 \\ -2 & 0 & 2 \\ -1 & 0 & 1 \end{bmatrix}} \qquad \underset{G_y}{\begin{bmatrix} 1 & 2 & 1 \\ 0 & 0 & 0 \\ -1 & -2 & -1 \end{bmatrix}}$$

Figure 3.10: Convolution Matrices of Sobel Operator

3.3.6 Crack Simulation and Calculation

The image with detected cracks usually contains noise points biasing the calculating of crack length on pixel level. Therefore, it is critical to filter out noise points before calculating crack length. The gradient is first filtered by a threshold determined by the gradient magnitude of the cracks, which is to eliminate points corresponding with relatively small gradient since the edge should be accompanied by obvious intensity change and thus a relatively large gradient magnitude. Accordingly, the threshold can be set higher for a high-quality image compared with poor quality images. Besides, the Sobel operator can also detect the boundary of image so the gradients magnitude of image density near boundaries are set to 0. The detected edge is stored as a series of gradient scalars, where the number indicates gradient magnitude on the pixel point as shown in Figure 3.11. The series of number in a specific column indicates the width of the crack at the specific location of image. The numbers inside the crack width are usually not zero in practice since the intensity is not homogeneous. In other words, the crack in the image is marked with high gradient scalars for many consecutive rows. Some noise points have the similar format but less width than the real continuous cracks which may come from the non-uniform lighting or uneven painting. These noise points are filtered out according to their short width, and the corresponding lower number of rows. For the current experiment, it is observed that noises points usually have less than three rows which is adopted as the threshold for filtering out noise points with short width.

After filtering out noise points on pixel level, the next step is calculating the crack length on pixel level. It is worth mentioning that the numerical values on pixel points refer to the gradient magnitude and the length calculation requires the location of pixel points whose gradient magnitude is significant. Since width is not considered for length calculation, the column of sequential numerical values in Figure 3.11 indicating crack width is compressed vertically by selecting the median for the whole column of their coordinate location. The median is used instead of mean to avoid bias from any possible outlier in the column. A series of coordinate of pixel points is acquired in this step representing the location of the crack. Calculating the crack length based on every filtered pixel point can introduce bias since the distance between two pixel points is too small to be used for describing the entire crack length. Thus, ten pixel points are compressed and grouped together horizontally by selecting the median of the grouped pixel points for calculating crack length on pixel level. In summary, the gradient magnitudes are compressed vertically first since width is not considered for calculating crack length, then the magnitudes are compressed horizontally for representing the crack length accurately.

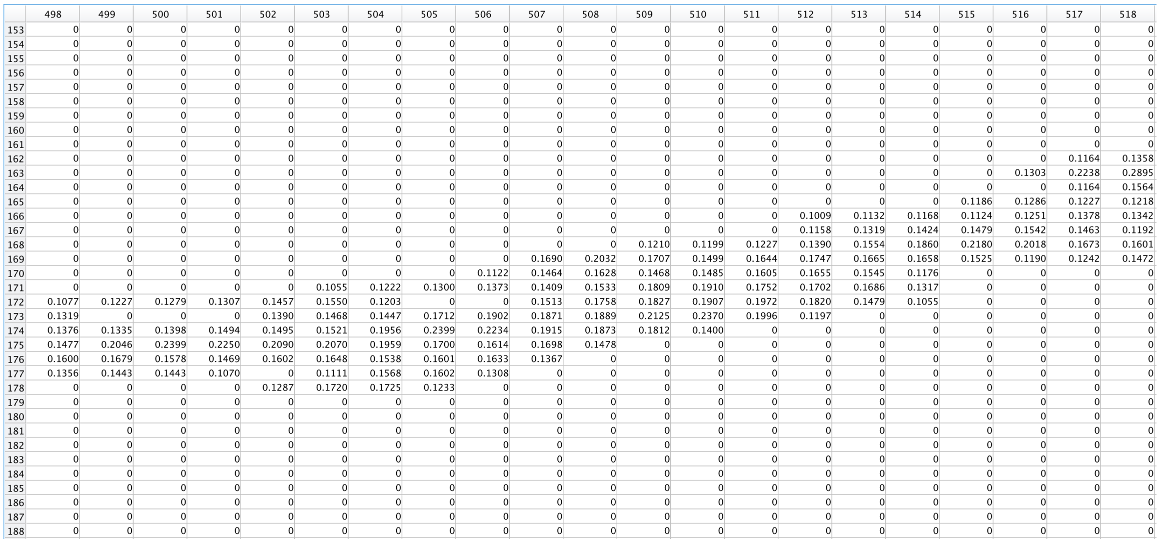

	498	499	500	501	502	503	504	505	506	507	508	509	510	511	512	513	514	515	516	517	518
153	0	0	0	0	0	0	0	0	0	0	0	0	0	0	0	0	0	0	0	0	0
154	0	0	0	0	0	0	0	0	0	0	0	0	0	0	0	0	0	0	0	0	0
155	0	0	0	0	0	0	0	0	0	0	0	0	0	0	0	0	0	0	0	0	0
156	0	0	0	0	0	0	0	0	0	0	0	0	0	0	0	0	0	0	0	0	0
157	0	0	0	0	0	0	0	0	0	0	0	0	0	0	0	0	0	0	0	0	0
158	0	0	0	0	0	0	0	0	0	0	0	0	0	0	0	0	0	0	0	0	0
159	0	0	0	0	0	0	0	0	0	0	0	0	0	0	0	0	0	0	0	0	0
160	0	0	0	0	0	0	0	0	0	0	0	0	0	0	0	0	0	0	0	0	0
161	0	0	0	0	0	0	0	0	0	0	0	0	0	0	0	0	0	0	0	0	0
162	0	0	0	0	0	0	0	0	0	0	0	0	0	0	0	0	0	0	0	0.1164	0.1358
163	0	0	0	0	0	0	0	0	0	0	0	0	0	0	0	0	0	0	0.1303	0.2238	0.2895
164	0	0	0	0	0	0	0	0	0	0	0	0	0	0	0	0	0	0	0	0.1164	0.1564
165	0	0	0	0	0	0	0	0	0	0	0	0	0	0	0	0	0	0.1186	0.1286	0.1227	0.1218
166	0	0	0	0	0	0	0	0	0	0	0	0	0	0	0.1009	0.1132	0.1168	0.1124	0.1251	0.1378	0.1342
167	0	0	0	0	0	0	0	0	0	0	0	0	0	0	0.1158	0.1319	0.1424	0.1479	0.1542	0.1463	0.1192
168	0	0	0	0	0	0	0	0	0	0	0	0.1210	0.1199	0.1227	0.1390	0.1554	0.1860	0.2180	0.2018	0.1673	0.1601
169	0	0	0	0	0	0	0	0	0	0.1690	0.2032	0.1707	0.1499	0.1644	0.1747	0.1665	0.1658	0.1525	0.1190	0.1242	0.1472
170	0	0	0	0	0	0	0	0	0.1122	0.1464	0.1628	0.1468	0.1485	0.1605	0.1655	0.1545	0.1176	0	0	0	0
171	0	0	0	0	0	0.1055	0.1222	0.1300	0.1373	0.1409	0.1533	0.1809	0.1910	0.1752	0.1702	0.1686	0.1317	0	0	0	0
172	0.1077	0.1227	0.1279	0.1307	0.1457	0.1550	0.1203	0	0	0.1513	0.1758	0.1827	0.1907	0.1972	0.1820	0.1479	0.1055	0	0	0	0
173	0.1319	0	0	0	0.1390	0.1468	0.1447	0.1712	0.1902	0.1871	0.1889	0.2125	0.2370	0.1996	0.1197	0	0	0	0	0	0
174	0.1376	0.1335	0.1398	0.1494	0.1495	0.1521	0.1956	0.2399	0.2234	0.1915	0.1873	0.1812	0.1400	0	0	0	0	0	0	0	0
175	0.1477	0.2046	0.2399	0.2250	0.2090	0.2070	0.1959	0.1700	0.1614	0.1698	0.1478	0	0	0	0	0	0	0	0	0	0
176	0.1600	0.1679	0.1578	0.1469	0.1602	0.1648	0.1538	0.1601	0.1633	0.1367	0	0	0	0	0	0	0	0	0	0	0
177	0.1356	0.1443	0.1443	0.1070	0	0.1111	0.1568	0.1602	0.1308	0	0	0	0	0	0	0	0	0	0	0	0
178	0	0	0	0	0.1287	0.1720	0.1725	0.1233	0	0	0	0	0	0	0	0	0	0	0	0	0
179	0	0	0	0	0	0	0	0	0	0	0	0	0	0	0	0	0	0	0	0	0
180	0	0	0	0	0	0	0	0	0	0	0	0	0	0	0	0	0	0	0	0	0
181	0	0	0	0	0	0	0	0	0	0	0	0	0	0	0	0	0	0	0	0	0
182	0	0	0	0	0	0	0	0	0	0	0	0	0	0	0	0	0	0	0	0	0
183	0	0	0	0	0	0	0	0	0	0	0	0	0	0	0	0	0	0	0	0	0
184	0	0	0	0	0	0	0	0	0	0	0	0	0	0	0	0	0	0	0	0	0
185	0	0	0	0	0	0	0	0	0	0	0	0	0	0	0	0	0	0	0	0	0
186	0	0	0	0	0	0	0	0	0	0	0	0	0	0	0	0	0	0	0	0	0
187	0	0	0	0	0	0	0	0	0	0	0	0	0	0	0	0	0	0	0	0	0
188	0	0	0	0	0	0	0	0	0	0	0	0	0	0	0	0	0	0	0	0	0

Figure 3.11: Detected Edge by Sobel Operator

The last step is transferring the pixel length to real world dimension in millimeter. Here, a feature in the image of known size is needed to establish as relationship between pixels and real-world distance. For this step, the quality of the initial image is also critical, as image sensor must be parallel to the surface of the specimen, and areas of high lens distortion must be avoided. In trials to date, a simple machinist scale glued on the specimen bridges the dimension in millimeter and pixel length finishing the calculation of crack length. The scale is marked at 0.5 mm resolution, and is located immediately adjacent to the crack to establish this conversion.

3.3.7 Initial Result and Discussion

The developed method is coded in MATLAB and applied to the images captured from the hexagon experiment to measure the crack length. Figure 3.12 illustrates the application of developed method on a captured image. To increase the contrast between crack and structure surface, the UV dye is painted after the testing machine is temporarily stopped resulting in no applied displacement on the specimen. Then the specimen is applied with the maximum displacement to open the crack showing in Figure 3.12a as the original image, which is transferred to grayscale in Figure 3.12b. The grayscale image is smoothed by Gaussian filter followed by Sobel operator detecting the cracks as shown in Figure 3.12c. After filtering out the noise, the crack length on pixel level is calculated from the Euclidean distance of grouped pixel points. Figure 3.12d demonstrates the simulated crack length.

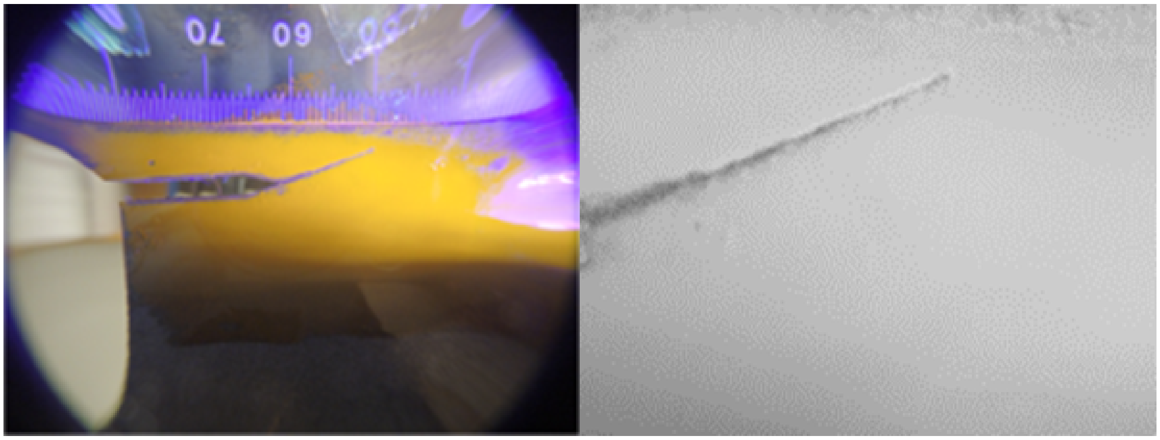

(a) Original Image (b) B/W Image

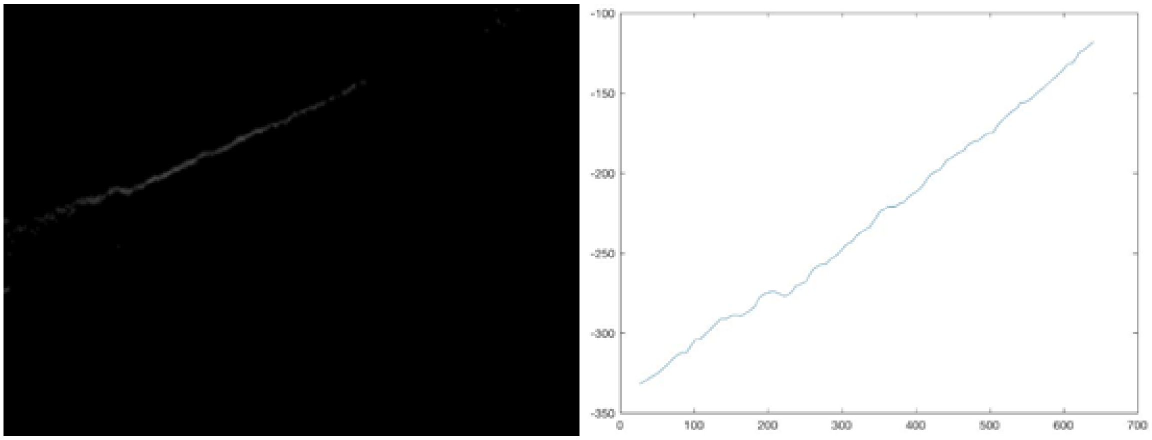

(c) Edge Detected (d) Crack Simulated

Figure 3.12: The Application of Computer Vision Method

The performance of the developed method is demonstrated and investigated in this section on the acquired images from the fifth hexagon fatigue test. Since the cracks are straight, the measurement from machinist scale is adopted here as a comparison with computer vision method. The percentage errors between the measurement from computer vision method and machinist scale are calculated based on Equation 3.3, where L_{cv}, L_{scale} is the crack length measured by the developed method and machinist scale respectively. Table 3.2 compares the measurement of crack length from the fifth hexagon experiment. Since the CV method requires cracks to be opened when taking pictures so that the crack and the rest regions can have different intensity for edge detection, the CV results of left top and right bottom at 800000 cycles are not available due to the unopened crack. The percentage error is relatively large when the crack is small. With the propagation of the crack, the percentage error decreases resulting in a mean error around 4.23% with standard deviation around 3.98%, encouraging for the proposed CV method. Given the relative easy application of the method, and its ability to quickly record the length of several cracks on the same specimen, it appears well suited for system fatigue tests where tracking multiple crack length is the key experimental result. When investigating potential causes of the error, one area is identified for improving the performance which is to improve the quality of captured images. The quality of captured images can be enhanced by improving the ambient light and revising the mounting system to ensuring that the lens is parallel to structure surfaces.

$$Error = |\frac{L_{cv} - L_{scale}}{L_{scale}}| \times 100\% \tag{3.3}$$

3.4 Validation of Computer Vision Based Method

In order to have a more exact validation than just using the data from the fifth hexagon experiment, the developed computer vision method in Section 3.3 is validated by a standard fatigue test with a traverse microscope as conventional method for measuring crack length. The design of standard fatigue test specimens, test setup,

Cycles	*Left Top (MS;CV)*	*Error%*	*Left Bottom(MS;CV)*	*Error%*	*Right Top(MS;CV)*	*Error%*	*Right Bottom(MS;CV)*	*Error%*
100000	2.00; 2.27	13.50	2.30; 2.19	4.78	2.65; 2.42	8.68	2.40; 2.81	17.08
200000	5.50; 5.51	0.18	5.50; 5.22	5.09	5.65; 5.34	5.49	4.50; 4.43	1.55
300000	8.25; 8.38	1.57	8.00; 7.79	2.63	8.50; 8.38	1.41	7.50; 7.41	1.2
400000	11.40; 11.12	2.46	11.00; 11.89	8.09	11.75; 11.88	1.11	9.80; 9.81	0.10
500000	13.25; 12.8	3.40	14.10; 13.98	0.85	14.80; 14.5	2.03	11.80; 11.69	0.93
600000	14.70; 15.29	4.01	17.50; 18.97	8.4	19.00; 17.9	5.79	12.60; 12.53	0.55
700000	14.70; 16	8.84	23.50; 22.93	2.42	25.00; 26.14	4.56	12.60; 14.05	11.56
800000	14.70; N/A	N/A	30.75; 31.92	3.80	31.50; 32.16	2.09	12.60; N/A	N/A
Mean of Error% (CV)					4.23			
Std of Error% (CV)					3.98			

Table 3.2: Comparison of Crack Length of Machinist Scale and CV Method of the Fifth Hexagon Experiment (unit: mm; MS = Machinist Scale; CV = Computer Vision)

and validation results are included in the following section.

3.4.1 Experimental Design

The validation of the developed computer vision based method has been conducted on two standard eccentrically-loaded single edge crack tension specimen, which is a rectangular specimen with an edge pre-crack designed following the ASTM standard, *ASTM* (2011). The detail dimension of the specimen is shown in the CAD plot, Figure 3.13. The bolt hole has the same dimension with those on hexagon specimens so that the grip can be employed for this validation test as well. The specimen without pre-cracks is cut by waterjet from an A36 steel sheet with 9 mm thickness and the pre-crack is machined by wired EDM with 0.004 inches diameter wire for high-resolution crack tips. The experiment is tested under displacement control. An Abaqus model is built to calculate the SIF given specific displacements. The detail procedure is similar to the modeling of hexagon specimen in Section 3.2.3. The SIF is calculated using contour integral method around crack front region. The quadratic element C3D20 is used for the frame while C3D15 is employed for modeling the crack front. For the specimen with pre-crack, the calculated SIF is 30 $Mpa\sqrt{m}$ with 23.6 kN maximum reaction force under 0.3 mm displacement.

As the conventional measuring method, a traverse microscope is employed to

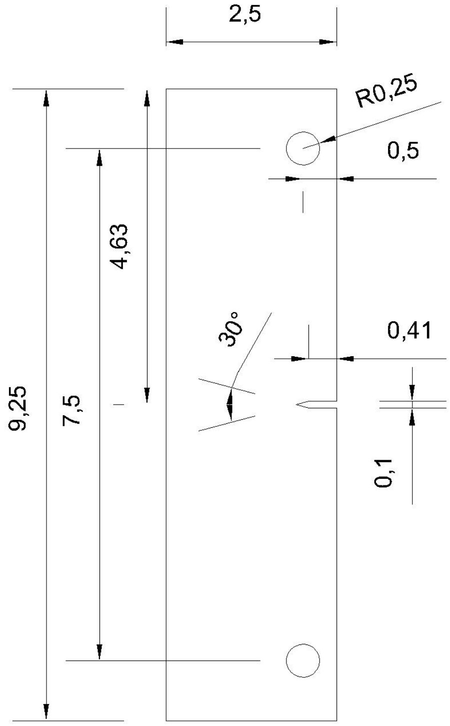

Figure 3.13: CAD Plot of Standard Eccentrically-loaded Single Edge Crack Tension Specimen (unit: *inch*)

measure the crack length at the back side of the specimen while the computer vision method measures the crack at the front side. The traverse microscope has 20X magnification capability which is equipped with a micrometer with a resolution of $1e^{-5}$ inches. To help the traverse microscope locates crack tip, UV dye is also painted on the backside surface of structure when the crack is closed by pausing the fatigue test apparatus at zero or a low load value. After the crack is re-opened by re-applying load to the specimen, the crack length is measured under UV light. The measured crack length is compared with the results from CV method. The setup of the validation test is shown in Figure 3.14. Since the crack is straight, a machinist scale with marking of 0.5 *mm* was also used to measure the crack length on the front side to ensure the crack propagate through the thickness identically,

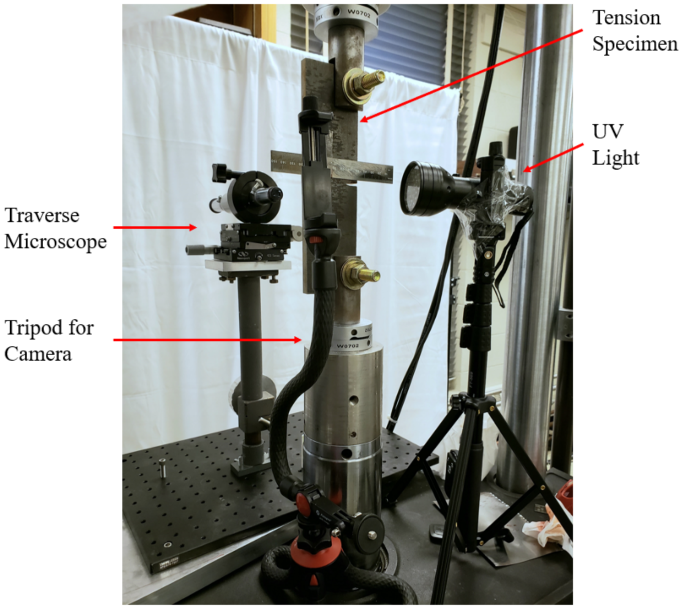

Figure 3.14: Test Setup of the Validation of Computer Vision Based Method

3.4.2 Test Setup

Two standard eccentrically-loaded single edge crack tension specimens have been tested on MTS 810 testing system. The grip designed for hexagon specimen is used to fix the standard crack specimen onto testing frame. Two PVC washers are inserted between specimen and grips to ensure the reaction force is in-plane. The standard specimens were preloaded at 8 kN to guarantee a slack-free connection between the specimen and the fixture bolts. The test is under displacement control with a maximum displacement amplitude of 0.14 mm resulting to a maximum reaction force of 23.6 kN. The first test was recorded 6 times with respect to different crack length while the second one was recorded 11 times to provide sufficient data points for validation purpose. In each recording, three methods are applied to record the crack length. The traverse microscope measured the crack length from the backside of the specimen, and the CV method is applied on the front side for the convenience of taking photos. In order to ensure the cracks on both sides are identical, a machinist scale with marking of 0.5 mm was also used to measure the crack length on the front side.

The process of testing a standard eccentrically-loaded single edge crack tension specimen is summarized as follows:

1. Mount grips onto MTS 810 testing machine
2. Launch MTS 810 software and open testing frame
3. Mount the standard eccentrically-loaded single edge crack tension specimen onto the top grip with bolts and PVC washers
4. Align the holes on bottom grip and single edge crack tension specimen through MTS 810 software, fix the specimen with bolts and PVC washers
5. Setup the testing parameters in MTS 810 software including frequency, displacement, number of cycles, etc.
6. Preload the specimen and reset the reference point after preloading
7. Run the test for 75000 cycles and stop the test for the first measurement, then decrease the increment of applied cycles from 40000 to 7000 in terms of gathering more measurements

3.4.3 Validation Results

An example of applying developed CV method on captured image is demonstrated in Figure 3.15 from original image to simulated crack. To increase the contrast between crack and structure surface, the UV dye is painted after the testing machine is temporarily stopped resulting in no applied displacement on the specimen. Then the specimen is applied with the maximum displacement to open the crack showing in Figure 3.15a as the original image, which is transferred to grayscale as shown in Figure 3.15b. The grayscale image is smoothed by the Gaussian filter and the cracks are detected by Sobel operator illustrated in Figure 3.15c. After filtering out the noise, the pixel points are first grouped by finding the median points, then the crack length on pixel level is calculated from the Euclidean distance of grouped pixel points. The simulated crack length is demonstrated in Figure 3.15d. Table 3.3 and 3.4 shows the recorded crack length as well as the crack length calculated by computer vision method. Error 1 compares the crack lengths on the frontside and backside measured by machinist scale and traverse microscope respectively. Error 2 indicates the difference between crack lengths measured by traverse microscope and CV method. Figure 3.16 and 3.17 plot the measured crack length by traverse microscope, machinist scale and CV method. The crack length measured by traverse microscope and machinist scale has a relatively large error at 115000 cycles in the second standard fatigue test, which could come from the impurity of the material obstructing the growth of crack temporarily. However, the rest measured crack lengths by traverse microscope and machinist scale have acceptable error indicating the cracks on the back and front side are identical. Since the conventional and CV methods are applied on the back and front side respectively, the identical length on the two sides makes the comparison of conventional and CV methods meaningful. Even the difference between results of conventional and CV methods are relatively large at 200000 cycles in the first test and 115000 cycles in the second test, the most measurements matches very well with mean of error around 5.5 % and standard deviation around 7.2 %. The validation results demonstrate the performance of the developed CV method. Given the relative easy application and its ability to quickly record the length of several cracks on the same specimen, the developed CV method is suitable for measuring total crack length in system fatigue tests.

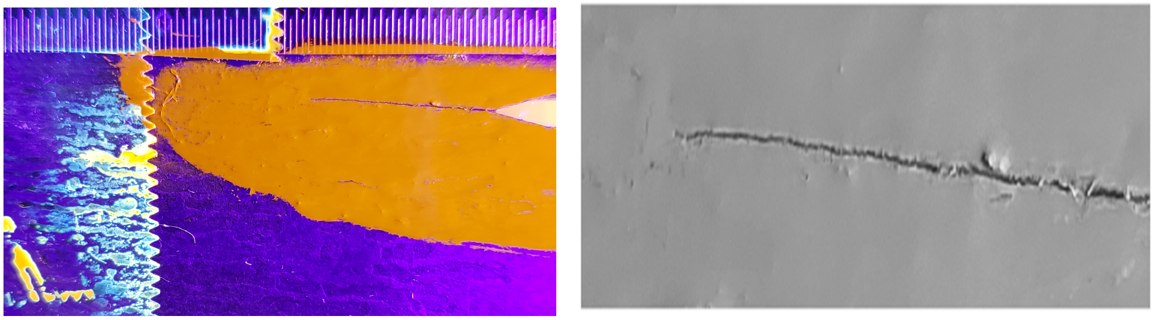

(a) Original Image (b) B/W Image

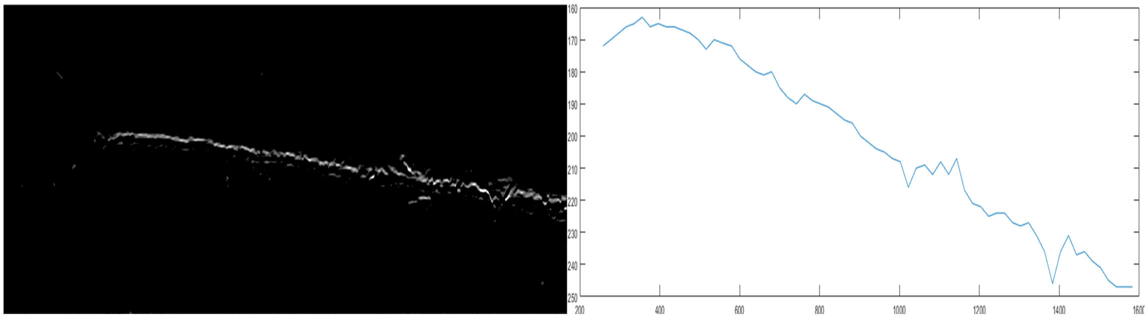

(c) Edge Detected (d) Crack Simulated

Figure 3.15: The Validation of Computer Vision Method

Cycles	*Traverse Microscope (backside)*	*Machinist Scale (frontside)*	*CV method (frontside)*	*Error1 (%)*	*Error2 (%)*
150000	6.70560	7.1	6.6790	5.882	0.397
200000	12.80160	12.5	10.2647	2.356	19.817
225000	16.56080	16.6	16.3971	0.237	0.988
240000	20.16760	19.8	19.3698	1.823	3.956
247500	21.84400	21.6	20.7989	1.117	4.784
255000	23.92680	24.3	22.9990	1.560	3.878
		Mean of Error		2.162	5.637
		Std of Error		1.957	7.166

Table 3.3: Validation Results of Computer Vision Based Method from The First Standard Fatigue Test (unit: mm)

Cycles	*Traverse Microscope (backside)*	*Machinist Scale (frontside)*	*CV method (frontside)*	*Error1 (%)*	*Error2 (%)*
75000	2.28600	2.4	2.2449	4.987	1.798
115000	5.18160	4.0	4.1375	22.804	20.150
150000	7.70128	7.6	7.6082	1.315	1.209
165000	8.89000	9.5	9.2773	6.862	4.357
180000	11.50112	11.4	11.6840	0.879	1.590
195000	13.66520	13.6	15.0165	0.477	9.889
205000	15.91056	15.5	15.5417	2.580	2.318
215000	17.79016	17.5	20.9704	1.631	17.876
225000	20.16760	20.0	20.1087	0.831	0.292
232000	21.79320	21.0	22.0879	3.640	1.352
239000	23.89632	23.6	23.8591	1.240	0.156
Mean of Error				4.295	5.544
Std of Error				6.454	7.203

Table 3.4: Validation Results of Computer Vision Based Method from The Second Standard Fatigue Test (unit: mm)

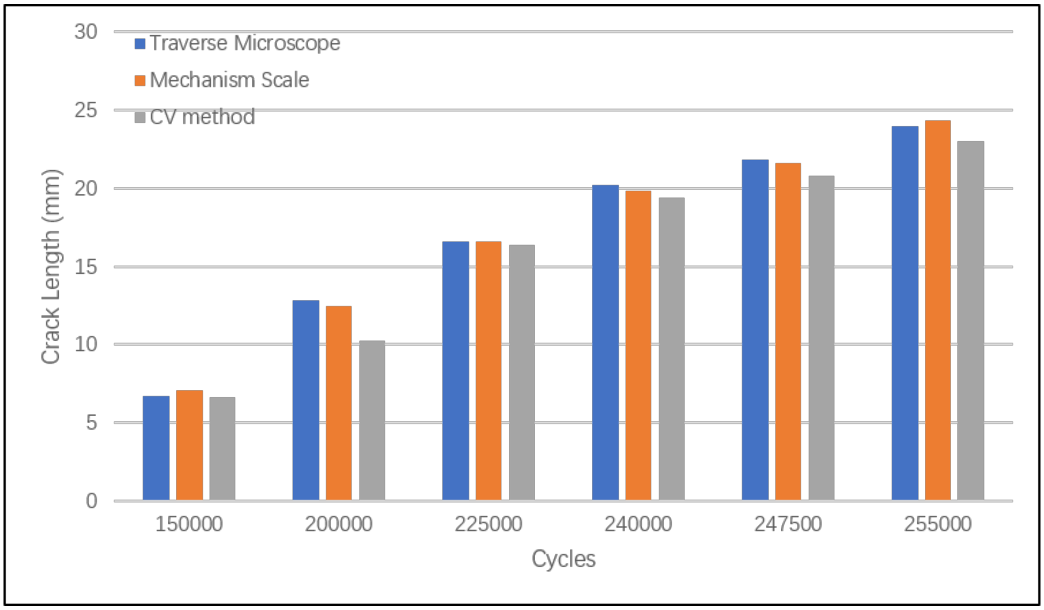

Figure 3.16: Measured Crack Lengths of The First Validation Test

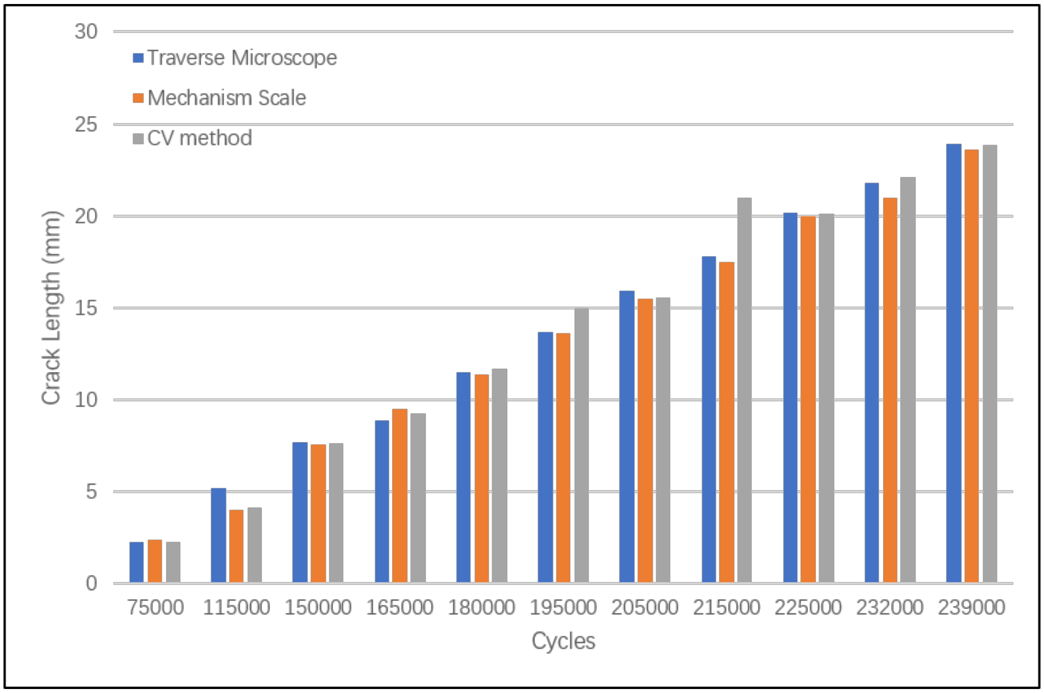

Figure 3.17: Measured Crack Lengths of The Second Validation Test

3.5 Measuring Crack length - Digital Image Correlation Method

3.5.1 Introduction

Due to the rapid development of computers and charge-coupled device (CCD) cameras, the DIC technique is widely used as a full-field non-contact measuring method. DIC is a post-possessing approach to acquire the field-strain and displacement of structure under deformation, which can be performed for detecting the crack tip and calculate the crack length. Figure 3.18 shows the procedure of applying DIC method. The structure surface is prepared by painting with speckle patterning in terms of matching the reference and deformed images. Then the first step is similar to the computer vision method which captures images for analysis. The difference is that in order to perform correlation of images successfully, the structure surface needs to be painted with a refined pattern, i.e. the surface is paint with black background color and some tiny white particles are made for tracking and correlating. Then a region of interest (ROI) is drawn to indicate the area for analysis. The processing of image is performed by an open-source software named GOM Correlate, and the crack length can be acquired by plotting the major strain verses distance which is explained in detail in the following sections.

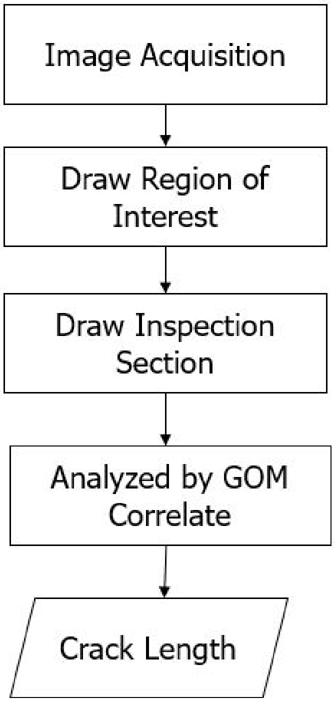

Figure 3.18: Flow Chart of DIC Method

3.5.2 Literature Review

DIC method was first proposed by *Peters and Ranson* (1982) utilizing digital imaging techniques to correlate the deformed images and references in terms of measuring surface displacements. During the past decades, the proposed method has been applied to fields such as automotive, material science, aerospace, and civil. *Brauser et al.* (2010) analyzed the deformation behaviour of spot-welded specimens which is widely used in automotive structures by acquire the local strain distributions through DIC method. *Rossini et al.* (2015) investigated dissimilar laser welding of high strength steel sheets for automotive industry by monitoring the deformation field on the surface of the specimen using DIC. In aerospace area, DIC is usually employed in experimental analysis of panels such as evaluating the fracture behavior of a large aircraft panel with a propagated crack, *Du et al.* (2011). DIC has also been used in material research related to fatigue. *Sutton et al.* (1992) conducted an experimental study of the near tip deformation fields for a Single Edge-Cracked specimen and generated a parabolic fit to the acquired displacement data in terms of locating crack tip. *Sutton et al.* (2007) used DIC to acquire full-field deformations during the loading and stable tearing processes in terms of characterizing the stable crack extension behavior of an aluminum alloy. *Lee et al.* (2009) investigated fracture behavior such as crack initiation and rapid growth of multilayered unidirectional graphite using DIC and high-speed cameras. The broad application of DIC inspired modifying and using it in this research for obtaining crack length.

3.5.3 Image Acquisition

The quality of captured figure is critical in a successful DIC application relying on camera and lighting system. A Blackfly BFLY-PGE-31S4M GigE CCD camera manufactured by FLIR is used in the experiment. The reason of choosing CCD camera is that its sensors can create high-quality and low-noise images while CMOS sensors are more susceptible to noise. A Sony IMX265 sensor is equipped in the Blackfly CCD camera capturing monochrome figure at 35 Frame per Second (FPS) with resolution 2048×1536. Tamron 23FM25SP lens is combined with the CCD camera whose 25mm focal lens can capture detailed figure around 10cm×8cm area at 26cm objective distance. The camera is connected to a GigE host adapter with RJ45 connector and controlled by software named *FlyCapture* Software Development Kit (SDK), which provides a common software interface to control and acquire images for FLIR cameras under 32- or 64-bit Windows or Linux system. Besides the CCD camera system, a LimoStudio 700W photography lighting system is chosen to provide high-quality and uniform light on the specimen. A white back drop is hanging behind the specimen for a clean background in favor of following analysis. The setup of DIC system of diamond specimen is shown in Figure 3.19, an standard setup also used for hexagon specimen.

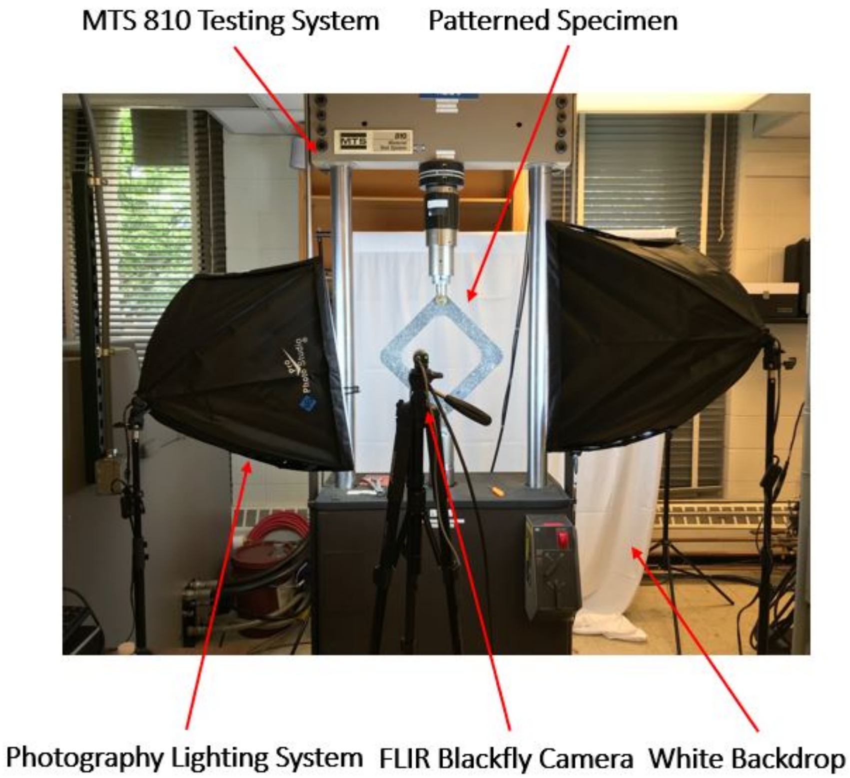

Figure 3.19: Setup of DIC Method

The detailed procedure of image acquisition for DIC approach is summarized as follows:

1. Clean the surface of specimen and paint with black color as background, then make tiny white particles with filters refining the particles. Leave the paint until dry. It is recommended to use spray painting with flat finish to avoid reflection.
2. Stop the test and remove the applied displacement on specimen
3. Mount the CCD camera and lights in front of the crack location
4. connect CCD camera with PC by Ethernet cable and open *FlyCapture* Software

5. Adjust the distance between camera and specimen to make sure the crack area is clearly observed in *FlyCapture* Software
6. Take a picture before loading as the reference figure
7. Applied the maximum displacement to specimen and take a second picture as the deformed figure

3.5.4 DIC Analysis and Crack Length Calculation

The DIC analysis is performed by an open source program named *GOM Correlate*. Images of the non-deformed specimen (reference image), the deformed specimen (current image) are input into the software. Then the ROI is defined as the interested area. The analysis is performed on the ROI of current and reference images to obtain correspondence between material points by cutting the reference image into small subsections and finding the corresponding locations in current image. After finishing the calculation and defining the inspection sections along the crack, a plot of major strain verses length is generated for the defined sections. The length is scaled to the mm for determining crack length. The procedure is shown in Figure 3.20. The major strain describes the strain from the tip of precracks to the crack tip where it tends to have a turning point due to the plastic zone as illustrated in Figure 3.21, i.e. the rate of decrease of the strain is slow after the turning point. It should be noted that the plastic zone tends to extend the crack resulting to a longer crack length, thus the crack length is corrected by subtracting the radius of plastic zone which is calculated by Equation 3.4, where K is the SIF and σ_y is the yield strength of material. In order to simplify the calculation of the size of plastic zone, two assumptions are made: (1) since the size of plastic zone decreases slowly as the crack size increases, it is assumed that the size of plastic zone decreases linearly with the increasing of cycles under displacement control experiment; (2) the four cracks have the same size of plastic zone. The size of plastic zone before crack propagation is determined by calculating the SIF by Abaqus, while the size of plastic zone after structure failure is assumed to be 0. Then the linearity of the size of plastic zone verses cycles can be determined. It should be noticed that the discussed DIC method is suitable for measuring the length of a straight crack. If the crack has curvature, a series of section should be drawn with the assumption that the crack in each section is straight, and the length of curvature is simulated by adding up the length of each straight crack.

$$r_y = \frac{1}{2\pi}(\frac{K}{\sigma_y})^2 \tag{3.4}$$

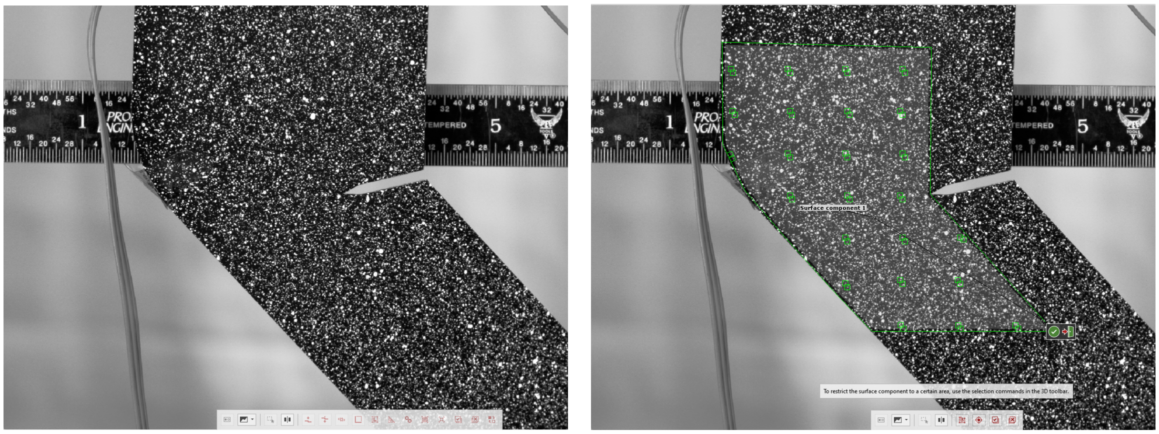

To restrict the surface component to a certain area, use the selection commands in the 3D toolbar.

(a) Original Image (b) Defined ROI

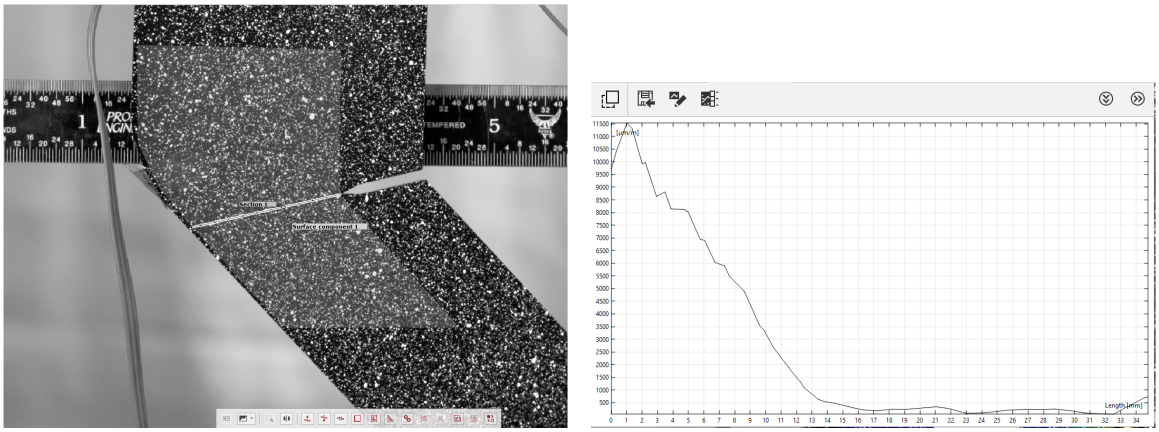

(c) Inspection Section (d) Strain v.s. Length

Figure 3.20: The Procedure of Applying DIC Method

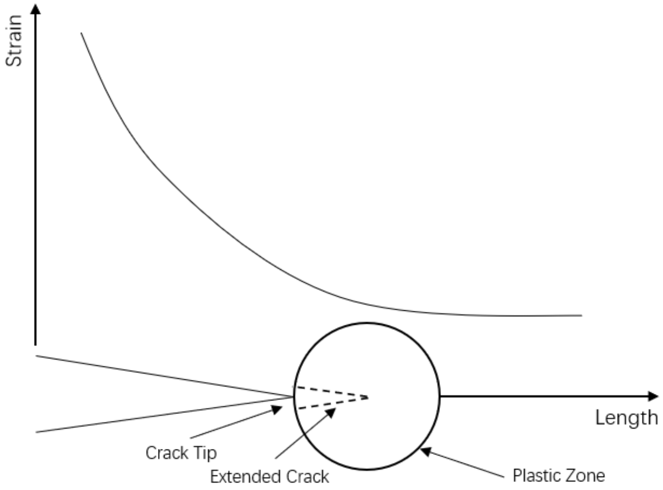

Figure 3.21: Illustration of the Change of Major Strain Verses Length

3.5.5 Result and Discussion

The following section demonstrates the DIC results of the fifth hexagon test. Figure 3.22 shows the correction of radius of plastic zone. The SIF without crack growth is simulated by Abaqus and the radius of 0 cycles is calculated which is 2.3 *mm*. The structure fails at 867111 cycles where the radius of plastic zone is assumed to be 0. With the assumption that the radius of plastic zone has linear relation with applied cycles, the correction is calculated and applied to correct the DIC results shown in Table 3.5, where the crack length measured by machinist scale and DIC is compared followed by the percentage error. The DIC method is implemented from 100000 cycles to 800000 cycles. It should be noted that the DIC results of left top and right bottom at 800000 cycles are not available since the crack cannot be opened. As shown in Table 3.5, the percentage error is relatively large when the crack is small. With the propagation of crack, the percentage error decreases resulting in a mean error around 9.71% with standard deviation around 7.36% for DIC method, which meets our expectation and the trend of crack length from DIC follows the results from machinist scale very well as shown in Figure 3.23. The DIC method is suitable for fatigue test or monitoring of real world structure where crack length is the key factor.

The measurement from CV method is also included in Table 3.5 for comparison. Overall, the CV method has a better performance regarding the mean of error and std of error.

Table 3.6 shows the DIC results of the fifth hexagon test using an alternative assumption, which assumes that the radius of plastic zone does not decrease with crack propagates. In other words, the radius is a constant which equals to the radius of plastic zone when four crack have no growth. The mean of error decreases to 5.24% while the std of error decrease to 4.53%. The alternative assumption with a constant radius increases the performance of DIC method, indicating that DIC method can be enhanced in the future by refining its assumptions.

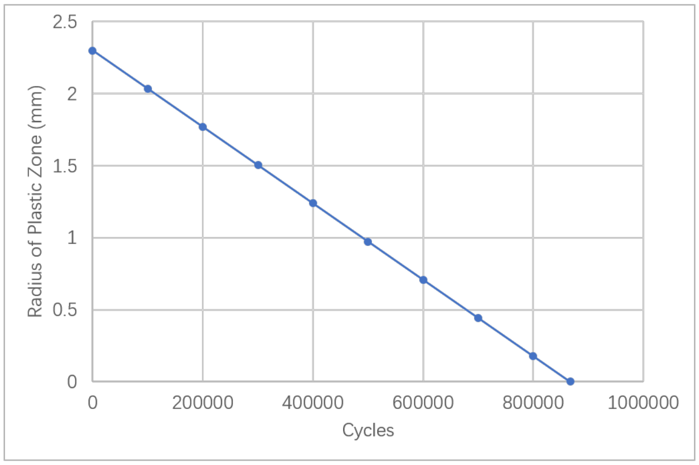

Figure 3.22: Correction of Radius of Plastic Zone

Cycles	*Left Top (MS;DIC;CV)*	*Error% (DIC;CV)*	*Left Bottom(MS;DIC;CV)*	*Error% (DIC;CV)*	*Right Top(MS;DIC;CV)*	*Error% (DIC;CV)*	*Right Bottom(MS;DIC;CV)*	*Error% (DIC;CV)*
100000	2.00; 2.56; 2.27	28.26; 13.50	2.30; 2.96; 2.19	28.92;4.78	2.65; 2.76; 2.42	4.34;8.68	2.40; 2.86; 2.81	19.38;17.08
200000	5.50; 5.93; 5.51	7.82; 0.18	5.50; 6.03; 5.22	9.64; 5.09	5.65; 5.73; 5.34	1.42; 5.49	4.50; 5.73; 4.43	27.34;1.55
300000	8.25; 8.80; 8.38	6.61; 1.57	8.00; 8.99; 7.79	12.44;2.63	8.50; 9.69; 8.38	14.06; 1.41	7.50; 8.89; 7.41	18.60; 1.20
400000	11.40; 11.16; 11.12	2.09; 2.46	11.00; 12.06; 11.89	9.64; 8.09	11.75; 12.56; 11.88	6.90; 1.11	9.80; 10.56; 9.81	7.76; 0.10
500000	13.25; 13.53; 12.80	2.08; 3.40	14.10; 15.03; 13.98	6.56;0.85	14.80; 16.02; 14.50	8.28; 2.03	11.80; 12.02; 11.69	1.91; 0.93
600000	14.70; 15.69; 15.29	6.74; 4.01	17.50; 18.49; 18.97	5.66; 8.40	19.00; 19.79; 17.90	4.16; 5.79	12.60; 13.79; 12.53	9.45; 0.55
700000	14.70; 16.06; 16.00	9.23; 8.84	23.50; 24.76; 22.93	5.34; 2.42	25.00; 26.06; 26.14	4.22; 4.56	12.60; 14.05; N/A	11.56; N/A
800000	14.70; N/A; N/A	N/A; N/A	30.75; 32.32; 31.92	5.11; 3.80	31.50; 33.32; 32.16	5.78; 2.09	12.60; N/A; N/A	N/A; N/A
	Mean of Error% (DIC;CV)				9.71; 4.23			
	Std of Error% (DIC;CV)				7.36; 3.98			

Table 3.5: Comparison of Crack Length of Machinist Scale, DIC Method with Varying Radius of Plastic Zone, and CV Method of the Fifth Hexagon Experiment (unit: mm; MS = Machinist Scale; DIC = Digital Image Correlation; CV = Computer Vision)

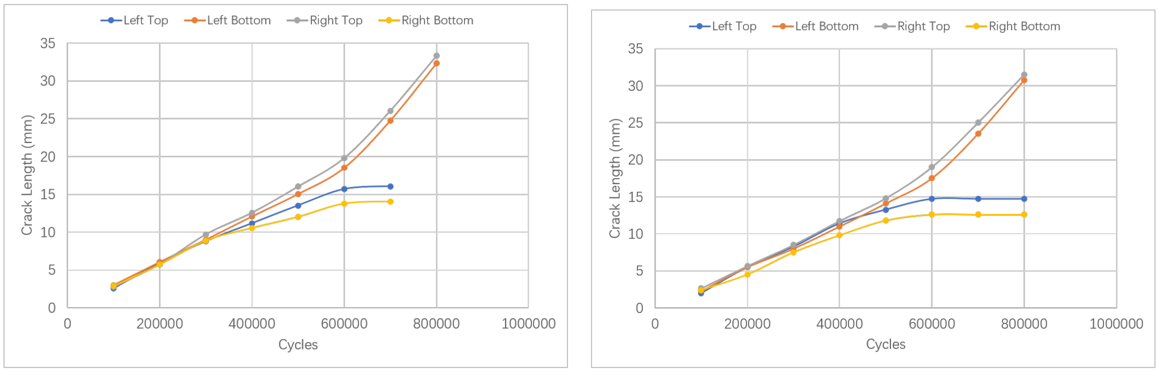

(a) Crack Length by DIC

(b) Crack Length by Machinist Scale

Figure 3.23: Comparison of Crack Length of the Fifth Hexagon Experiment (Left: DIC, Right: Machinist Scale)

Cycles	*Left Top (MS;DIC;CV)*	*Error% (DIC;CV)*	*Left Bottom(MS;DIC;CV)*	*Error% (DIC;CV)*	*Right Top(MS;DIC;CV)*	*Error% (DIC;CV)*	*Right Bottom(MS;DIC;CV)*	*Error% (DIC;CV)*
100000	2.00; 2.30; 2.27	15.00; 13.50	2.30; 2.70; 2.19	17.39;4.78	2.65; 2.50; 2.42	5.66;8.68	2.40; 2.60; 2.81	8.33;17.08
200000	5.50; 5.40; 5.51	1.82; 0.18	5.50; 5.50; 5.22	0.00; 5.09	5.65; 5.20; 5.34	7.96; 5.49	4.50; 5.20; 4.43	15.56;1.55
300000	8.25; 8.00; 8.38	3.03; 1.57	8.00; 8.20; 7.79	2.50;2.63	8.50; 8.90; 8.38	4.71; 1.41	7.50; 8.10; 7.41	8.00; 1.20
400000	11.40; 10.10; 11.12	11.40; 2.46	11.00; 11.00; 11.89	0.00; 8.09	11.75; 11.50; 11.88	2.13; 1.11	9.80; 9.50; 9.81	3.06; 0.10
500000	13.25; 12.20; 12.80	7.92; 3.40	14.10; 13.70; 13.98	2.84;0.85	14.80; 14.70; 14.50	0.68; 2.03	11.80; 10.70; 11.69	9.32; 0.93
600000	14.70; 14.10; 15.29	4.08; 4.01	17.50; 16.90; 18.97	3.43; 8.40	19.00; 18.20; 17.90	4.21; 5.79	12.60; 12.20; 12.53	3.17; 0.55
700000	14.70; 14.20; 16.00	3.40; 8.84	23.50; 22.90; 22.93	2.55; 2.42	25.00; 24.20; 26.14	3.20; 4.56	12.60; 12.20; N/A	3.17; N/A
800000	14.70; N/A; N/A	N/A; N/A	30.75; 30.20; 31.92	1.79; 3.80	31.50; 31.20; 32.16	0.95; 2.09	12.60; N/A; N/A	N/A; N/A
	Mean of Error% (DIC;CV)				5.24; 4.23			
	Std of Error% (DIC;CV)				4.53; 3.98			

Table 3.6: Comparison of Crack Length of Machinist Scale, DIC Method with Constant Radius of Plastic Zone, and CV Method of the Fifth Hexagon Experiment (unit: mm; MS = Machinist Scale; DIC = Digital Image Correlation; CV = Computer Vision)

3.6 Strain Monitoring

3.6.1 Introduction

In order to understand the change of rigidity during the hexagon experiment, strain gauges are employed in the third, fourth and fifth hexagon fatigue test to capture strain. A data acquisition system from National Instrument (NI) is used in the test, which is able to track small resistance change in strain gauges and record the streaming data from strain gauges. The data acquisition system is configured through *LabView* software and validated in the third test of hexagon specimen and then applied to the fourth and fifth hexagon specimen test. The collected data from strain gauges provides another piece of evidence for the BNs. The configuration of data acquisition system, setup of strain gauges as well as analysis results are explained in the following sections.

3.6.2 Literature Review

Strain gauges have a long history of being widely used in testing and structure health monitoring including aerospace, civil engineering, and marine engineering disciplines. In aerospace, strain gauges are usually attached to a load-bearing component to measure stresses along the path of wing deflection. In the low-speed wind-tunnel experiments on sharp-edged delta wings conducted by *Earnshaw and Lawford* (1966), strain gauges were used to investigate the forces and moments, and normal-force fluctuations. Strain gauge has also been used to monitor the structure health of bridges. *Wong* (2004) introduced a wind and structural health monitoring system integrating more than 350 measurement channels including strain gauge sensory system and data acquisition system, which is applied to monitor the structure conditions of Tsing Ma Bridge, Kap Shui Mun Bridge and Ting Kau Bridge in Hong Kong. *Nakamura and Suzumura* (2012) employed strain gauges to analyze the stress concentration factor at the sharp edge of the pits of corroded bridge wires. In the field of naval architecture and marine engineering, *Lee* (2018) applied strain gauge to evaluate the stability of marine propulsion shafting system. *Ritch et al.* (2008) collected data from 120 strain gauges on a ship panel to measure and evaluate local ice pressure. Strain gauge has also been applied in passive structural health monitoring of a high-speed naval ship by record the ambient vibrations with five strain gauges at a 100 Hz sampling frequency, *Sabra and Huston* (2011). The wide application of strain gauges inspired using strain gauge in the experiment of hexagon specimens to monitor the changes of strain field during structure degradation.

3.6.3 Wheatstone Bridge

Strain gauges convert a mechanical strain into a small change of an electrical resistance. Measuring such a small change in resistance is challenging considering the low signal level and unknown noises. Fulfilling a strain measurement successfully requires Wheatstone bridge since the resistance change is too small to be measured by ohmmeter. The basic structure of Wheatstone bridge is shown in Fig 3.24 containing four arms with one resistance on each arm, a excitation voltage, and a galvanometer which measures current accurately. The Wheatstone bridge contains two parallel voltage divider circuits, R_1 R_2 and R_3 R_4, forming a passive and balanced electrical circuits. The balanced electrical circuit can be used to measure an unknown resistance by replacing one of the four arms with the unknown resistance. The output of Wheatstone bridge (V_0) is measured by Equation 3.5. With a balanced resistance, the output is zero while a nonzero output is generated by replacing any resistance in the Wheatstone bridge with an active strain gauge. There are three types of strain gauge configuration, quarter bridge, half bridge and full bridge, determined by the number of active strain gauges in Wheatstone bridge. The configuration of strain gauge applied in the experiment is a quarter-bridge strain gauge illustrated in Figure

3.25. It can measure axial or bending strain by replacing R_4 with a strain gauge measuring the tensile strain. The compensating strain gauge for the effect of temperature is not deployed in this application since the room temperature is stable and the strain gauges used in this research are capable of compensating temperature on steel structures.

$$V_0 = [\frac{R_3}{R_3 + R_4} - \frac{R_2}{R_1 + R_2}]V_{ex} \tag{3.5}$$

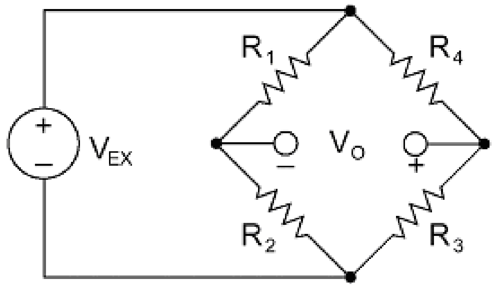

Figure 3.24: Diagram of Wheatstone Bridge

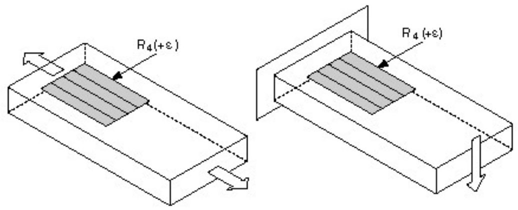

Figure 3.25: Configuration of Strain Gauge

3.6.4 Strain Gauges and Data Acquisition System

OMEGA uniaxial pre-wired strain gauges KFH-3-350-C1-11L3M3R with 350 Ω resistance are employed in the fatigue test as shown in Figure 3.26. It has a grid with $3mm \times 2mm$ measuring area carried by rugged polyimide with dimension $7.4mm \times 3.9mm$ The measuring grid is formed by etching constantan foil, which is then completely sealed in a carrier medium composed of polyimide film making them durable in the experiment. Their rugged construction and flexibility make them suitable for highly accurate static and dynamic measurement. The strain gauges are compensated for steel and the pre-wire makes them easy to be installed.

A National Instrument measurement system containing of a NI 9236 and a cDAQ-9181 are adopted for collecting data from strain gauges in this test as shown in Figure 3.27. NI 9236 is a 350ohm, quarter bridge input module with 8 channels which enables it to connect and measure eight strain gauges simultaneously at a high speed. It can read as much as 10 k samples per second on each channel. A build-in voltage excitation is included in NI 9236 for quarter-bridge sensors. cDAQ-9181 is a chassis designed for small and distributed sensor measurement with one slot to connect one NI 9236 modules. The chassis controls the timing, data transfer through communicating with computer by Ethernet. The system allows synchronized, high-speed measuring for dynamic strain on all channels simultaneously. The data recording system is driven by NI-DAQmx and controlled by a LabView algorithm as demonstrated in Figure 3.28. The DAQ Assistant is an API from NI-DAQmx aiming to help the users set up measurements, triggering and data logging straightforwardly. It let user configure measurement tasks, channels, customized timing, triggering, and scales without lengthy programming. DAQ Assistant outputs the measurement from strain gauge as an input to Write To Measurement File, which documents the data with desired format on hard drive. The Iterations Panel is included to demonstrate the counting of iterations. Since the test is running on 7 Hz and the strains don't change in a short period, a lag is added and set as 20000 *milliseconds* to record the strain once every 20 *seconds*. The 20 *seconds* delay can not only reduce recording repeated data but also keep the data consistent meanwhile. In other words, the system measures for 1 second with the sample rate of 1000 Hz every 20 *seconds*. The entire function is enclosed in a while loop with the stop condition as $N \leq 750$ which is able to cover 100000 cycles in a hexagon experiment.

Figure 3.26: OMEGA Uniaxial Pre-wired Strain Gauges

(a) NI 9236

(b) cDAQ-9181

Figure 3.27: Measurement System from National Instrument

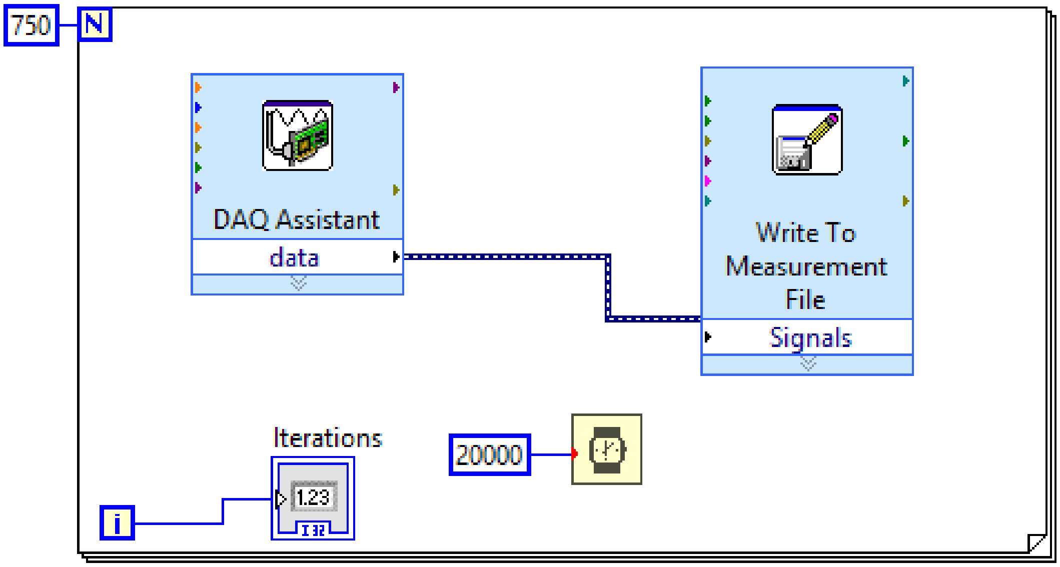

Figure 3.28: LabView Program for Data Acquisition with Strain Gauges

3.6.5 Test Setup

The strain gauge measuring system is validated in the third hexagon experiment and deployed in the fourth and fifth hexagon tests. Four OMEGA uniaxial pre-wired strain gauges KFH-3-350-C1-11L3M3R are glued on the center of each side of the vertical beams as shown in Figure 3.29. The location is selected to be away from the crack propagation area to reflect the structure status without influence from crack propagation. In order to have a stable connection, the surface where strain gauges are glued on is flattened by wired EDM resulting a smooth surface for deploying strain gauges. The dimension of the flattened area is also included in Figure 3.29.

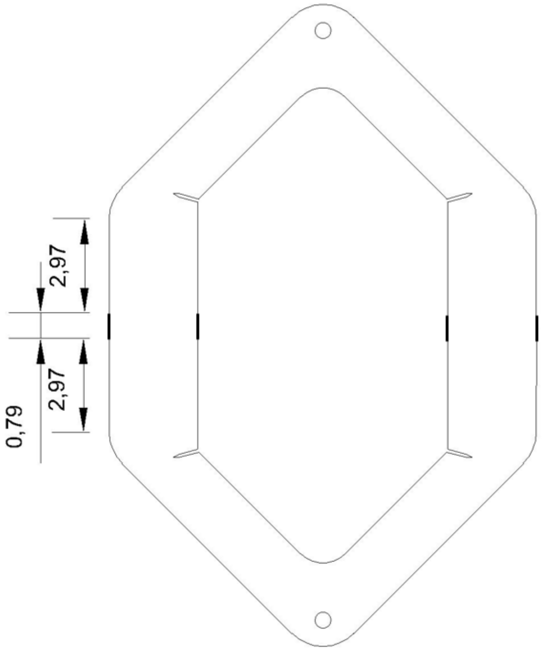

Figure 3.29: Strain Gauge Locations (unit: *inch*)

Surface cleanness is critical for measuring strains accurately. The fourth and fifth hexagon experiment involve the DIC measurement. DIC requires painting patterns on specimen surface. The flatted area is covered by tape during painting to avoid any particles which may negatively affect the measurement of strain gauges. The operation procedure contains surface preparation, mounting strain gauges, and setting up data acquisition system is summarized as follows.

1. Surface Preparation
    1. (a) Remove any painting or coatings by sand paper with 400 grit or higher; use 220 grit sand paper for any necessary coarse cleaning
    2. (b) Clean the surface gently with a metal conditioner and wipe with a clean tissue to make sure no dust particles are in the strain gauges area
2. Strain Gauges Mounting
    1. (a) Mark on the specimens for strain gauge orientation and alignment
    2. (b) Remove strain gauges from package and inspect for any defect by eyes
    3. (c) Glue strain gauges to the surface; apply constant pressure until the contact is strong
    4. (d) Cover the strain gauges with plastic membrane to prevent dust
3. Data Acquisition System Setup
    1. (a) Insert NI 9236 into chassis cDAQ-9181; Connect the chassis with computer by Ethernet and power supply with power cord
    2. (b) Connect the wires of strain gauges to NI 9236
    3. (c) Open LabView program, configure the measurement in DAQ Assistant
    4. (d) Start the data acquisition system by running LabView program; then start fatigue test

3.6.6 Results of Strain Measurement

The strain gauge is deployed aiming to understand the status of hexagon specimen during complex multi-degradation. Each of the four strain gauges is composed a quarter-bridge and measure the strain every 20 seconds with 1000 Hz sample rate.

The data is stored as text in a lvm file which is explored by Pandas Dataframe supported by Python. Due to the cyclic loading, the maximum strain corresponding to the maximum displacement is selected and extracted to monitor the status of the structure. With the maximum and minimum strain, the maximum stresses θ_{max} and minimum stresses θ_{min} are obtained and used to calculate the membrane and bending stresses. The associated equations are shown in Equation 3.6, where θ_m and θ_b represent membrane and bending stresses respectively. The reaction force can be calculated by multiplying membrane stress with the area of cross section where strain gauges are deployed. Figure 3.30a shows the strain of the fifth hexagon experiment with respect to the applied cycles. From the left to the right, the strain is numbered as 0, 1, 2, and 3 with respect to the location of strain gauges. Due to the symmetric design, strain 0 and strain 3 are increasing while strain 1 and strain 2 are decreasing with applied cycles; the bending and membrane stresses of the two beams are decreasing while bending stress has a larger slope compared to membrane stress. It should be noticed that the bending stress decreases to 0 and starts to grow again around 740000 cycles, which corresponds to the intersection of strain 0, 3 and strain 1, 2 in Figure 3.30a. The interesting phenomenon is illustrated in Figure 3.31, where the arrow indicates the direction of the stress and the length of arrow demonstrates the absolute value of the stress. Since the design is symmetric, Figure 3.31 only shows the left beam of the hexagon specimen. From Figure 3.31a to Figure 3.31e, with the growing of cracks, S_1 is decreasing while S_2 is increasing. After S_2 becomes positive and keeps increasing, S_1 and S_2 are identical at a specific point resulting in pure membrane stress and the bending stress switches orientation in Figure 3.30b. The reaction force is calculated as shown in Figure 3.30c and compared to the maximum reaction force indicated by MTS testing system which have similar trend and matches very well. The small difference could come from the fact that the reaction force recorded by MTS testing system is static force, i.e. the test is stopped and the maximum displacement is applied to record the maximum reaction force, while the strain gauges measurement indicates the dynamic force. The strain gauges successfully monitor the complex change inside the hexagon specimen during the experiment. The rest results of strain gauge measurement for the third and fourth tests are included in the following section of experiment results.

$$\begin{aligned} \theta_m &= \frac{1}{2}(\theta_{max} + \theta_{min}), \\ \theta_b &= \frac{1}{2}(\theta_{max} - \theta_{min}). \end{aligned} \tag{3.6}$$

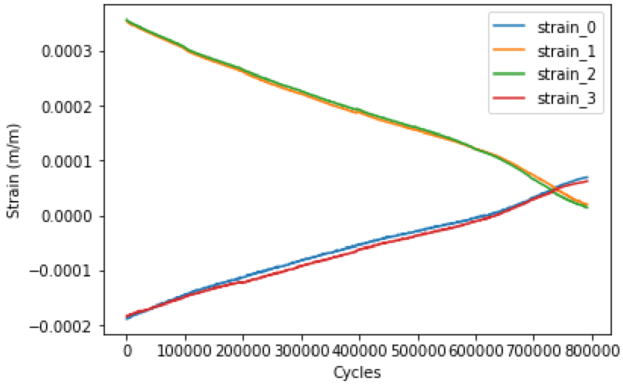

(a) Measured Strain of The Fifth Hexagon Experiment

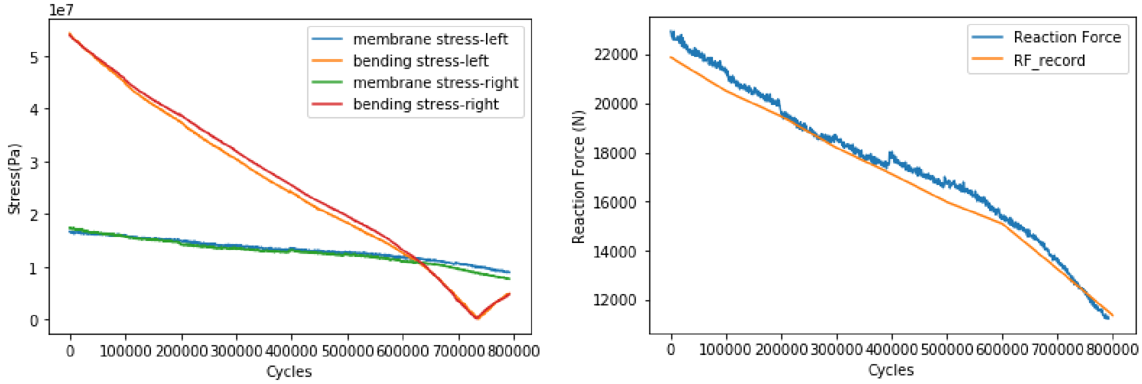

(b) Membrane and Bending Stress of The Fifth Hexagon Experiment

(c) Comparison of Reaction Force

Figure 3.30: Results from Strain Gauge Measurement of the Fifth Hexagon Experiment

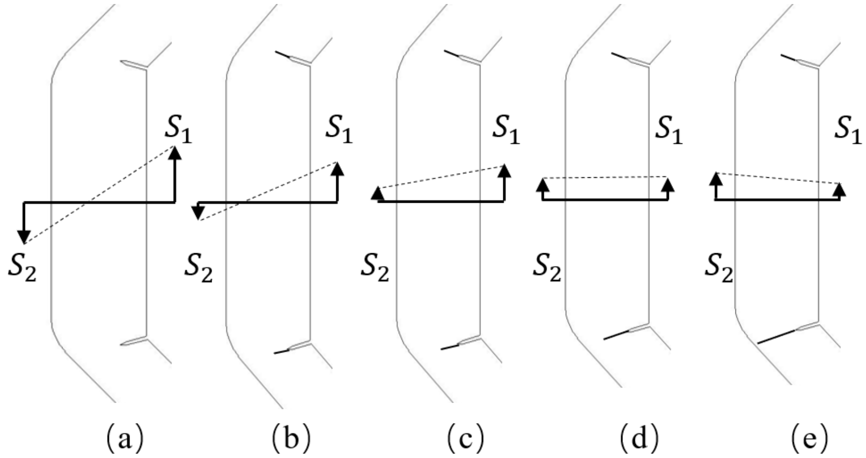

Figure 3.31: Analysis of Stress Change Over the Experiment

3.7 Experiment Results

In experiment exploration, two diamond specimens has been design and machined first. Unfortunately, the cracks of diamond specimen didn't propagate as expected even using wired EDM to make the crack tip sharp and loading to two million cycles. Then hexagon specimens have been designed as an upgraded version and machined by waterjet as well as wired EDM. To measure crack length, two methods are developed including computer vision method and DIC method. Strain gauge measurement is applied to understand the complex strain status of specimen undergoing degradation. The first hexagon specimen is tested mainly for validating the specimen design, so the crack length is only measured by machinist scale rather than the developed methods; The second hexagon specimen is for applying the computer vision and DIC method. The third experiment hexagon specimen focuses on validating the system measuring strain gauges. The fourth and fifth hexagon test employ all the developed methods including computer vision and DIC methods for crack length and strain gauges for structure status. The recorded data of the five hexagon experiments are listed in the following sections.

3.7.1 The First Hexagon

Note that the first hexagon specimen has four horizontal pre-cracks which is unable to have the cracks growing straight out of the pre-crack on the specimen. Thus, the design of following four hexagon specimens changes slightly by orienting the pre-crack of 15° to ensure the grown crack straight out of the pre-crack. The first hexagon experiment focuses on validating the design so the crack length is measured only by machinist scale and the record is not refined, i.e. the cycles between records are not uniform, as shown in Table 3.7. In the first hexagon test, the specimen is preloaded with 8.6 kN to guarantee the bolt and hole have a tight contact and the specimen is always under tension cycles. Then the amplitude is set as 0.25 mm resulting in 23.44 kN maximum reaction force initially. The maximum and minimum displacements in a period of the first hexagon experiment are extracted and plotted in Figure 3.32, which demonstrates the displacement in 190 minutes showing that the experiment is under displacement control. The rest four experiments have the same test setup leading to a fixed maximum and minimum displacement. The maximum reaction force decrease smoothly with applying cycles onto specimen as shown in Figure 3.33b. The crack length is measured by machinist scale with markings 0.5mm and plotted in Figure 3.33a. From the beginning to around 670000 cycles, the crack lengths have minor differences. With more cycles applied, the left top and right bottom cracks become dominant and the growth of left bottom and right top cracks are shadowed by the dominant cracks. The first experiment successfully verifies that the crack can propagate with hexagon-shaped design and the cracks interact with each other during deterioration process, which satisfies the goal of the experimental design.

3.7.2 The Second Hexagon

The second hexagon experiment employs the developed computer vision and DIC method to measure crack length. The specimen is preloaded with 9.69 kN to guar-

Cycles	*Left Top (MS)*	*Left Bottom (MS)*	*Right Top (MS)*	*Right Bottom (MS)*	*Maximum Reaction Force*
369706	2.50	4.00	4.00	5.50	21.22
569706	10.80	11.80	9.50	11.80	19.14
669706	14.20	14.50	12.50	16.00	17.89
769706	17.00	16.80	13.60	19.40	17.01
869706	21.10	18.00	14.00	24.00	15.28

Table 3.7: Recorded Crack Length of the First Experiment of Hexagon Specimen (unit: Length mm; Force kN; MS = Machinist Scale)

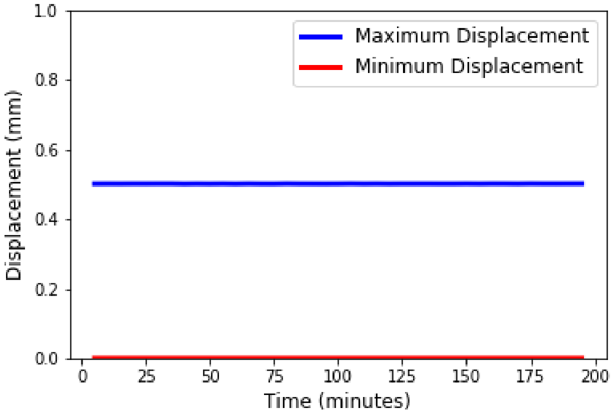

Figure 3.32: Maximum and Minimum Displacement in A Period of the First Hexagon Test

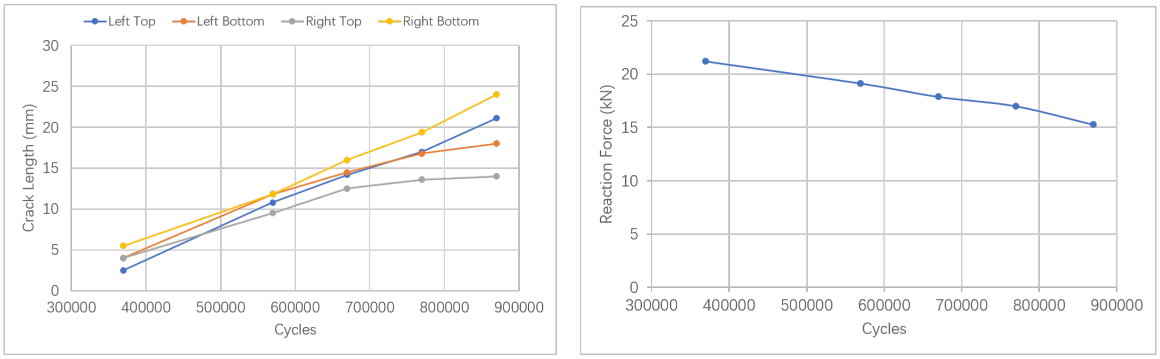

(a) Crack Length v.s. Cycles of The First Hexagon Test

(b) Maximum Reaction Force v.s. Cycles of The First Hexagon test

Figure 3.33: Plot of Crack Length and Maximum Reaction Force From The First Experiment of Hexagon Specimen, measured by machinist scale

antee the bolt and hole have a tight contact without slack. Then the amplitude is set as 0.25 *mm* resulting in 22.16 *kN* maximum reaction force. The crack length and maximum reaction force is recorded every 100000 cycles to have a detailed record of crack propagation. The images for the computer vision analysis are taken by GoPro while the images for DIC method are captured by a CCD camera. Since the crack is straight, a machinist scale with markings 0.5 *mm* is also used for measuring the crack length. Figure 3.35a plots the propagation of four crack length with respect to the applied cycles. From the beginning to 600000 cycles, the four crack length has negligible differences since the symmetric design and identical starting length of the precracks. However, with increasing cycles, the left bottom crack becomes dominant among the four cracks. At 1147505 cycles, the left bottom crack has propagated through the width of the bar as demonstrated in Figure 3.34. Interestingly, the bottom crack on each side is dominant, which means the left bottom crack is dominant between left bottom and top cracks; right bottom crack is dominant between right bottom and top cracks. The maximum reaction force is recorded to reflect the rigidity and indicate the threshold of structure failure for the future experiments. The maximum reaction force decreases smoothly from the beginning to a million cycles while an abrupt drop appears around 1.1 million cycles with a steeper slope. The left bottom crack is broken at 1.2 million cycles resulting in a 1.9 *kN* maximum reaction force. This means the specimen still has the capability to take loads even it is pretty small compared to the capability at the beginning. The experiment successfully simulated the dependence and interaction among component in deterioration with a structural redundancy mimicking the properties of complex marine structures.

The crack lengths are also measured by computer vision and DIC method as shown in Table 3.8. Since the cracks barely open when close to break, images cannot be captured for further analysis resulting in several N/A in the table. The crack length measurement from computer vision method and DIC method is plot in Figure

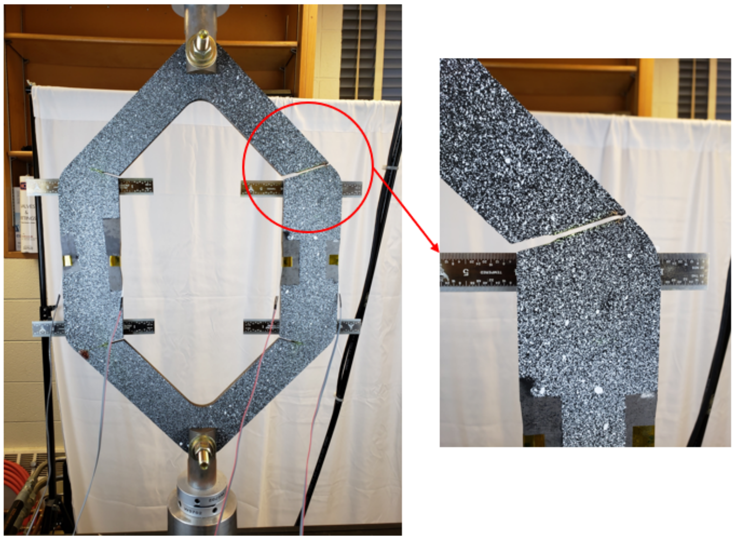

Figure 3.34: Cracked Hexagon Specimen(backside)

Cycles	*Left Top (MS;DIC;CV)*	*Error%*	*Left Bottom(MS;DIC;CV)*	*Error%*	*Right Top(MS;DIC;CV)*	*Error%*	*Right Bottom(MS;DIC;CV)*	*Error%*	*MRF*
100000	2.25;2.89;2.12	28.52;5.77	2.20; 3.09; 1.68	40.53;23.64	2.50; 2.19;N/A	12.33;N/A	2.25; 2.59; N/A	15.18;N/A	20.02
200000	5.40;5.58 ;4.77	3.40;11.67	5.40; 6.28; 4.60	16.36;14.81	5.40; 6.58;5.01	21.91;7.22	4.70; 5.58; 4.22	18.79;10.21	19.36
300000	8.00;8.27 ;7.38	3.44;7.75	8.30; 8.67; 7.25	10.20;12.65	8.70; 8.48;7.43	2.59;14.60	8.00; 8.87; 6.05	10.94;24.38	17.73
400000	10.90;10.97;10.16	0.61;6.79	11.50; 11.77; 10.01	2.32;12.96	11.30; 10.97;9.22	2.95;18.40	10.50; 11.07; 9.06	5.40;13.71	17.04
500000	13.60;13.26;12.65	2.51;6.99	14.00; 14.06; 12.49	0.42;10.79	12.50; 12.86;12.38	2.87;0.96	12.40; 12.96; 11.75	4.50;5.24	16.35
600000	15.30;14.05;14.42	8.17;5.75	15.70; 16.05; 15.20	2.23;3.18	14.20; 14.35;13.08	1.06;7.89	14.30; 15.85; 13.53	10.84;5.38	15.85
700000	16.40;16.54;17.86	0.86;8.90	18.20; 18.04; 18.52	0.87;1.76	14.90; 16.04;16.40	7.66;10.07	16.00; 17.24; 14.62	7.76;8.63	15.48
800000	17.20; 17.23;16.12	0.19;6.28	20.00; 20.83; 20.93	4.17;4.65	15.50; 16.63;15.19	7.31;2.00	17.10; 20.03; 16.60	17.15;2.92	15.06
900000	17.50; 18.42;19.06	5.29;8.91	23.40; 23.92; 22.06	2.24;5.73	15.50; 17.43;13.65	12.42;11.94	18.90; 20.63; 18.53	9.13;1.96	14.98
1000000	17.50; 18.62;N/A	6.38;N/A	27.30; 28.42; 27.84	4.09;1.98	15.50; 17.62;N/A	13.65;N/A	20.00; 20.92; N/A	4.58;N/A	14.13
1100000	17.70; N/A;N/A	N/A;N/A	32.50; 33.31; 31.95	2.49;1.69	17.00; 18.81;N/A	10.64;N/A	21.20; 21.81;N/A	2.87;N/A	13.86
1147505	18.00; N/A;N/A	N/A;N/A	36.00; N/A;N/A	N/A;N/A	17.50; N/A;N/A	N/A;N/A	21.50; N/A;N/A	N/A;N/A	10.64
1200000	18.00; N/A;N/A	N/A;N/A	37.50; N/A;N/A	N/A;N/A	17.50; N/A;N/A	N/A;N/A	21.50; N/A;N/A	N/A;N/A	1.9
	Mean of Error% (DIC;CV)				7.96; 8.56				
	Std of Error% (DIC;CV)				8.08; 5.67				

Table 3.8: Recorded Crack Length of the Second Experiment of Hexagon Specimen (unit: Length mm; Force kN; MS = Machinist Scale; DIC = Digital Image Correlation; CV = Computer Vision; MRF = Maximum Reaction Force)

3.36. Even DIC results are more close to the measurement from machinist scale, both computer vision and DIC follows the trend of crack growth very well, resulting in 8.56% mean of error and 5.67% standard deviation of error for computer vision method, 7.96% mean of error and 8.08% standard deviation of error for computer vision method, which lays a solid foundation for applying there methods in the fourth and fifth tests. It should be noted that the measurement from CV method for right top drops from 700000 to 800000 cycles since the crack cannot open thoroughly due to the shadowing effect from the dominant crack. The computer vision measurement can be improved by increasing lighting and ensuring the camera lens is parallel with structure surface.

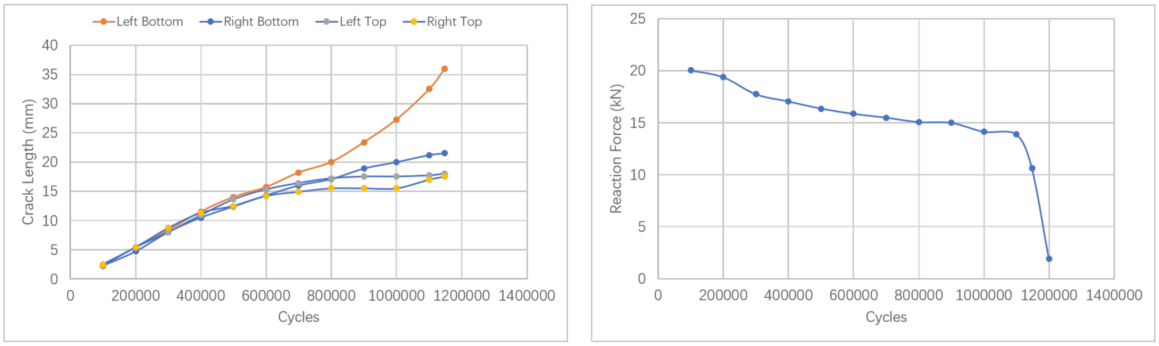

(a) Crack Length v.s. Cycles of The Second Hexagon Test

(b) Maximum Reaction Force v.s. Cycles of The Second Hexagon test

Figure 3.35: Plot of Crack Length and Maximum Reaction Force From The Second Experiment of Hexagon Specimen, measured by machinist scale

3.7.3 The Third Hexagon

The purpose of the third hexagon is verifying the application of strain gauges and data acquisition system so the crack length is only measured by machinist scale as shown in Table 3.9. Since the goal of the third test is validating the data acquisition system rather than collecting abundant data, a relatively larger pre-load is applied to shorten the test duration. The specimen is preloaded with 12 kN to guarantee a tight contact and the specimen is applied with tension cycles. Then the amplitude

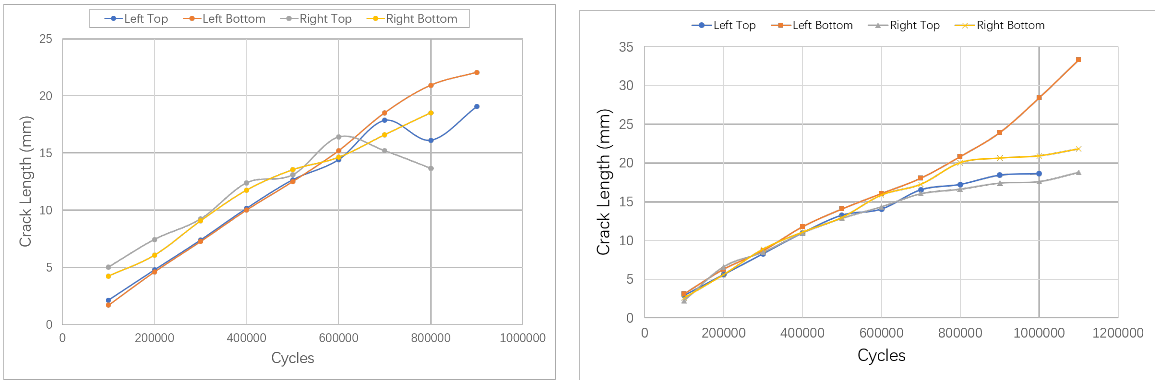

(a) Crack Length v.s. Cycles of The Second Hexagon Test by CV method

(b) Crack Length v.s. Cycles of The Second Hexagon Test by DIC method

Figure 3.36: Plot of Crack Length From The Second Experiment of Hexagon Specimen, measured by CV and DIC methods

is set as 0.25 mm resulting in 24.07 kN maximum reaction force. The crack length and maximum reaction force is recorded every 100000 cycles and the data from strain gauges is recorded for 1 $second$ every 20 $seconds$ with 1000 Hz sample rate. The crack lengths are similar from beginning to 200000 cycles and then the right top and left bottom crack start to dominant. The record of crack length and maximum reaction force stops at 700000 cycles since the gathered data is sufficient for validating strain gauge measurement.The strain gauge data is analyzed by program written in Python and plotted as shown in Figure 3.38. With respect to the location of strain gauges, the strain is numbered as 0, 1, 2, and 3 from the left to the right. The measured strain from strain gauge 0, 3 and strain gauge 1, 2 has similar trend due to the symmetric design and their deployment locations. With applying more cycles, the strain of 0 and 3, i.e. the outer side of two beams increase while the strain of inner side of two beams decrease due to crack propagation. As shown in Figure 3.38b, the membrane stress of left and right beams are similar during the degradation process as well as the bending stress of left and right beams. The membrane stress decrease slightly compared to the bending stress. The bending stress decreases to 0 and starts to grow again around 600000 cycles corresponding to the intersection of strain 0, 3 and strain

1, 2 in Figure 3.38a. The reaction force is calculated as shown in Figure 3.38c and compared to the maximum reaction force indicated by MTS testing system which have similar trend and matches well. The difference could come from the fact that the reaction force recorded by MTS testing system is static force, i.e. the test is stopped and the maximum displacement is applied to record the maximum reaction force, while the strain gauges measurement indicates the dynamic force. The strain gauges successfully monitor the complex change inside the hexagon specimen during the experiment and are applied in the fourth and fifth hexagon experiments.

Cycles	*Left Top (MS)*	*Left Bottom (MS)*	*Right Top (MS)*	*Right Bottom (MS)*	*Maximum Reaction Force*
100000	2.50	2.50	2.50	2.50	21.91
200000	4.50	5.00	5.00	4.50	21.34
300000	7.00	9.00	9.00	6.60	20.03
400000	9.20	12.30	13.20	8.30	18.36
500000	9.20	17.50	18.30	8.90	17.32
600000	9.20	24.40	25.70	9.20	14.72
700000	9.20	31.80	31.80	9.50	12.04

Table 3.9: Recorded Crack Length of the Third Experiment of Hexagon Specimen (unit: Length mm; Force kN; MS = Machinist Scale)

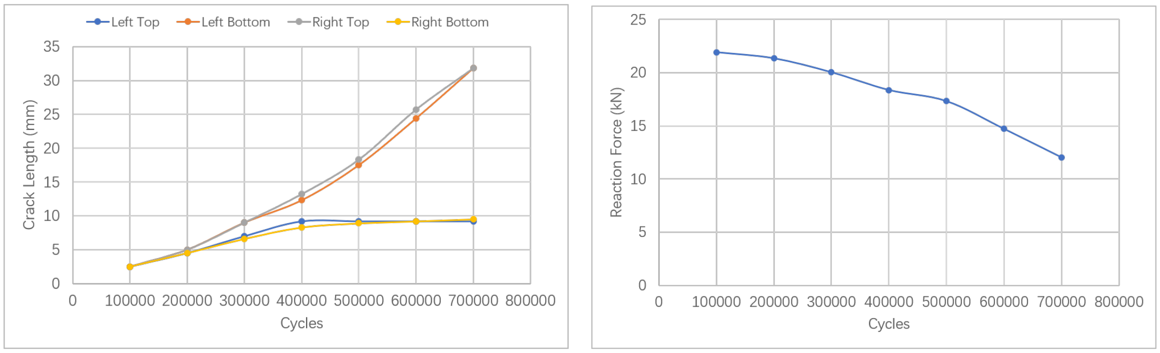

(a) Crack Length v.s. Cycles of The Third Hexagon Test

(b) Maximum Reaction Force v.s. Cycles of The Third Hexagon test

Figure 3.37: Plot of Crack Length and Maximum Reaction Force From The Third Experiment of Hexagon Specimen, measured by machinist scale

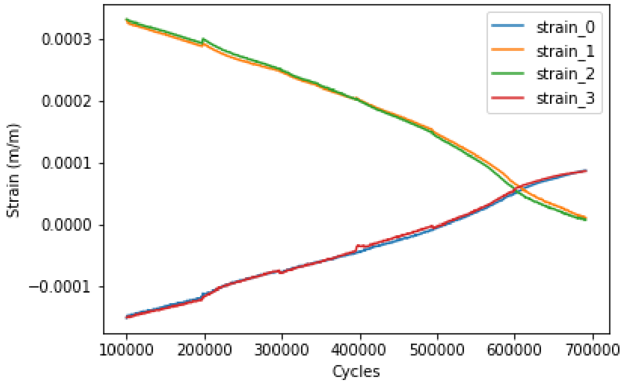

(a) Measured Strain of The Third Hexagon Experiment

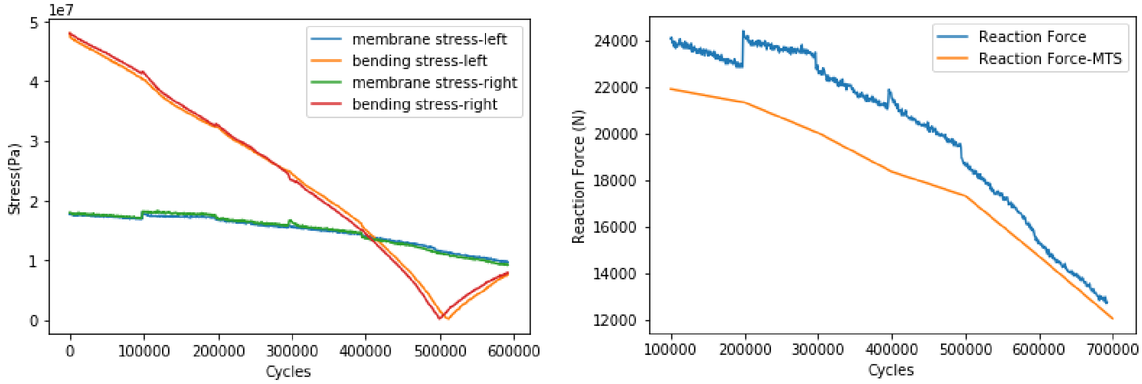

(b) Membrane and Bending Stress of The Third Hexagon Experiment

(c) Comparison of Reaction Force of The Third Hexagon Experiment (Strain Gauges verses MTS)

Figure 3.38: Results from Strain Gauge Measurement of the Third Hexagon Experiment

3.7.4 The Fourth Hexagon

The fourth hexagon experiment employs machinist scale, computer vision method, and DIC method for measuring crack length, as well as strain gauges for monitoring structural status during degradation. The specimen is preloaded with 9.1 kN so it is under tension cycles during deterioration process. 0.25 mm displacement amplitude is applied after preloading the specimen. The crack length and maximum reaction force is recorded every 100000 cycles and the data from strain gauges is recorded for 1 *second* every 20 *seconds* with 1000 hZ sample rate. As shown in Figure 3.39a, the crack length barely differ until 300000 cycles. Then, with applying more cycles, the left bottom and right top crack start to be dominant shadowing the growth of the left top and the right bottom crack. The maximum reaction force decreases smoothly along with increasing crack propagation. The left bottom crack breaks at 813097 cycles resulting in a 1.31 kN maximum reaction force as demonstrated in Figure 3.39b. The comparison of three measurement methods are displayed in Table 3.10 with 9.88% mean of error and 10.19% std of error for DIC method and 5.52% mean of error and 5.39% std of error for computer vision method. As shown in Figure 3.40, both measurement from computer vision and DIC follows the crack growth measured by machinist scale very well. The measured data of strain gauges labeled as 0 to 3 from left beam to right beam of hexagon specimen is plotted in 3.41a. The measured strain from strain gauge 0, 3 and strain gauge 1, 2 has similar trend due to the symmetric design and their deployment locations. Similar to the result in the third hexagon experiment, the bending stress approaches to 0 and starts to growing positively with respect to the moment that the strain on left and right side of each beam are identical. The reaction force is calculated as shown in Figure 3.41c having similar trend as the maximum reaction force indicated by MTS testing system. The difference in strain measurement could due to the relative small measurement area of strain gauge which is easily affected by unexpected particles which could come from the process of painting pattern for DIC method.

Cycles	*Left Top (MS;DIC;CV)*	*Error%*	*Left Bottom(MS;DIC;CV)*	*Error%*	*Right Top(MS;DIC;CV)*	*Error%*	*Right Bottom(MS;DIC;CV)*	*Error%*	*MRF*
100000	2.00; 2.48; 1.48	24.14; 26	2.00; 2.78; 1.91	39.14; 4.26	2.00; 2.68; 1.69	34.14; 15.5	1.90; 2.58; 1.83	35.94;3.68	20.81
200000	4.50; 4.46; 4.68	0.76; 4	4.70; 4.86; 4.72	3.52;0.42	5.20; 4.76; 4.88	8.35;6.15	4.50; 4.96; 4.19	10.35; 6.88	19.57
300000	7.60; 7.17; 7.56	5.94; 0.52	8.50; 7.95; 7.8	6.48; 8.23	8.10; 6.85; 7.57	15.45;6.54	7.10; 6.54; 7.03	7.76; 0.98	18.87
400000	9.80; 9.83; 9.89	0.32; 0.92	11.40; 11.03; 10.73	3.23; 5.88	11.40; 10.83; 11.37	4.98;0.26	9.50; 9.83; 9.55	3.49;0.53	17.61
500000	11.60;12.61; 10.96	8.74;5.52	15.40; 14.71; 14.81	4.45; 3.83	14.30; 14.61; 14.63	2.19; 2.31	11.50; 12.11; 10.13	5.34; 11.91	16.74
600000	12.20; 13.69; 12.12	12.27; 0.65	18.50; 17.70; 19.04	4.34; 2.92	18.60; 17.90; 19.30	3.77; 3.76	12.60; 13.89; 11.73	10.29; 11.91	15.33
700000	12.20; 13.98;N/A	14.59; N/A	26.80; 24.88; 24.29	7.16; 9.36	26.30; 25.28; 25.95	3.87; 1.33	12.60; 14.18; N/A	12.54; N/A	13.24
800000	12.20; N/A; N/A	N/A; N/A	33.50; 33.96; 35.8	1.38; 6.86	33.00; 33.46; 30.2	1.40;8.48	12.60; N/A; N/A	N/A; N/A	10.37
813097	12.20; N/A; N/A	N/A; N/A	37.50; N/A; N/A	N/A; N/A	33.00; N/A; N/A	N/A; N/A	12.60; N/A; N/A	N/A; N/A	1.31
	Mean of Error% (DIC;CV)				9.88; 5.52				
	Std of Error% (DIC;CV)				10.19; 5.39				

Table 3.10: Comparison of Crack Length of Machinist Scale and DIC method of the Fourth Hexagon Experiment (unit: Length mm; Force kN; MS = Machinist Scale; DIC = Digital Image Correlation; CV = Computer Vision; MRF = Maximum Reaction Force)

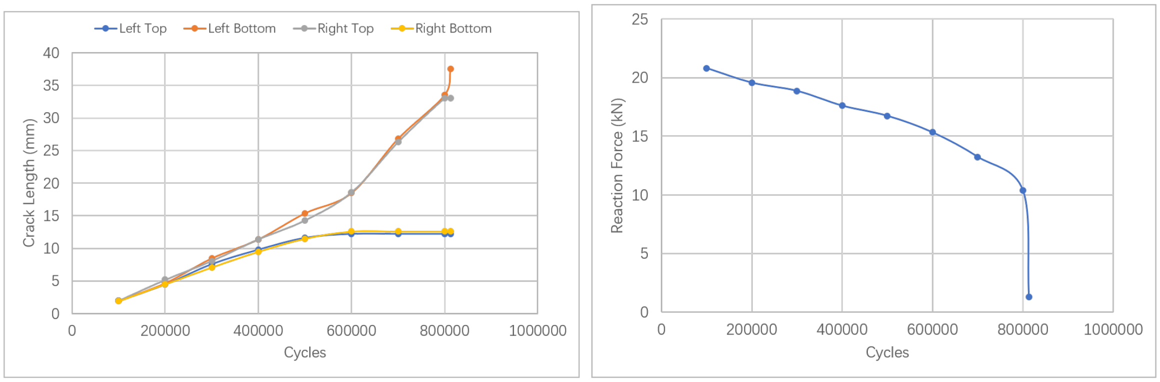

(a) Crack Length v.s. Cycles of The Fourth Hexagon Test

(b) Maximum Reaction Force v.s. Cycles of The Fourth Hexagon test

Figure 3.39: Plot of Crack Length and Maximum Reaction Force From The Fourth Experiment of Hexagon Specimen, Measured by Machinist Scale

3.7.5 The Fifth Hexagon

Similar to the fourth hexagon specimen, the crack length in the fifth test is also measured by machinist scale, computer vision method, and DIC method. Four strain gauges are bonded to the two sides of the specimen for recording the strain state during degradation. The results of computer vision method, DIC method, strain gauge measurement for the fifth hexagon specimen are discussed in Section 3.3, Section 3.5, and Section 3.6 respectively. The following tables and figures serve as complementary

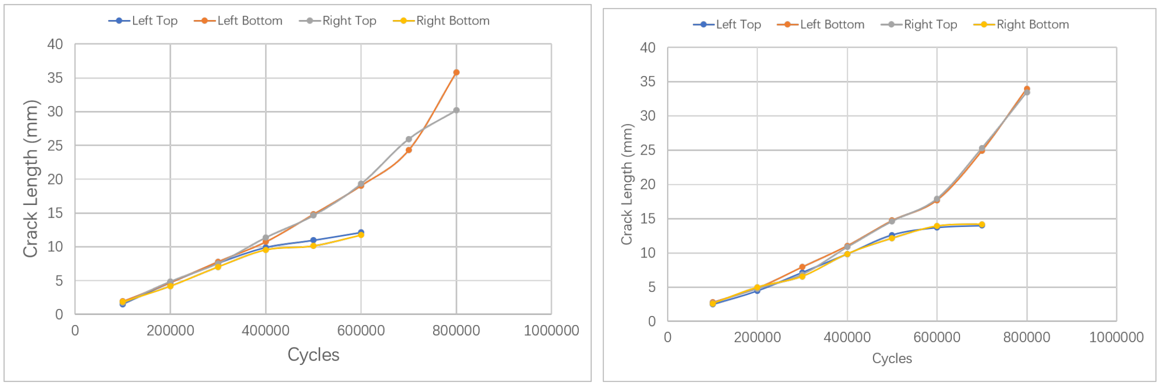

(a) Crack Length v.s. Cycles of The Fourth Hexagon Test by CV method (b) Crack Length v.s. Cycles of The Fourth Hexagon Test by DIC method

Figure 3.40: Plot of Crack Length From The Fourth Experiment of Hexagon Specimen, Measured by CV and DIC Methods

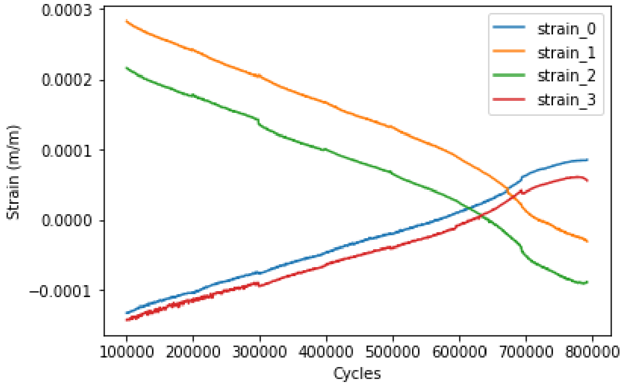

(a) Measured Strain of The Fourth Hexagon Experiment

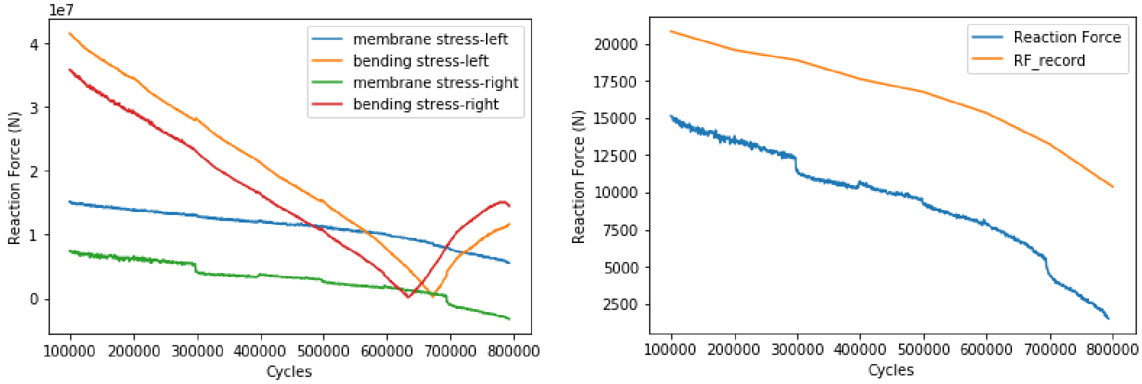

(b) Membrane and Bending Stress of The Fourth Hexagon Experiment (c) Comparison of Reaction Force of The Fourth Hexagon Experiment

Figure 3.41: Results from Strain Gauge Measurement of the Fourth Hexagon Experiment

results for the fifth hexagon experiment. The fifth hexagon specimen is preloaded at 9.3 kN to connect the specimen and the fixture bolt without slack and ensure the specimen is applied with tension cycles. Then a maximum displacement amplitude of 0.25 mm is set through MTS software resulting a maximum reaction force of 21.77 kN. Figure 3.43a plots the propagation of the four cracks with respect to the number of applied cycles measured by a machinist scale with markings of 0.5 mm. From the start of the test to 500000 cycles, the four crack lengths have only minor differences owing to the symmetric design and identical starting length of the precracks. However, with increasing cycles, the left bottom and right top cracks become dominant among the four cracks. At 867111 cycles, the right top crack has propagated through the width of the bar as demonstrated in Figure 3.42. It can be observed from Figure 3.42 that the left bottom crack is dominant on the left side while the right top crack is dominant on the right side. The maximum reaction force is recorded as shown in 3.43b to reflect the rigidity which decreases smoothly from the beginning to a 800000 cycles, followed by an abrupt drop with a steeper slope. The right top crack is broken at 867111 million cycles resulting in a 1.33 kN maximum reaction force. Even if the maximum reaction force at the end of the test is small compared to that at the beginning, the specimen still has the capability to take loads. The experiment successfully simulated the dependence and interaction among components in deterioration with a structural redundancy mimicking the properties of complex marine structures. Notably, the emergence of a large crack in the left bottom and right top appears to shield the other crack on the corresponding sides, slowing their growth. The recorded crack length and corresponding maximum reaction force are shown in table 3.11.

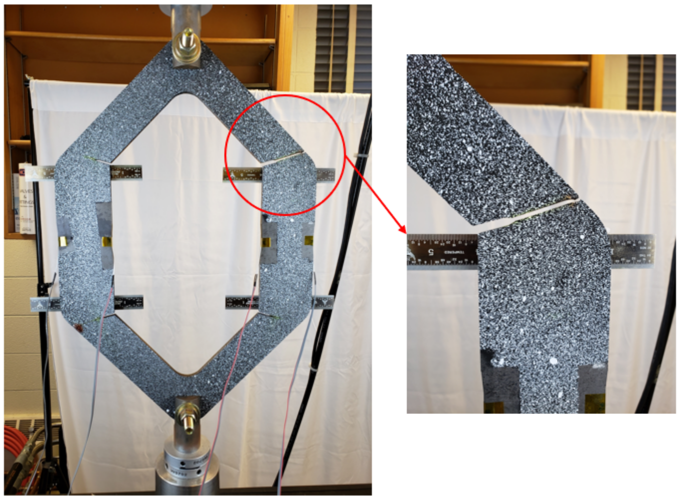

Figure 3.42: Cracked Fifth Hexagon Specimen (backside)

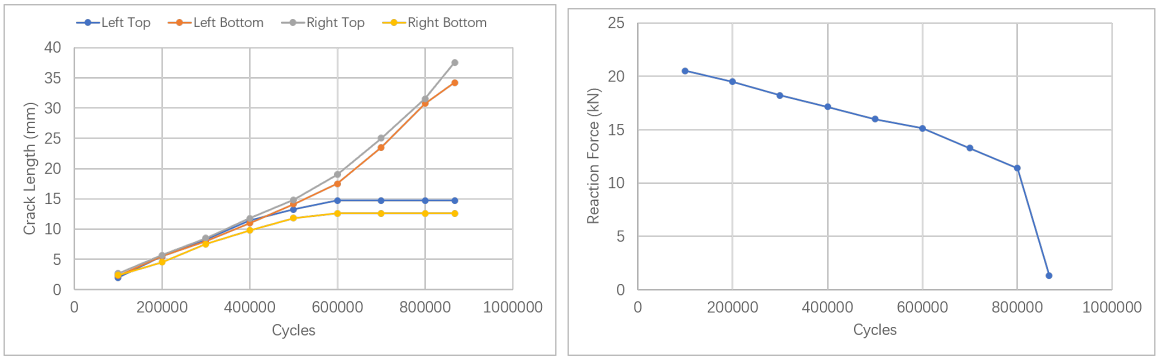

(a) Crack Length v.s. Cycles of The Fifth Hexagon Test

(b) Maximum Reaction Force v.s. Cycles of The Fifth Hexagon test

Figure 3.43: Plot of Crack Length and Maximum Reaction Force From The Fifth Experiment of Hexagon Specimen, Measured by Machinist Scale

Cycles	*Left Top (MS;DIC;CV)*	*Error% (DIC;CV)*	*Left Bottom(MS;DIC;CV)*	*Error% (DIC;CV)*	*Right Top(MS;DIC;CV)*	*Error% (DIC;CV)*	*Right Bottom(MS;DIC;CV)*	*Error% (DIC;CV)*	*MRF*
100000	2.00; 2.56; 2.27	28.26; 13.50	2.30; 2.96; 2.19	28.92;4.78	2.65; 2.76; 2.42	4.34;8.68	2.40; 2.86; 2.81	19.38;17.08	20.51
200000	5.50; 5.93; 5.51	7.82; 0.18	5.50; 6.03; 5.22	9.64; 5.09	5.65; 5.73; 5.34	1.42; 5.49	4.50; 5.73; 4.43	27.34;1.55	19.48
300000	8.25; 8.80; 8.38	6.61; 1.57	8.00; 8.99; 7.79	12.44;2.63	8.50; 9.69; 8.38	14.06; 1.41	7.50; 8.89; 7.41	18.60; 1.2	18.20
400000	11.40; 11.16; 11.12	2.09; 2.46	11.00; 12.06; 11.89	9.64; 8.09	11.75; 12.56; 11.88	6.90; 1.11	9.80; 10.56; 9.81	7.76; 0.10	17.13
500000	13.25; 13.53; 12.8	2.08; 3.40	14.10; 15.03; 13.98	6.56;0.85	14.80; 16.02; 14.5	8.28; 2.03	11.80; 12.02; 11.69	1.91; 0.93	15.99
600000	14.70; 15.69; 15.29	6.74; 4.01	17.50; 18.49; 18.97	5.66; 8.4	19.00; 19.79; 17.9	4.16; 5.79	12.60; 13.79; 12.53	9.45; 0.55	15.11
700000	14.70; 16.06; 16	9.23; 8.84	23.50; 24.76; 22.93	5.34; 2.42	25.00; 26.06; 26.14	4.22; 4.56	12.60; N/A; 14.05	N/A; 11.56	13.27
800000	14.70; N/A; N/A	N/A; N/A	30.75; 32.32; 31.92	5.11; 3.80	31.50; 33.32; 32.16	5.78; 2.09	12.60; N/A; N/A	N/A; N/A	11.38
867111	14.70; N/A; N/A	N/A; N/A	34.20; N/A; N/A	N/A; N/A	37.50; N/A; N/A	N/A; N/A	12.60; N/A; N/A	N/A; N/A	1.33
	Mean of Error% (DIC;CV)				9.71; 4.23				
	Std of Error% (DIC;CV)				7.36; 3.98				

Table 3.11: Comparison of Crack Length of Machinist Scale, DIC method and CV method of the Fifth Hexagon Experiment (unit: mm; MS = Machinist Scale; DIC = Digital Image Correlation; CV = Computer Vision; MRF = Maximum Reaction Force)

3.8 Conclusions

By combining numerical model and observations from marine structures or laboratory experiment, digital twin approaches are promising in predicting crack length and enhancing lifecycle performance of complex marine structures. Experimental data is important to verify and support such models. In this research, in terms of reducing time consumption and test cost of large scale experiments, a laboratory scale experiment is designed and conducted reflecting many of the properties of a complex marine structure undergoing degradation. The design of specimen and the logic of the experiment is presented. Three methods are used to measure the crack length including machinist scale, CV method and DIC method. As part of this work the new CV method was followed by the validation using standard eccentrically-loaded single edge crack tension specimen. Strain gauges are applied to monitor the structure helping understand the structural status better. Five sets of hexagon specimen have been tested and the test results are presented and documented in this chapter. The results indicate that the cracks interact with each other undergoing degradation resulting in the interesting shadowing effect. The maximum reaction force decreases smoothly as applied cycles increase and drops to a small maximum reaction force when one crack breaks indicating the specimen still has the capability to take loads. The result demonstrates that the designed specimen successfully mimics the properties of complex structures including crack interaction and structural redundancy. The results can not only be used to evaluate the performance of the numerical model developed in the following chapter but also support the exploration of digital twin models.

CHAPTER IV

A Numerical Model Predicting the Crack Growth of Complex Structural System: Development, Tuning and Evaluation

4.1 Introduction

Suffering from fluctuating load cycles, the structural safety and reliability of marine structures are jeopardized by fatigue damage. If the crack length can be predicted and the inspection or maintenance strategies are optimized accordingly, the safety and reliability of marine structures can be increased. Digital twin models have been proposed for such purposes. Digital twin contains a numerical model describing the real-world structural system. With the data fusion process combining observations from the structural system into the numerical model, the numerical model will have enhanced prediction performance. Such digital twin methods can improve lifecycle performance and forecast risks, and importantly many digital twins now attempt to model structural system rather than individual failures, such as fatigue cracks. In the following section, a DBN is explored to model the crack propagation from a single crack to multi-crack with interactions. The task is divided into several steps: first, a DBN is constructed to model one crack propagation with simulated input in Section 4.3. Based on Section 4.3, Section 4.4 introduces hyperparameters for modeling the interactions between two cracks with simulated input. Then, a DBN with hyperparameters describing the interaction among four cracks is developed for the hexagon specimen in Section 4.5. Finally, Section 4.6 introduced the connections between crack lengths and SIF to model the interactions among cracks better. In summary, Section 4.3 and Section 4.4 explored DBN from one crack to two cracks with simulated evidence. Section 4.5 and Section 4.6 expand the DBN to four cracks with experiment data as evidence and focus on how to improve the modeling of crack interactions in terms of increasing prediction accuracy. The performance of the developed numerical model is evaluated by the independent data of hexagon experiment and the result is concluded in Section 4.7.

4.2 Literature Review

Due to the uncertainties in the as-built condition of marine structures from sources such as shipyard-to-shipyard differences, material qualities discrepancy, and manufacture inconsistency, it is challenging to build numerical models for the fatigue damage in complex structural system. Owing to the stochastic nature of fatigue damage, probabilistic approaches have been widely proposed for modeling fatigue damage. *Souza and Ayyub* (2000) developed a methodology to analyze ship structure fatigue based on probabilistic linear elastic fracture mechanics considering the effects of the residual stresses introduced in the fabrication process. *Doshi and Vhanmane* (2013) proposed a method to assess the fatigue life of the connection of a longitudinal stiffener to a transverse web frame with fracture mechanics. In this work, the crack growth law parameters and the applied loads were treated as random variables. Probabilistic fatigue analysis usually requires simulate numerous cases. *Monsalve-Giraldo et al.* (2016) applied univariate dimension-reduction method to increase the simulation efficiency in terms of making the method more applicable. *Khan and Ahmad* (2010) applied the uncertainty modeling to evaluate the fatigue safety of oil and gas risers under random loads. Finite element model built in ABAQUS/Aqua was used to acquire the dynamic behavior of riser. Moreover, probabilistic modeling has also been explored for steel structures in civil engineering area. *Kwon et al.* (2011) integrated a bilinear S-N approach into a probabilistic model to describe the uncertainties associated with the fatigue deterioration process, which is applied to critical details of bridges for case study. *Lu et al.* (2016) presented a probabilistic modeling approach with deterministic finite-element-based hot-spot analysis. In order to reduce the computational complexity in finite element model, machine learning technologies including uniform design and support vector regression is introduced. Extended efforts have been conducted on this area, however, these studies mainly focused on analyzing the fatigue performance on individual components. The interactions among components are also an important factor for modeling fatigue damage more accurately. These system studies are currently lacking in the literature.

To overcome the difficulties in probabilistic method and work with uncertainties, BN have been explored to model the degradation process of complex structural system considering interactions among components. BN are suitable for system-level modeling giving their ability to model complex conditional dependence and propagate evidence throughout the entire network. *Bhandari et al.* (2017) models pitting degradation of ocean structures with a BN predicting the long-term pitting corrosion depth of steel structures in marine environment. *Abaei et al.* (2018) applied a BN on assessing reliability of marine floating structures and predicting an optimum design point of the mooring system. DBN have been developed to extend the BN to problems involving time sequences. DBN are efficient and robust in updating and predicting, making it suitable for the crack length prediction of deterioration processes. *Straub* (2009) proposed a framework for modeling deterioration processes using DBN. The study indicated that the DBNs is ideally suitable for near-real time application in deterioration process due to its efficiency, robustness and updating capability. *Rabiei* *et al.* (2016) applied DBN on estimating damage and predicting crack initiation in a metallic alloy under fatigue. In this study, DBN is employed to model all random variables along with their dependence. *Zhu et al.* (2019) assessed the fatigue damage of orthotropic steel deck based DBN. The framework was able to perform diagnosis and prognosis through integrating the model with inspections. In order to handle the dependence at different system components during deterioration, *Luque and Straub* (2016) introduced the hierarchical structure to DBN for system-level analysis. Numerous approaches have been developed based on BN, however, the majority of them have not been evaluated by independent experiment data. In this work, a new hierarchical network is built based on DBN and evaluated by independent data from real-world experiments. The following sections explore the construction of the developed network in several steps from modeling a single crack to modeling a multi-crack structure including component dependence whose performance is evaluated by independent experiment data.

4.3 Dynamic Bayesian Network for Single Crack with Simulated Input

In this section, the growth of a single crack is modeled by DBN based on Paris' law. The DBN model is constructed by the commercial software - *HUGIN Andersen et al.* (1989) and *Jensen et al.* (2005). The simulated evidence is input at each timestep to predict the crack growth.

4.3.1 Fatigue Crack Growth Model

The deterministic core of the fatigue model used here is the Paris' law describing crack growth as follows,

$$\frac{da}{dn} = C[\Delta SF\sqrt{\pi a}]^m \tag{4.1}$$

where a is crack length; n is number of applied cycles; $\frac{da}{dn}$ describes the crack growth rate; ΔS is the stress range with constant amplitude which is assumed to be homogeneous and uniaxial; C and m are experimentally determined material constants; F is a dimensionless parameter depends on the geometry which is set as 1 in this case for convenience with the assumption that the crack is located on a plate with infinite size. All the proceeding variables can be modeled scholastically to give a stochastic crack growth prediction. $\Delta SF\sqrt{\pi a(n)}$ is defined as the stress intensity factor (SIF) in linear elastic theory interpreting the stress intensity near the tip of a crack or notch caused by a remote load or residual stresses, *Anderson* (2005).

Equation 4.1 is a differential equation where crack length a and number of cycles n can be separated given F is equal to 1. Solving the Equation 4.1 for crack length a with respect to the number of cycle n, results in Equation 4.2, *Ditlevsen and Madsen* (1996)

$$a = [(1 - \frac{m}{2})C\Delta S^m \pi^{m/2} n + a_0^{(1-m/2)}]^{1/(1-m/2)} \tag{4.2}$$

If the model is built based on Equation 4.2 directly, the states of modeling $(1 - \frac{m}{2})C\Delta S^m \pi^{m/2} n$ is the multiplication of the states of C, m and ΔS, which is computationally expensive and could lead to an explosion of the associated state space. In order to avoid state space explosion and reduce computation cost, $q = (1 - \frac{m}{2})C\Delta S^m \pi^{m/2} n$ is introduced to reduce the dimension of the problem *Straub* (2009). The corresponding equation 4.2 is shown as follows,

$$a = [q + a_0^{(1-m/2)}]^{1/(1-m/2)} \tag{4.3}$$

By replacing the number of cycles as the cycles between time step t and $t-1$, equation 4.2 can be rewritten in the following format, equation 4.4,

$$a_t = [q + a_{t-1}^{(1-m/2)}]^{1/(1-m/2)} \tag{4.4}$$

where a_t and a_{t-1} represent the crack length of current and previous time step respectively; q and m are the parameter for the current time step. Note that the equation is valid when $m \neq 2$, which otherwise may lead to extreme values of a_t.

4.3.2 Network Construction

Based on equation 4.4, the network is constructed as illustrated in Figure 4.1, following the example of *Straub* (2009). The time steps are shown as subscripts of the nodes from 0 to T. In the first time step, q is constructed as a child of parent nodes C, m and ΔS. In each time step, the dependencies between nodes are modeled by arrows, e.g. a_1 depends on a_0, q_1 and m_1. The nodes without parents are described by prior probability such as nodes C, ΔS and a_0 while the nodes with parents have conditional probability tables such as q and a_1. The progression of crack is described by the arrows between two time steps, e.g. q_1 to q_2, m_1 to m_2 and a_1 to a_2. The progression is quantified by transition matrices. The evidence can be input from the node of crack length $(a_i, i = 0, 1, ...T)$ of each time step.

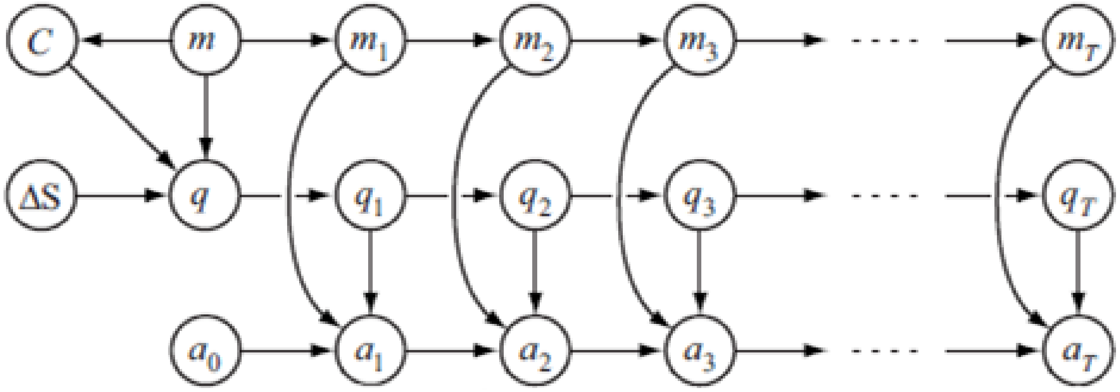

Figure 4.1: Diagram of DBN for the Growth of a Single Crack (adapted from *Straub* (2009))

The software, *Hugin*, is used to build the DBN model and perform inference with evidence. The *Hugin* software is a system contains tools for construction, maintenance, and deployment of BN, which is designed to be used easily for anyone wishing to construct an expert system based on BN, *Madsen et al.* (2005) and *Jensen et al.* (2005). It provides a GUI for users to construct a network, input evidence, and perform inference. The model shown in Figure 4.1 is constructed in *Hugin* with the concept of OON. The OON contain instance nodes representing subnets. It is suitable for building a DBN which usually has repetitive patterns. An instance connects to other nodes through interface nodes including input nodes and output nodes. The input nodes are placeholders rather than real nodes that pass the info from previous instance to the current instance. The output nodes are real nodes of an instance which can be bounded to an input node of another instance. For example, in Figure 4.2 the "first slice" and "other slices" are two subnets of the entire network where the "first slice" is unique and the "other slices" is a repetitive pattern. Thus, the instances are built separately in *Hugin* software and connected together to represent the entire DBN model. Instances connect with each other by interface nodes responsible for transferring information, i.e. the input and output nodes. In Figure 4.2, the dashed gray nodes of "other slice" are input node and the gray nodes are output nodes. The first slice contains input and output nodes as well but the input nodes are not connected with previous output nodes. The model contains four slices and since the first slices have two nodes for inputting observations, five nodes are available for inputting five evidence in total.

4.3.3 Variable Discretization and Network Quantification

After constructing the structure of model, the next step is quantifying the network. The first step is determining the range of variables. The range is defined in the way that the probability of this variable being outside the range is smaller than a specific threshold, which is usually set as 10^{-6} in practical. Note that in Chapter II the inference method focuses on discrete variables while this chapter deals with continuous variable, hence the variables are discretized. Inference of continuous variables exists

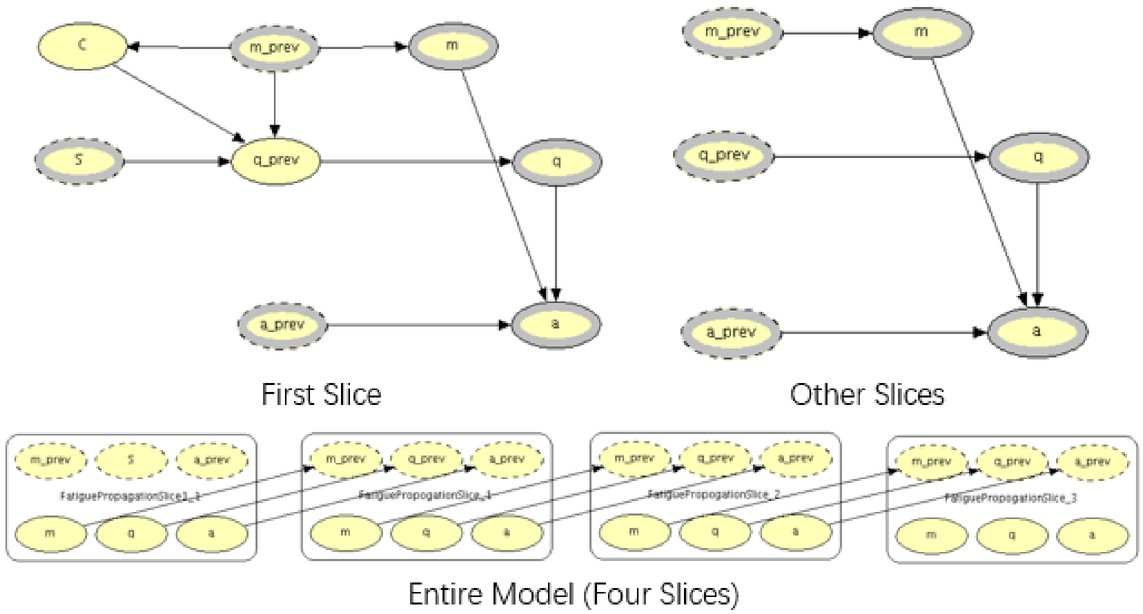

Figure 4.2: Implement DBN of Crack Growth in Hugin

but is usually inferenced by sampling-based methods where the cost of calculation increases dramatically with increasing the number of nodes and the convergence is usually hard to achieve, *Li and Mahadevan* (2018). Thus, the next step is discretizing the range in terms of using exact inference more efficiently, *Luque and Straub* (2016) and *Schneider et al.* (2017). The most straightforward discretization is dividing the range into equal-length intervals. However, this approach may not describe the variables suitably. Thus, the variable x is usually projected onto a higher space $T(x)$ and the equal-length discretization is applied on the higher space. The discretized continuous variables will have a series of consecutive and mutually exclusive states. Table 4.1 shows the range and discretization of variables for the model in Figure 4.2. The final quantifying step is determining the probability tables including prior probability tables and conditional probability tables, with respect to the state of a variable. The prior probabilities tables quantify the prior probabilities of nodes without parents like node C while the conditional probability tables describe the conditional probabilities conditioned on the states of parent nodes for child nodes like q. Table 4.2 shows the distribution and parameters of nodes having prior probabilities. The conditional

Variable	**Range**	**Number of States**	**Intervals**
$a_t(mm)$	0.01-50	80	0, exp{ln(0.01):[ln(50)-ln(0.01)]/78:ln(50)},∞
m	2-5	30	0, ln{exp(2):[exp(5)-exp(2)]/28:exp(5)},∞
q	-1--10^{-3}	35	$-\infty$, -exp[0:ln(10^{-3}/33:ln(10^{-3})], ∞
ΔS	10-110	52	0, 10:2:110:, ∞
ln(C)	(-35.3)-(-30.7)	48	$-\infty$, -35.3:0.1:-30.7, ∞

Table 4.1: Range and Discretization of Variables

Variable	**Distribution**	**Mean**	**Standard deviation**	**Correlation**
$a_0(mm)$	Exponential	1	1	-
ΔS	Normal	60	10	-
ln(C), m	Bi-Normal	(-33; 3.5)	(0.47;0.3)	$\rho_{ln(C),m} = -0.9$

Table 4.2: Distribution and Parameters of Variables

probabilities is acquired through Monte Carlo simulation combining the states of the parents nodes. Take $q(C, \Delta S, m)$ for an example, for each combination of the states of C, ΔS and m, 1000 sample is generated according to $q = (1 - \frac{m}{2})C\Delta S^m \pi^{m/2} n$, where n is 10^6 cycles. Then the simulated q is distributed into the state of q to form the conditional probability table.

4.3.4 Single Crack Results and Conclusions

To test the updating ability of the proposed DBN model, five crack lengths are generated as simulated observations from sampling Equation 4.3. The parameters used for generating observation are summarized in Table 4.3. The generated five crack lengths are input into the a_{prev} and a nodes of the first slice and a nodes of the rest three slices as evidence to update the marginal probability of nodes C, S and m. The updated C, S and m are described by the expectation calculated by multiplying the marginal probability with the states of the variable. Figure 4.3 shows the expectations of C, S and m with two and five pieces of evidence used for update. The red dash line indicates the parameters adopted for data generation which is the true value that the predictions are supposed to approach. In other words, with more evidence input into the model, the expectations or predictions of parameters

$a_0(mm)$	$S(MPa)$	**C**	**m**	**n**
1.1	75	$exp(-33)$	3.3	10^6

Table 4.3: Parameters for Generating Simulated Crack Growth

are expected to move towards the red dash line. Figure 4.3a-4.3c demonstrate the predicted parameters with three and five evidence input. The results indicate that the prediction of parameters moves towards the red dash line, i.e. the true value, with more evidence input. The predicted S with five pieces of evidence is slightly higher than the parameter used in data generation which indicates the DBN model believes the observed crack length should correspond to a higher stress. The prediction of m is changing slightly compared with C and S but it should be noted that the predicted m is already very close to the number used in data generation. The results demonstrate the power of updating and predicting of DBN and lay the foundation for modeling multi-crack deterioration in Section 4.4.

4.4 Dynamic Bayesian Network for Multi-crack with Simulated Input

4.4.1 Introduction

Section 4.3 demonstrated the capability of DBN in modeling the deterioration process of a single crack. However, marine structures usually suffer from multi-cracks in critical location and the cracks in complex structural system are typically correlated. Thus, considering the structure at the system level instead of the level of individual components is critical. In the following section, the dependence between cracks is modeled and the deterioration of a single crack is integrated into a system level prediction.

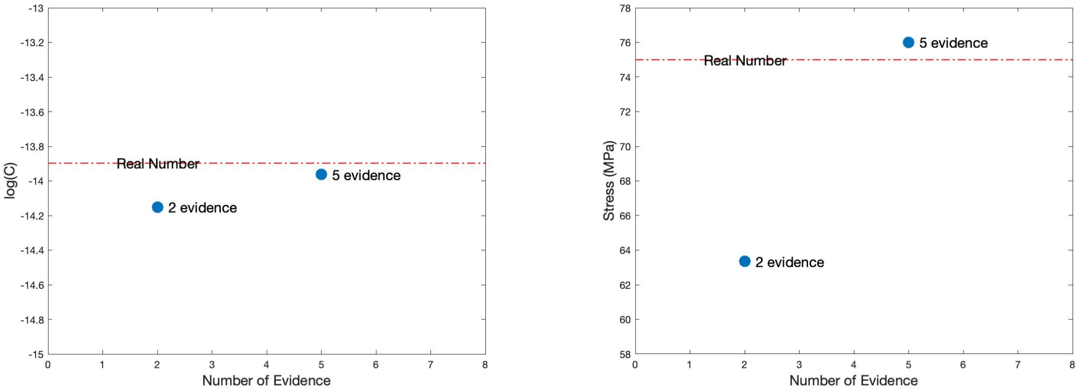

(a) Updating of $Log(C)$

(b) Updating of S

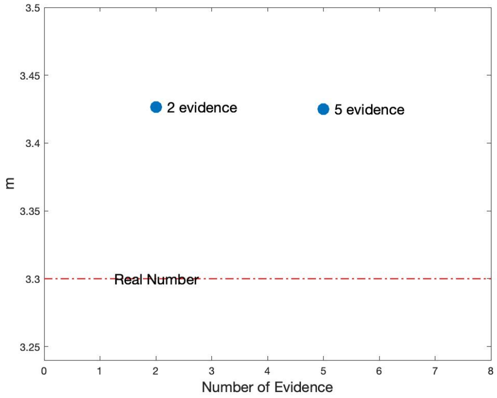

(c) Updating of M

Figure 4.3: Parameter Updating with Evidence Input

4.4.2 Dependency and Hierarchy Model

Modeling dependence for components at the system level is difficult in terms of representing the correlation mathematically. Several previous studies can be found which investigated the component dependence. These studies commonly used two typical models - random field models and hierarchical models - two common methods for modeling dependence, *Maes et al.* (2008) and *Vrouwenvelder* (2004). Random field models focus on modeling the dependence among different geometric locations *Maes* (2003) and *Stewart and Mullard* (2007), while hierarchical model uses common influencing factors describing the components dependence *Maes et al.* (2008) and *Maes and Dann* (2007), which is suitable for this case since cracks are correlated with common features instead of geometric properties. Figure 4.4 shows a hierarchical BN with a common influencing factor α at the highest level of the hierarchy, which is usually referred to as the hyperparameters level. The hyperparameter has several children nodes $(V_1, V_2, ..., V_n)$ which are correlated through the hyperparameter. As long as the hyperparameter is uncertain, the children variables are dependent on each other.

In order to calculate the CPT of variables V_i, Nataf transformation *Liu and Der Kiureghian* (1986) is applied making the assumption that the children nodes of the hyperparameter node are jointly normal. Nataf transformation projects the random variable V_i onto the space of standard normal distribution shown as $Y_1, Y_2, ..., Y_n$ in Figure 4.4 circled by the dash box. Y_i are standard normal variables connecting random variables V_i and the hyperparameter α by Equation 4.5, where F_{V_i} is the CDF of V_i and ϕ is the inverse of standard normal CDF. The correlation ρ_V between V_i can be reflected by the correlation ρ_Y between Y_i. In other words, after performing the transformation described in Equation 4.5, the resulting random variables $Y_1, Y_2, ..., Y_n$ have correlation ρ_Y. ρ_Y is a function of ρ_V and F_V which can be approximated according to *Liu and Der Kiureghian* (1986). The dependence of Y_i is modeled by the standard normal hyperparameter α as shown in Figure 4.4. Then Y_i are normal random variable conditional on α with mean $\sqrt{\rho_Y}\alpha$ and standard deviation $\sqrt{1-\rho_Y}$. The unconditional Y_i are standard normal random variables with mutual correlation ρ_Y. The nodes Y_i working as transformation nodes can be eliminated and the resulting BN with direct connection from α to V_i is shown in the right plot of Figure 4.4. The CPT of V_i can be acquired by Equation 4.6.

$$Y_i = \phi^{-1}[F_{V_i}(V_i)], i = 1, 2...n \tag{4.5}$$

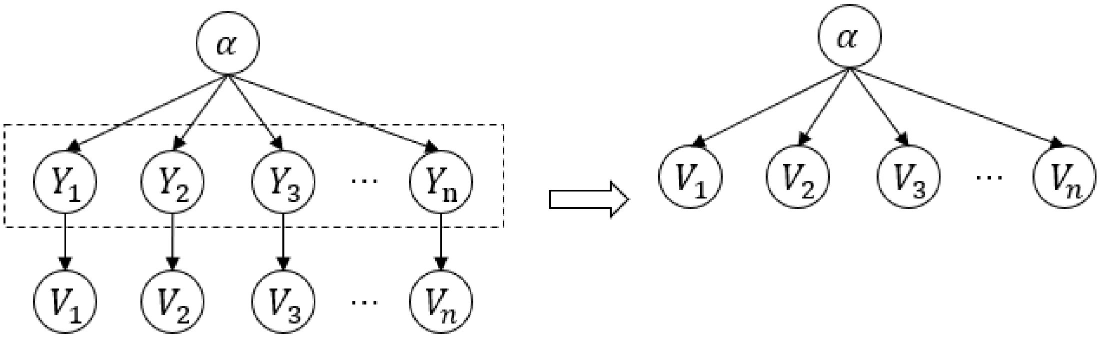

Figure 4.4: Hierarchy Model of Bayesian Network, *Luque and Straub* (2016)

$$F_{V|\alpha}(v) = \phi[\frac{\phi^{-1}(F_V(v)) - \sqrt{\rho_Y}\alpha}{\sqrt{1-\rho_Y}}] \tag{4.6}$$

4.4.3 Network Construction, Variable Discretization, and Network Quantification

The DBN network is built in *Hugin* based on the single-crack model described in Section 4.3.2, combined with the hyperparameter concept. Figure 4.5 demonstrated the DBN model for two interactive cracks constructed in *Hugin.* Similar to the single-crack model, the first slice is unique while the other slices have a repetitive pattern. In the model, the stress of two single-crack model are connected by a hyperparameter in the first slice representing the interactions of the cracks in the degradation process.

The first slice is connected to its successors by connecting the output nodes, shown as gray nodes, with the input nodes of the other slices, shown as dashed gray nodes. The entire model has five slices modeling the deterioration process.

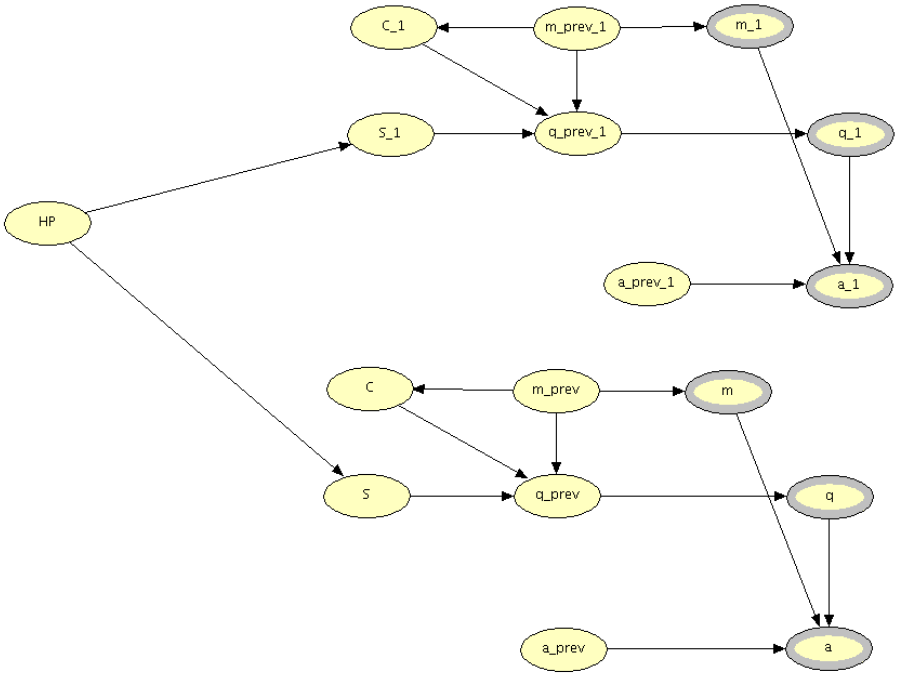

(a) First Slice

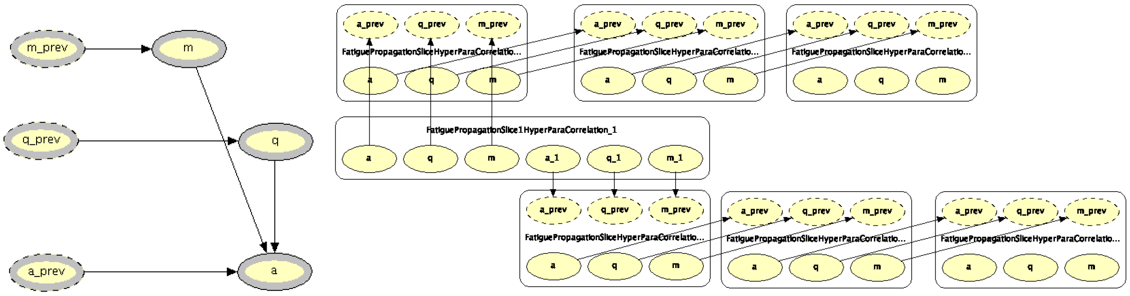

(b) Other Slices (c) Entire Network

Figure 4.5: Modeling Two Cracks in Hugin

The random variables used this model have the same range, discretization, and distribution with those in Section 4.3, as shown in Table 4.4 and Table 4.5. The distribution and parameters for hyperparameter of stress are summarized in Table 4.9. The correlation of components stress is $\rho_S = 0.5$. The prior probabilities tables are quantified according to the specified distributions like node C and node hyperpa-

Variable	Range	Number of States	Intervals
$a_t(mm)$	0.01-50	80	0, exp{ln(0.01):[ln(50)-ln(0.01)]/78:ln(50)},∞
m	2-5	30	0, ln{exp(2):[exp(5)-exp(2)]/28:exp(5)},∞
q	-1--10^{-3}	35	$-\infty$, -exp[0:ln(10^{-3}/33:ln(10^{-3})], ∞
ΔS	10-110	52	0, 10:2:110:, ∞
ln(C)	(-35.3)-(-30.7)	48	$-\infty$, -35.3:0.1:-30.7, ∞

Table 4.4: Range and Discretization of Variables

Variable	Distribution	Mean	Standard deviation	Correlation
$a_0(mm)$	Exponential	1	1	-
ln(C), m	Bi-Normal	(-33; 3.5)	(0.47;0.3)	$\rho_{ln(C),m} = -0.9$

Table 4.5: Distribution and Parameters of Variables

rameter node HP, which is node α in Figure 4.4. The conditional probability tables for node S_1 and S are acquired by Equation 4.6. The rest conditional probability tables are simulated through Monte Carlo method combining the states of parents nodes. For each combination of the parents states, 1000 samples are generated and distributed into the states to form the conditional probability table.

4.4.4 Results and Conclusions

The performance of the network with hyperparameter is evaluated by the crack length generated in Section 4.3. The simulated crack length is the observation of one crack while another crack is assumed to have no growth in the deterioration process. Five observations are input into the growing and non-growing crack. Since the hyperparameter models the interaction of the stresses of two cracks, the expectation of the two stresses S and S_1 are calculated and compared by multiplying the marginal probability with the states of the variable. The expectations are calculated after inputting the third and fifth evidence respectively in terms of investigating the updating power. The result is plotted in Figure 4.6 with the red dash line indicating the

Variable	Distribution	Mean	Std	Number of States	Intervals
α_s	Normal	0	1	5	$\phi^{-1}(0 : 0.2 : 1)$

Table 4.6: Distribution and Parameters for Hyperparameter of Stress

parameters used for data generation which the predictions are supposed to approach. It should be noted that in the data generation process, the crack interaction is not considered. The expectation after three observations are annotated with red color while the expectations after five observations are marked with blue color. Comparing the expectations with real number used in observation generation, the expectation of stress moves towards the true value with more evidence observed. The stress difference between two cracks increases with the observation from three to five indicating the model can distinguish the different propagation of the two cracks. The predicted stress S for crack 1 with five observations of crack growing is slightly higher than the parameter used in data generation, while the predication for crack 2 without crack propagation is lower than the real number, which indicates the interaction between two cracks. That is to say, due to the interaction of cracks, the DBN model believes the growing crack should correspond to a higher stress while the stress of another crack is shadowed by the growing crack. The result successfully demonstrates that DBN combined with hyperparameter can distinguish and react to the interactions among components.

4.5 Dynamic Bayesian Network for Hexagon Specimen

4.5.1 Introduction

With the exploration of DBN and hyperparameters in Section 4.3 and Section 4.4, the DBN is proved to be capable of modeling the deterioration of structural system over time and make predictions about future structural capacity. Additionally, the DBN modeling single crack growth in component level was expanded to address the propagation of two cracks in a common system, which lays a solid foundation for modeling the hexagon specimen with interaction between four cracks in this section. Expanding the interactions from two cracks to four cracks is not only about increasing

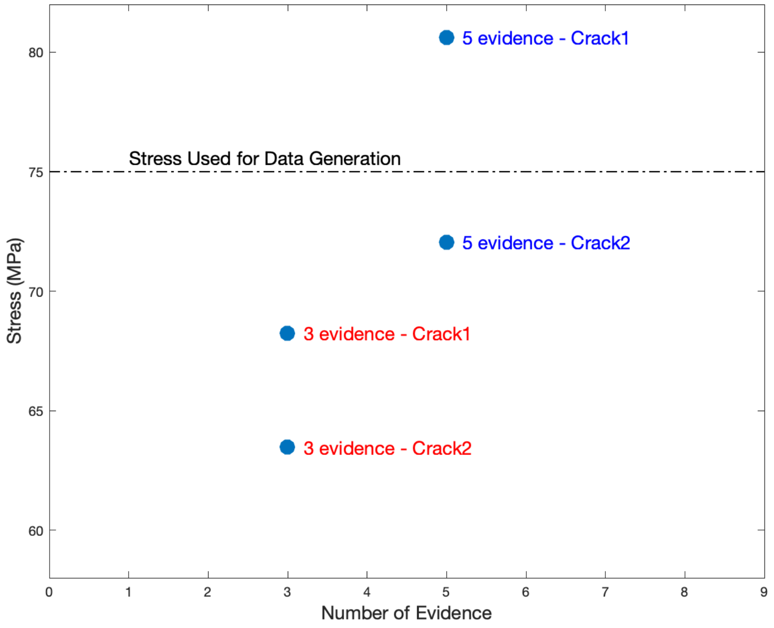

Figure 4.6: Stress Updating of Two Dependent Cracks

computational cost, the crack model as well as the quantification are also modified for this case. The goal of modeling hexagon specimen is to predict the crack length in system level considering the dependence among cracks. Section 4.5.2 describes the crack growth model used in this model. The construction and quantification of model are detailed in Section 4.5.3. The updating power and performance of the developed model are discussed in Section 4.5.4.

4.5.2 Fatigue Crack Growth Model

The deterministic fatigue model used here is the Paris law, Equation 4.7, the same as modeling the single crack propagation with simulated input in Section 4.3. The equation describes the crack growth rate as a function of SIF - $\Delta S F \sqrt{\pi a(n)}$ - with power m and coefficient C, where SIF is a function of stress ΔS, crack length a and geometry parameter F. In Section 4.3, the geometry parameter F is set as 1 by assuming the crack is on a plate with infinite size. The assumption makes Equation

4.7 integratable to a explicit solution of crack length. However, in modeling the crack growth of hexagon specimen, the crack cannot be assumed to propagate on an infinite plate. The geometry restriction has to be considered for modeling accurately. Thus, each crack on the hexagon specimen is viewed as an edge crack on a bar with finite width. The geometry factor F is estimated by a fourth order polynomial shown in Equation 4.8, where a is the crack length, b is the width of bar, *Liu et al.* (2015). Since the geometry factor is a function of crack length a, integrating the Paris' law equation explicitly is not possible. Thus, the crack growth is simulated numerically by the fourth order Runge Kutta method which estimates the integration with four approximations to the slope.

$$\frac{da}{dn} = C[\Delta S F \sqrt{\pi a}]^m \tag{4.7}$$

$$F = 1.122 - 0.231\frac{a}{b} + 10.55(\frac{a}{b})^2 - 21.71(\frac{a}{b})^3 + 30.382(\frac{a}{b})^4 \tag{4.8}$$

The concept behind the fourth order Runge Kutta method is shown in Equation 4.9 and 4.10. Equation 4.9 describes the initial value problem where y is an unknown function of t and y itself. The initial y_0 is known at t_0. With the defined step size h, which is the applied cycles between two observations, the fourth order Runge Kutta estimated the increment from y_n to y_{n+1} with a weight average of increment k_1, k_2, k_3 and k_4, described in Equation 4.10, where $n = 0, 1, 2...$ represents the steps, *Süli and Mayers* (2003). k_1 and k_4 are acquired from the slope at the beginning and ending of the interval; k_2 and k_3 are calculated using the slope at the midpoint with y_n and k_1, y_n and k_2 respectively, shown in Equation 4.11.

$$\begin{aligned} \dot{y} &= f(t, y), \\ y(t_0) &= y_0. \end{aligned} \tag{4.9}$$

$$y_{n+1} = y_n + \frac{1}{6}(k_1 + k_2 + k_3 + k4) \tag{4.10}$$

$$\begin{aligned} k_1 &= hf(t_n, y_n), \\ k_2 &= hf(t_n + \frac{h}{2}, y_n + \frac{k_1}{2}), \\ k_3 &= hf(t_n + \frac{h}{2}, y_n + \frac{k_2}{2}), \\ k_4 &= hf(t_n + h, y_n + k_3). \end{aligned} \tag{4.11}$$

4.5.3 Network Construction, Variable Discretization, and Network Quantification

In Section 4.4, the system-level deterioration process is explored by modeling the interactions of two cracks with hyperparameters, which supports the modeling of hexagon specimen is this section. The DBN network is built in *Hugin* with a similar structure as the case with two cracks. The major difference is that the first slice is expanded to four cracks with two hyperparamters HP_s and HP_m describing the interactions of stress and material property among four cracks, as shown in Figure 4.7a. The initial crack length a_0 does not appear in the model since it is involved in the calculation of CPT implicitly. With the concept OON in *Hugin*, the first slices and other slices are built as two instances with input and output nodes shown as gray nodes and dashed gray nodes respectively. By connecting the first slice to its successors through the output nodes and the input nodes, the entire model is built with nine slices modeling the nine observations in the deterioration process of the fifth hexagon specimen, Figure 4.7c. In this application, the approach is justified owing to the precision in the initial crack size via the EDM fabrication approach. The model is a rough approximation of the crack growth process, as full dependence between the cracks is not included, nor is the impact of crack size on resulting stress.

To model the hexagon specimen, the random variables should be adjusted with respect to the hexagon application in terms of range, discretization, and distribution, as shown in Table 4.4 and Table 4.5. The range is defined so that the probability of a variable being outside the range is smaller than a specific threshold. In this work, the threshold is set as 10^{-6}. The discretization is applied on each continuous variables over its range in favor of performing exact inference method. The discretized continuous variables have a series consecutive and mutually exclusive states. Since the crack propagation is slow initially and increases dramatically with continuing application of loading cycles, the discretization of crack length a_t is refined for crack length less than 3 mm and increased from 4 mm to 100 mm to capture crack growth. Material parameter m is uniformly discretized in exponential space and then transferred back to its original space. Similarly, material parameter C is uniformly discretized in log space. Stress ΔS is discretized evenly in its original stress space. Compared to the random variables in Section 4.4, the range of random variables for hexagon specimen is adjusted according to this specific case. The discretization strategy of variables m, ΔS, and $ln(C)$ are the same except the number of states is reduced to avoid state explosion and lower the computation cost. The discretization of crack length a_t is refined for small crack length since the rate of crack growth increases as crack propagates. In this way, the discretization is able to capture the crack propagation well with a manageable size of CPT. The distribution and parameters for hyperparameter of stress ΔS and material property m are the same to the model in Section 4.4, summarized in Table 4.9.

After defining the range, discretization, and distribution of random variables, the

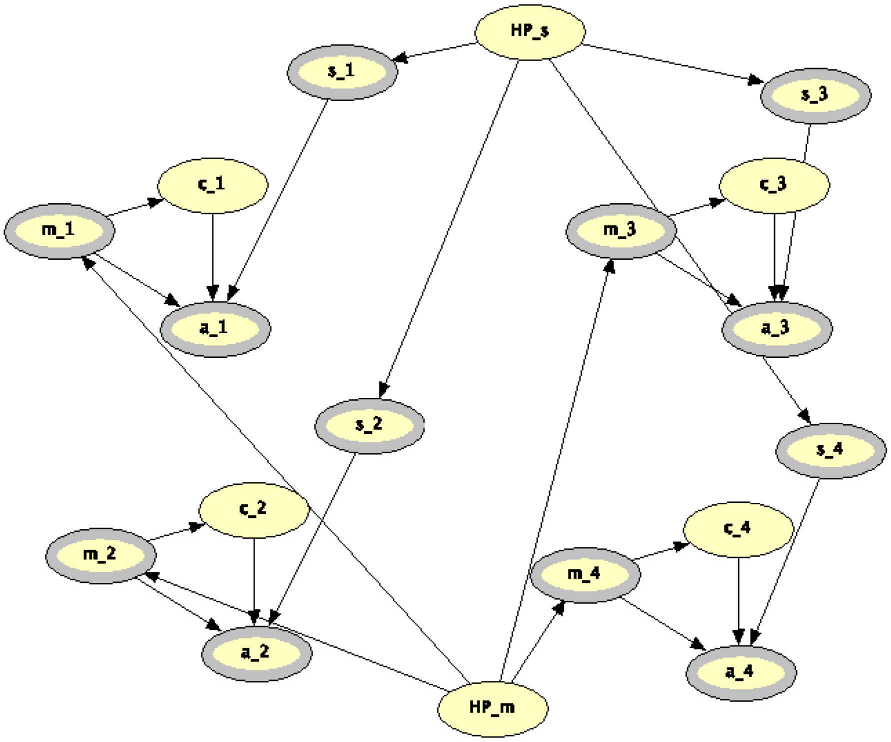

(a) First Slice

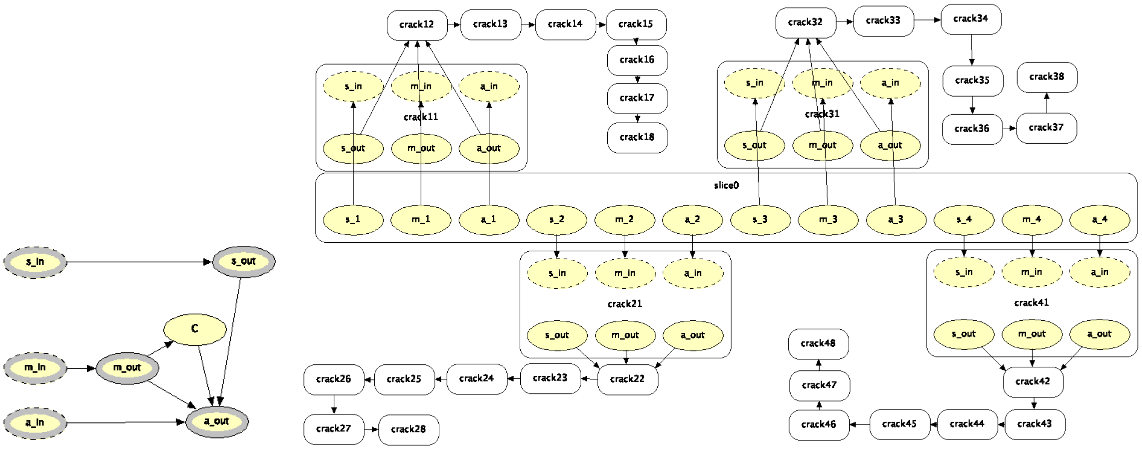

(b) Other Slices (c) Entire Network

Figure 4.7: Modeling Hexagon Specimen in Hugin

Variable	**Range**	**Number of States**	**Intervals**
$a_t(mm)$	0.0001-100	31	0, exp(log(0.0001):(log(3)-log(0.0001))/5:log(3)), 4:1:18, 21:3:36, 39:30:100, ∞
m	2.4-3.6	20	0, ln{exp(2.4):[exp(3.6)-exp(2.4)]/18:exp(3.6)}, ∞
ΔS	5-84	21	0, 5:4:84, ∞
ln(C)	(-21.3)-(-19.5)	22	$-\infty$, -21.3:(21.3-19.5)/20:-19.5, ∞

Table 4.7: Range and Discretization of Variables

Variable	**Distribution**	**Mean**	**Standard Deviation**	**Correlation**
ln(C), m	Bi-Normal	(-20.4; 3)	(0.3;0.2)	$\rho_{ln(C),m} = -0.9$

Table 4.8: Distribution and Parameters of Variables

next step is calculating the probability table. The prior probability table is calculated by assessing the probability in the defined intervals. The conditional probability table of crack length a_n given a_{n-1}, Δs, c and m is simulated by Monte Carlo method combining the states of parents nodes. In each combination, 1000 sample is generated and the crack growth is numerically simulated through the fourth order Runge Kutta. The crack size is then scattered into the node's states to construct the conditional probability table. Since the combination of states of a_{n-1}, Δs, c and m increase dramatically with increased number of discretizations, the number of states is decreased to avoid potential state explosion problem.

4.5.4 Results and Conclusions

For evaluation purpose, the crack length from the fifth hexagon experiment measured by machinist scale are input into the DBN model as observations, Table 4.10. The distribution of random variables is updated after inputting an observation of crack length which is extracted from *Hugin* as CSV files for further analysis. Since the prediction is available after inputting the first observation and the prediction af-

Variable	Distribution	Mean	Std	Number of States	Intervals
HP_s	Normal	0	1	5	$\phi^{-1}(0:0.2:1)$
HP_m	Normal	0	1	5	$\phi^{-1}(0:0.2:1)$

Table 4.9: Distribution and Parameters of Hyperparameters

ter last observation has no comparison, 8 data points are available for comparing the prediction with recorded experimental results.

Each probability from *Hugin* describes the chance falling into a specific state of crack length, thus, the predicted crack length is the expectation calculated by multiplying the center of each state with the corresponding probability. Note that the the crack length a_t has states beyond 39 mm for refining the CPT, i.e. [39, 69], [69, 99], which is treated as 39 mm in calculating expectation since the crack is broken after 39 mm and the center points of those states has no physical meaning in this case. The comparison between predicted and recorded crack length is plotted in Figure 4.8. The pink diamond represents the predicted crack length from the network while the blue square shows the recorded data from experiment. The 50% range is plotted indicating the variability of distribution from the network. Note that if the probability of being in one state is greater than 50%, no range is associated with that expectation. The four sub-plots have the same range of Y axis for demonstrating the shadowing effect clearly. As shown in the plot, even though the prediction tends to be larger than recorded data, by providing more observations, the prediction still follows the overall trend well. The variability of distribution stays low until the left bottom and right top crack become dominant from 600000 cycles when some large variability appears reflecting the adjustment of network from this observation. Then the model is confident with its prediction with more than 50% probability in one state. The biggest challenge for this model is predicting the shadowing effect, i.e. which crack is dominant. According to the experiment record, left bottom and right top cracks become dominant starting from 500000 to 600000 cycles, corresponding to the prediction after inputting 5 evidence. The model seems unable to forecast the dominant cracks resulting in the jump of left top and right bottom crack from 500000 to 600000 cycles. The jump shows that the model is adapting to the disagreement between prediction and observation. The predicted length of the dominant cracks, left bottom and right top, also has jumps due to the relatively large prediction compared to the observations. After adjusting to the observations, the prediction moves closer to the records from 6 to 8 evidence for left top, left bottom, and right bottom cracks, 7 to 8 evidence for right top crack.

Cycles	*Left Top (MS)*	*Left Bottom(MS)*	*Right Top(MS)*	*Right Bottom(MS)*
100000	2.00	2.30	2.65	2.40
200000	5.50	5.50	5.65	4.50
300000	8.25	8.00	8.50	7.50
400000	11.40	11.00	11.75	9.80
500000	13.25	14.10	14.80	11.80
600000	14.70	17.50	19.00	12.60
700000	14.70	23.50	25.00	12.60
800000	14.70	30.75	31.50	12.60
867111	14.70	34.20	37.50	12.60

Table 4.10: Validation Data Collected from the Fifth Hexagon Experiment (unit: *mm*; MS = Machinist Scale)

The updating of nominal stress node is investigated through the extracted CSV file from *Hugin*. The data is probabilities associated to the states of stress which is fitted with quadratic line and plotted in Figure 4.9. The X axis shows the range of nominal stress while the Y axis indicating the probability. The distribution of stress is updated after inputting each observation of crack length. For a clear illustration of updating process, the distribution of stress after inputting the evidence of 100000, 300000, 500000, and 700000 cycles are plotted. 100000, 300000 cycles is included to demonstrate the distribution before left bottom and right top crack become dominant, while 500000 and 700000 cycles shows the change of stress after the shadowing effect appears. As demonstrated in the plot, the four cracks have a similar stress distribution before 500000 cycles since the growth of four cracks is the same. Starting from 500000 cycles, left bottom and right top cracks take dominant slowing the propagation of left and right bottom crack while increasing the growth rate of left bottom and right top crack. Thus, at 700000 cycles, the left top and right bottom have a large nominal

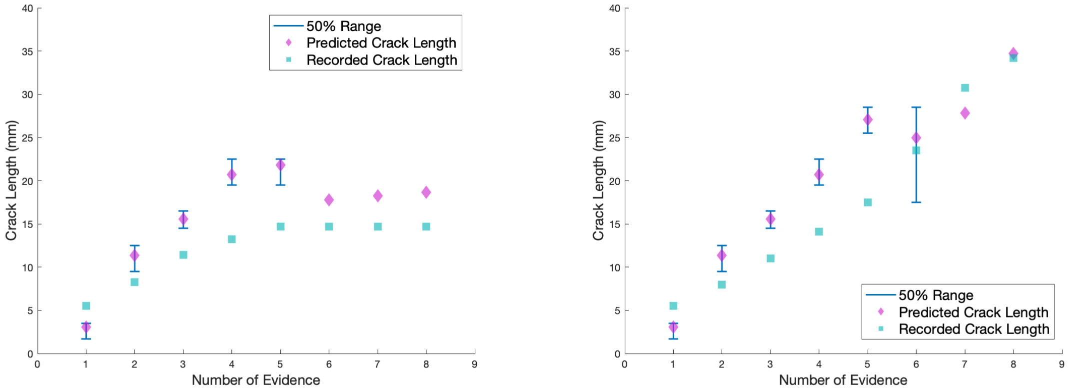

(a) Crack Length of Left Top

(b) Crack Length of Left Bottom

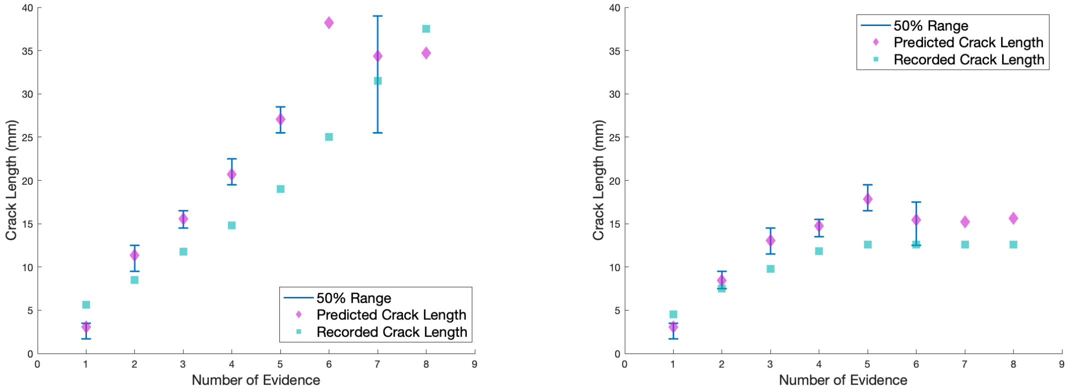

(c) Crack Length of Right Top

(d) Crack Length of Right Bottom

Figure 4.8: Predicted Crack Length from the DBN model Developed with OON

stress due to a relatively smaller crack length. The left bottom and right top crack have smaller nominal stress resulting from the larger crack. Even with the left bottom and right top cracks dominant, the nominal stress of left bottom is slightly larger than right top since right top crack grows faster than the left bottom. The updating of nominal stress demonstrates the status of the specimen providing a supplement view for the degradation process.

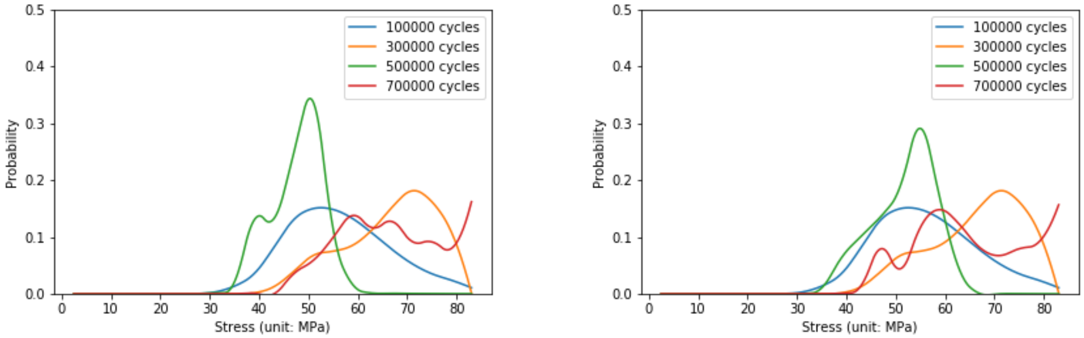

(a) Nominal Stress of Left Top (b) Nominal Stress of Left Bottom

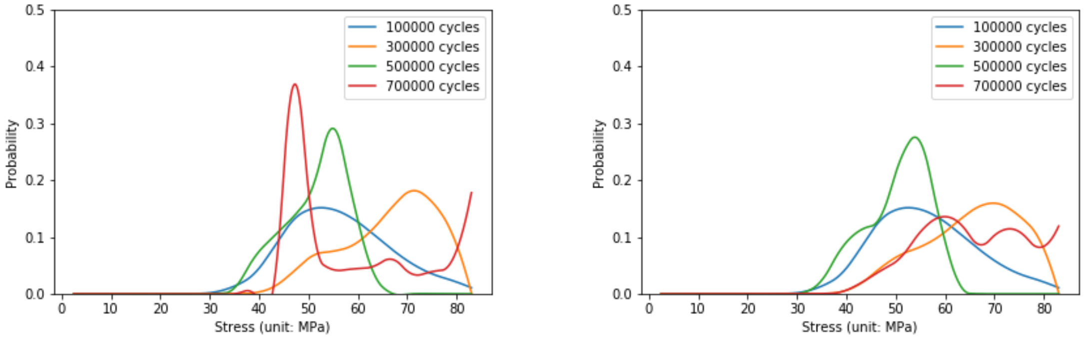

(c) Nominal Stress of Right Top (d) Nominal Stress of Right Bottom

Figure 4.9: Updating of Nominal Stress from the DBN model Developed with OON

Considering that the material property is different at different locations of a steel plate, the hyperparameter of m is included. The updating of material property m is extracted from the CSV file and plotted as quadratic lines in Figure 4.10. Since the prediction of material properties falls to the first state with 100% after 7 observations for right top and left bottom crack, 6 observations for left top and right bottom crack, the plot includes the probability distribution from 100000 to 500000 cycles. As shown in the plot, the distribution for four cracks are similar before 500000 cycles since the crack growth is the same. As inputting more evidence from 100000 to 400000 cycles, the variability of distribution decrease while the center moves from 2.75 to 2.55. Since 500000 cycles, the left bottom and right top crack are dominant resulting in a similar distribution. As both are shadowed, the left top and right bottom crack have similar updating for m at 500000 cycles. This updating of m reflects the interaction among four cracks and demonstrates the updating capability of DBN. As inputting evidence after 500000 cycles, the difference between large predictions and small observation drag the prediction of m to the first state which can be tuned in future works.

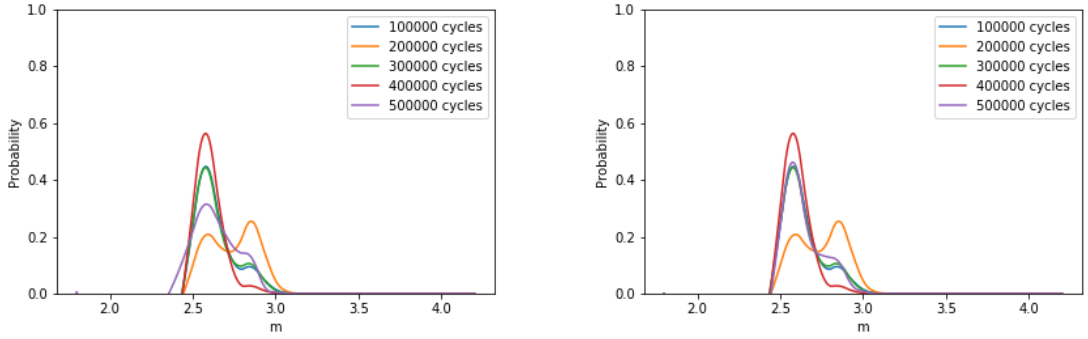

(a) m of Left Top

(b) m of Left Bottom

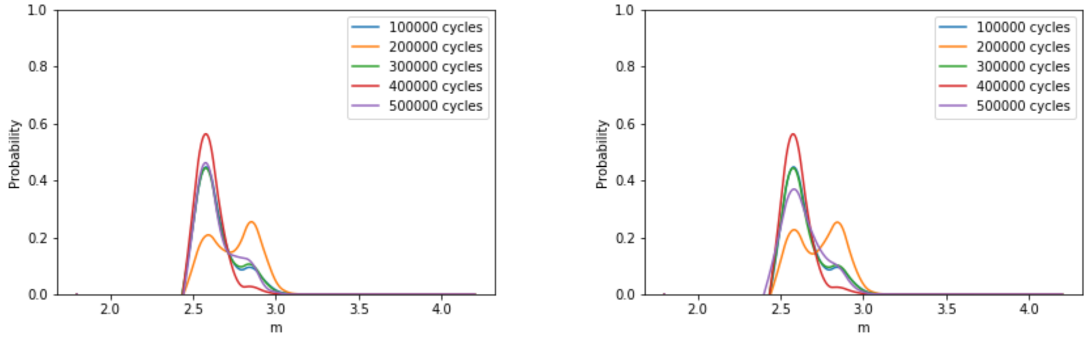

(c) m of Right Top

(d) m of Right Bottom

Figure 4.10: Updating of Material Parameter m from the DBN model Developed with OON

The performance of this model is affected by several factors. This DBN model models the propagation of four cracks separately whose dependence is described only by hyperparameters. In other words, each crack is treated as a single edge crack in modeling the propagation and then connected through hyperparameters. Since the assumption of single edge notch, the SIF is obtained based on an empirical equation in establishing the CPT which may not suit well for this case leading to a large prediction for crack length. By using hyperparameter of stress, we assume that the stress of every two cracks has the same correlation which is too simple of an idealization for this hexagon specimen. This assumption affects the performance negatively. Thus, an updated model is developed in the following section by exploring the dependence between crack lengths and SIF.

4.6 Dynamic Bayesian Network for Hexagon Specimen with Connections between Cracks and SIF

4.6.1 Introduction

The DBN model in Section 4.5 has an acceptable performance when provided with evidence in predicting crack length. The model is a rough approximation of the crack growth process without counting the impact of crack size on the resulting stress. In other words, as the crack grows, the specimen stiffness changes resulting in the SIF evolving at each crack tip over time from the other three crack lengths, rather than just its own crack length. Thus, in order to improve the model performance, the connections between each crack size and load stress are critical and explored in this section. This stress need not be tracked explicitly, it can be included in SIF for each crack which depend on the lengths of other cracks. More complex connection means more combinations of states which can result in a state explosion problem, restricting the application of the method. The technologies named Temporal Clone and Boyen-Koller approximation are applied to avoid state explosion which is explained in detail in Section 4.6.2. Another challenge is quantifying the connection between cracks and resulting SIF. An Abaqus script is written in Python to calculate the SIF with respect to various combinations of crack lengths. Then the data is used to train a Kriging model in terms of building the CPT. The details are included in Section 4.6.4 and 4.6.5. The quantification of the other probability tables are described in Section 4.6.3. Finally, Section 4.6.6 evaluates the performance of this DBN model, followed by the analysis of marginal probabilities updating. The performance of model developed in this section is also compared to the model in Section 4.5.

4.6.2 Network Construction

DBN can be constructed by building and connecting ordinary static BN representing the evolving of time, where each ordinary static BN is called a time slice, *Kjærulff* (1995). As described in Section 4.5, OON is built in *Hugin*, and can be used to model the degradation of structural systems over time. In an OON, the output and input nodes of each time slice are connected together to form the entire model. Another method used to construct DBN is named Temporal Clone based on the idea that the state of random variables in current time depends on the state of the system in the past. The state of system in the past can be represented by Temporal Clone. Figure 4.11 illustrates a simple application of Temporal Clone in modeling disease progression. The Temporal Clone is marked with right slashes named as *T_Disease* which represents the system state of node *Disease* in the past. Node *T_Disease* is cloned from its master node *Disease*. Node *Symptom* is the observed symptom, input as evidence. By connecting the Temporal Clone *T_Disease* and regular node *Disease*, the dependence between past and current states is specified. With time evolving, the Temporal Clone *T_Disease* always dynamically represents the state of system at past time while regular node *Disease* stands for current state. By defining the number of time slices, the DBN can be built based on the defined structure containing Temporal

Clones and regular nodes.

In order to use Temporal Clone correctly, it should be noted that the links between nodes should represent the natural flow of time. As discretized random variables, discretized temporal clones have tables defining the distribution of its initial state. With time evolving, the time clone are substituted by nodes in the previous time slices. The discretization of temporal clones can only be changed by modifying the nodes from which they clone. Deleting the master node also deletes the Temporal Clones of that master node.

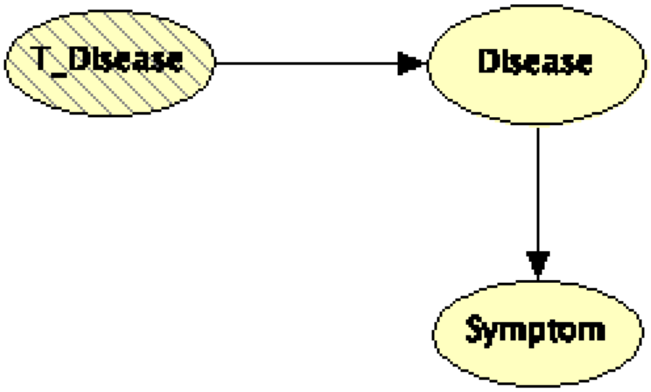

Figure 4.11: Disease Progression Model based on Temporal Clone

Based on Temporal Clone and Paris' law in Equation 4.7, the hexagon model connecting cracks with resulting SIF is built in *Hugin* as shown in Figure 4.12, where the solid nodes represent the current state of the system while the nodes marked with right slashes model the system states at the past. In this model, *m_lt*, *m_rt*, *m_lb*, *m_rb*, and *C_lt*, *C_rt*, *C_lb*, *C_rb* represents the material properties at the left top (lt) crack, right top (rt) crack, left bottom (lb) crack, and right bottom (rb) crack respectively. *K_lt*, *K_rt*, *K_lb*, and *K_rb* are the SIF of the four cracks while *a_lt*, *a_rt*, *a_lb*, and *a_rb* are the current crack length. *HP_m* is the hyperparameter of material property m describing the correlation of material property at different locations. The Temporal Clone for the hyperparameters is added into the model to represent the dependencies between past and current. The Temporal Colones for four cracks - *T_a_lt*, *T_a_rt*, *T_a_lb*, and *T_a_rb* - connect the crack length at past time to current SIF. Each SIF is linked by four temporal clones of crack lengths since SIF at each crack location is determined by all the remaining crack sizes. Compared with the model in Section 4.5 which model the interaction among stress with hyperparameter, this DBN model modeling the interaction by connecting temporal clones of crack lengths with SIF. The current crack length is a function of material properties m, C, SIF K, and previous crack length modeled by temporal clone *T_a*. Nine time slices are defined for this model with respect to the records in the fifth hexagon experiment. To summarize, the degradation of four cracks is modeled in this DBN with temporal clones and the interaction among cracks is described by the hyperparameter of m and the temporal clones of previous crack lengths linking to the current SIFs, which are different at each crack tip.

The complex connections between crack lengths and SIF make it a challenge to inference and update with evidence. Boyen-Koller approximation is applied here to improve the computational performance. Boyen and Koller, *Boyen and Koller* (1998) and *Koller and Friedman* (2009), proposed an approach to approximately calculate the joint distribution of the interface variables between two successive time slices with the goal of keeping the accumulated errors bounded indefinitely, which is suitable for the inference of model with temporal clones. The idea behind the proposed method is to make the complexity of junction tree of a single time slice tractable by factorizing the distribution. In inference, the desired factorization is applied to approximate the distribution of interface variables from which the factors are passed to the junction tree of the next time slice. *Hugin* software integrates this technique for inference and predictions with evidence. Normal propagation is performed within each time slice while approximate distribution of interface nodes is transferred from one time slice to the next by conducting approximation following the links between the temporal

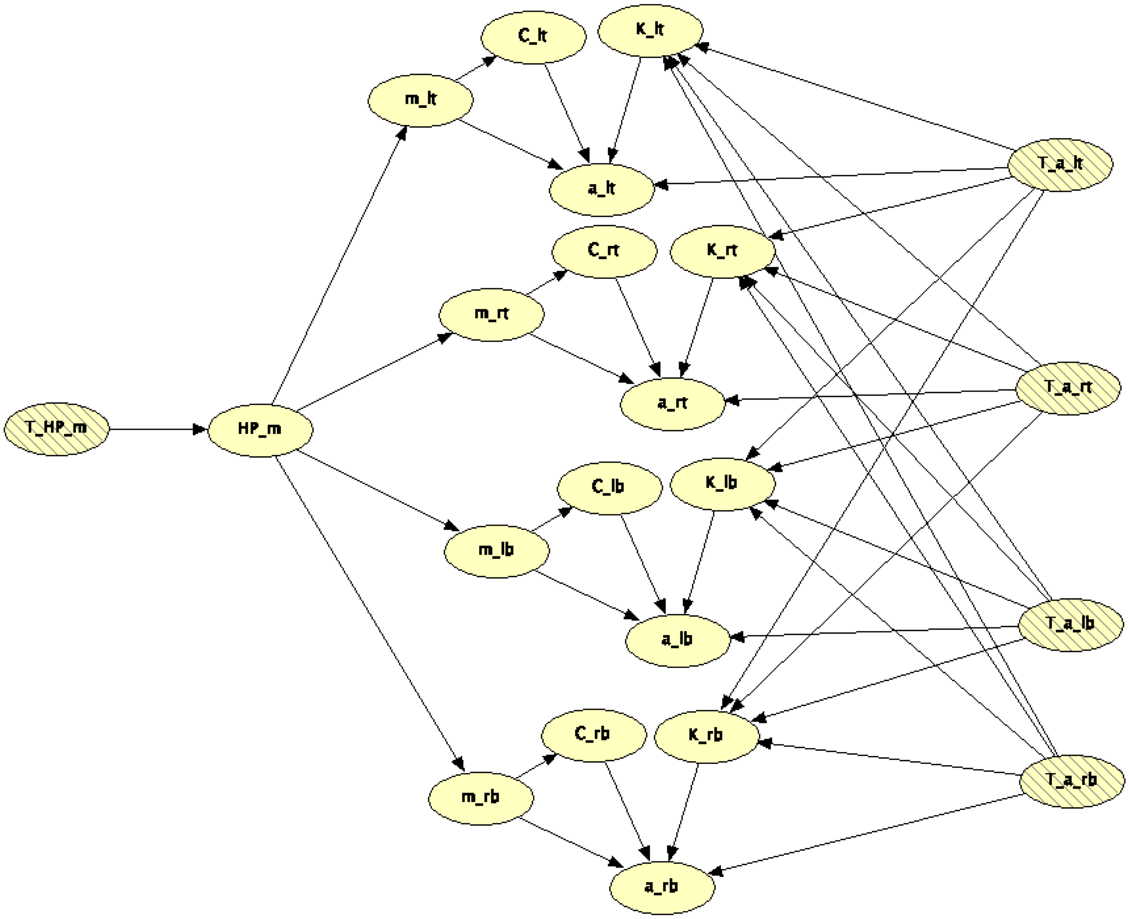

Figure 4.12: Model of Hexagon Specimen with Connections between Cracks and Resulting SIF based on Temporal Clones

clones which defines the factorization according to *Hugin Expert*.

4.6.3 Variable Discretization and Network Quantification

Regarding quantifying the model, the range, discretization, and distributions of random variables are first determined as shown in Table 4.11, which is applied to the four cracks. The range is chosen so that the probability of a variable being outside the range is smaller than a specific threshold which is set as 10^{-6} in this work. Since crack usually grow slowly in the beginning of deterioration, the refined discretization of crack length has $1mm$ increment from $0mm$ to $19mm$ while $3mm$ step from $19mm$ to $37mm$. The range and discretization of SIF is determined by the Kriging results whose detail is in Section 4.6.5. The material property m is discretized uniformly after being projected to a exponential space while C is discretized uniformly after being projected to a log-space. The discretization of temporal clones of nodes a, and *HP_m* is the same with their master nodes. Their distribution representing the initial state of system is shown in Table 4.12 from which the prior probabilities are determined. The distribution and parameters of hyperparameter *HP_m* is described in Table 4.13. The CPT of m given *HP_m* is determined by Equation 4.6. The CPT of *HP_m* given its temporal clone is a diagonal matrix. The CPT of crack length a_n given a_{n-1}, m, c and K is simulated by Monte Carlo method combining the states of parents nodes. In each combination, 1000 samples are generated and the crack growth is calculate by integrating the crack growth with the assumption that the SIF is a constant. The integrated results are scattered into the states of crack length to form the conditional probability table. The CPT of SIF given crack length at left top, right top, left bottom, and right bottom is established using Kriging model as shown in Section 4.6.5 which is employed to avoid running large number of Finite Element Analysis (FEA). The Kriging model is trained on sufficient SIFs generated by running FEA repeatedly with different combinations of crack length as input. The

Variable	**Range**	**Number of States**	**Intervals**
$a(mm)$	0-37	26	0, 0:19/19:19,22:(37-22)/5:37,∞
m	2.4-3.6	20	0, ln{exp(2.4):[exp(3.6)-exp(2.4)]/18:exp(3.6)},∞
$ln(C)$	(-21.3)-(-19.5)	22	$-\infty$, -21.3:(21.3-19.5)/20:-19.5, ∞

Table 4.11: Range and Discretization of Variables in Modeling of Hexagon Specimen

Variable	**Distribution**	**Mean**	**Standard Deviation**	**Correlation**
a	LogNormal	0	1	-
$ln(C)$, m	Bi-Normal	(-20.4; 3)	(0.3;0.2)	$\rho_{ln(C),m} = -0.9$

Table 4.12: Distribution and Parameters of Variables

details of acquiring training points from Abaqus in described in Section 4.6.4

4.6.4 Stress Intensity Factor from Abaqus

In the proposed model, it is a challenge to quantify the CPTs of resulting SIF from combinations of crack lengths. A Kriging model is trained to approximate the SIF given four crack lengths instead of running FEA simulation. A trained Kriging model or Gaussian process regression can make predictions by interpolating values. The kriging model is trained on data points of SIF generated by Abaqus with many combinations of crack lengths as input. The details of Abaqus modeling is described in this section.

Training a Kriging model requires hundreds data points as training set from FEA. In order to automate the FEA process, a Python script is written and iterative calculate the SIF of different combinations of crack length. The program flowchart is shown in Figure 4.13. For each iteration, a combination of crack lengths is input into the program. The crack length used for generating combinations is shown in 4.14. The integral circle around crack tips restricts the maximum crack growth as 27 mm

Variable	Distribution	Mean	Std	Number of States	Intervals
HP_m	Normal	0	1	5	$\phi^{-1}(0 : 0.2 : 1)$

Table 4.13: Distribution and Parameters of Hyperparameters

Variable	range	Intervals
Crack length for four cracks (mm)	0 - 27	0:(27-0)/9:27

Table 4.14: Crack Growth Used in Abaqus FEA Process

with 3 mm increments starting from 0 mm. The combinations of cracks growth are determined with the order of left top, right top, left bottom, right bottom. Due to the symmetric design, the crack growth of left top is set as smaller than the rest three crack growth in generating combinations to avoid duplication. Based on the provided crack lengths, the hexagon frame as well as crack partitions are built to which the material properties are assigned. The Young's modulus for A36 steel is set as 200 GPa with a Poisson's ratio of 0.26, *Matweb* (1999). Then the model is assembled and displacement analysis steps are created. Two reference points are defined and coupled to the surface of bolt holes to simulate the bolts applying displacement and boundary conditions. Then seams are assigned to four cracks and contour integration is defined around each crack tip area. The frame and crack front regions are meshed separately - Quadratic element C3D20 is used for the frame while C3D15 is employed for modeling the crack front regions. The displacement is set as 0.65 mm resulting in 22.05 kN maximum reaction force and 31.8 $Mpa\sqrt{m}$ SIF in the case where four cracks are all 20 mm. Figure 4.14 shows a meshed hexagon specimen generated by the Python script. Each iteration generates an *odb* file storing SIF info around the four crack tip regions which is extracted to build the training dataset containing 310 data points in total. Figure 4.15 shows the SIF from Abaqus analysis with four identical propagated cracks, which indicates the SIF decreases with four cracks growing identically under displacement control.

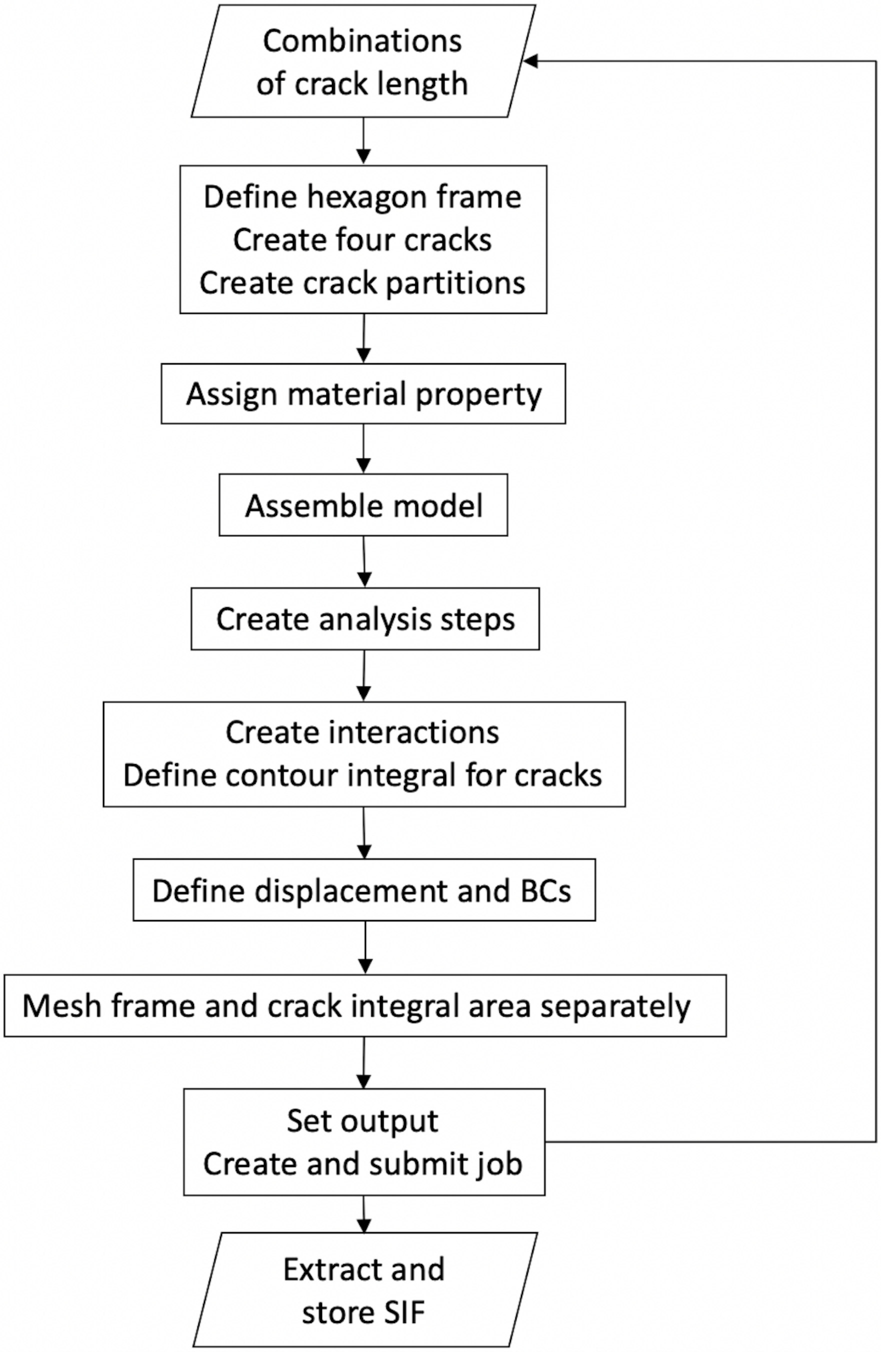

Figure 4.13: FEA process of calculating SIF for hexagon specimen with different combinations of crack length

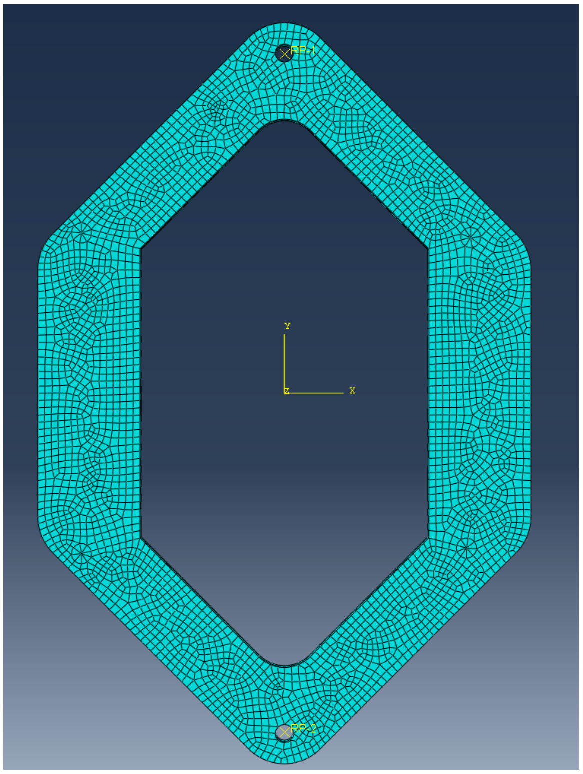

Figure 4.14: A Meshed Hexagon Specimen Modeled from Python Script

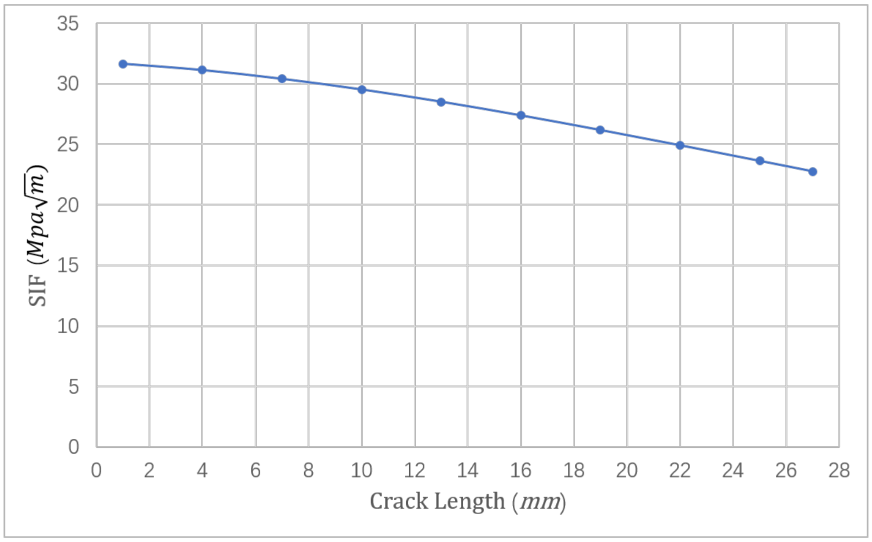

Figure 4.15: SIF from the Abaqus Model with Four Identical Propagated Cracks

4.6.5 Kriging Model: Training, Testing, Application

With the training data obtained from Abaqus models, a Kriging model is trained and applied for predicting SIF with the combinations of four crack lengths as input. The trained Kriging model is used to determine the discretization of SIF and generate the CPT of SIF given combinations of crack lengths. A brief introduction as well as the application of Kriging model is presented in this section.

A Kriging model or Gaussian process regression makes predictions by interpolating values which follows a Gaussian process. The model assumes that the parameter distribution can be represented by a Gaussian process. A training dataset has the format $T = \{\mathbf{Y}, \mathbf{X}\}$ with n points, where X is the matrix containing the features of all training points, i.e. $\mathbf{X} = [\mathbf{x}_1, \mathbf{x}_2, ..., \mathbf{x}_n]^T$, in which $\mathbf{x}_i (i = 1, 2...n)$ is a feature vector for a training point. Y can be seen as a vector storing the target values, i.e. $\mathbf{Y} = [y_1, y_2, ..., y_n]^T$, which is assumed being governed by a multivariate Gaussian distribution. A Gaussian process is defined by the mean μ and the covariance matrix $K(\mathbf{x}, \mathbf{x}')$ between all possible pairs, i.e. $\mathbf{Y} = f(x) \sim N(\mu, K(\mathbf{x}, \mathbf{x}'))$, where μ defines the central tendency which is usually set as 0 and covariance matrix describes the correlations between $\mathbf{x}$ and $\mathbf{x}'$. The value of an observed value y can be seen as the summation of an unknown constant or global trend function $f(x)$ with numerical or experimental error ϵ as shown in Equation 4.12.

$$y = f(x) + \epsilon \tag{4.12}$$

where ϵ is assumed to be independent and identically distributed, i.e. $\epsilon \sim N(0, \sigma^2)$ in which σ^2 is the variance. The likelihood of y given f can be expressed as,

$$p(y|f) = N(y|f, \sigma^2 I) \tag{4.13}$$

where $f = \{f(x_1), f(x_2), ..., f(x_n)\}$ is the response vector with respect to the sample locations. I is a diagonal matrix with dimension $n \times n$. According to *Williams and Rasmussen* (2006), the prior probability of f can be described as a Gaussian distribution with 0 as mean and Gram matrix K,

$$p(f) = N(f|0, K) \tag{4.14}$$

where each entry of K, i.e. $K_{ij} = k(x_i, x_j)$ represents the covariance of two sample points x_i and x_j. Then the probability of y can be acquired by combining Equation 4.13 and Equation 4.14,

$$p(y) = \int p(y|f)p(f)df = N(f|0, K + \sigma^2 I) \tag{4.15}$$

Then given the input vector x_{input}, the joint distribution of predicted vector $y_{predict}$ can be expressed as,

$$\begin{bmatrix} y \\ y_{predict} \end{bmatrix} \sim N\left(0, \begin{bmatrix} K + \sigma^2 I, K_1 \\ K_1^T, \hat{K} + \sigma^2 I \end{bmatrix} \right) \tag{4.16}$$

where K_1 represents the covaraince between predicted and sample points, i.e. $K_1 = [k(x_{input}, x_1), k(x_{input}, x_2), ..., k(x_{input}, x_n)]^T$. $\hat{K}$ describes the covariance of input vector x_{input}.

According to *Williams and Rasmussen* (2006), the covariance are determined by hyperparameters in terms of the best prediction result, which can be acquired based on training data using maximum log-likelihood estimation shown in Equation 4.17, where Θ is the hyperparameter that the Kriging algorithm optimizes so that the likelihood is maximized, n is the dimension of the input variables, *Williams and Rasmussen* (2006).

Method	Metric	Result ($Pa\sqrt{m}$)
10-fold Cross Validation	RMSE	3597.92

Table 4.15: Performance Evaluation of Trained Kriging Model

$$logp(f(x)|\Theta, x) = -\frac{1}{2}f(x)^T K(\Theta, x, x')^{-1} f(x') - \frac{1}{2}log|K(\Theta, x, x')| - \frac{n}{2}log2\pi \quad (4.17)$$

The Kriging model used here is written in Python by *Zhu et al.* (2014). The training dataset is generated from Abaqus models described in Section 4.6.4. The training dataset contains 310 data points where 10 data points are the SIF with all 4 cracks set to the same length at each location while the other 300 data points are the SIF with different crack lengths. The combinations of different crack lengths are generated based on a defined strategy, i.e. the crack growth of left top is set as smaller than the rest three crack growth to avoid duplication. Thus, the training dataset consists of 310 rows and 5 columns where the first four columns are the crack length in the order *left top*, *right top*, *left bottom* and *right bottom.* The last column is the SIF of the left top crack from Abaqus with all cracks modeled at the corresponding size. The performance of trained kriging model is evaluated using 10-fold cross validation with Root Mean Squared Error (RMSE) as the evaluation metric. The 10-fold cross validation divides the training dataset into ten subgroups and use nine subgroups for training while keeping the rest one subgroup for testing. The process is performed 10 times on different subgroups iteratively generating ten errors. The RMSE is averaged on the ten errors to achieve a performance evaluation with relatively low variance, i.e. the RMSE from 10-fold cross validation can represent the performance of trained Kriging model very well. The performance evaluation is summarized in Table 4.15. Considering that the level of SIF is 10^6 $Pa\sqrt{m}$, the RMSE of 3597.92 $Pa\sqrt{m}$ means the model is accurate and suitable for making predictions.

Variable	range	Intervals
Crack length in Abaqus (mm)	0 - 27	0:(27-0)/9:27
Crack length in Numerical Model (mm)	0 - 37	0, 0:19/19:19,22:(37-22)/5:37,∞

Table 4.16: Crack Growth Used in Abaqus FEA Process

As described in Section 4.6.4, due to the integral circle around crack tips, the training data from Abaqus covers the crack growth from 0 mm to 27 mm with 3 mm increment, while the crack growth in numerical model ranges from 0 mm to 37 mm as shown in Table 4.16. The combinations of crack lengths generated by combining the states of crack length in numerical model is used as the input for predictions. The trained Kriging model is employed to make predictions on those combinations of crack lengths. Since the training data contains the SIF of left top crack with combinations of crack lengths ordered as *left top*, *right top*, *left bottom* and *right bottom*, the prediction is the SIF of left top crack with desired crack combinations. In other words, the prediction results and training dataset follow the same format. In the results, when crack lengths are beyond the range of crack lengths covered in training dataset, the prediction tends to be biased. Therefore, a strategy is defined that the predicted SIF is set as 0 when two or more crack lengths are larger than 34mm, i.e. when two or more cracks are about to break, the SIF of left top crack should be very small and set as 0 in prediction results. With the prediction results, a histogram of SIF is plotted in Figure 4.16 from which the states of SIF is determined. The states of SIF is obtained by dividing the histogram into 42 bins and each bin contains the same number of data points. In this way, the discretization of SIF is refined and represent the distribution of SIF properly.

The above process generates a look-up table with combinations of crack lengths in the order of *left top*, *right top*, *left bottom* and *right bottom* and the associated SIF of left top crack. With the look-up table, the CPT of SIF given crack lengths are determined. Due to the discretization, each combination of crack lengths defines

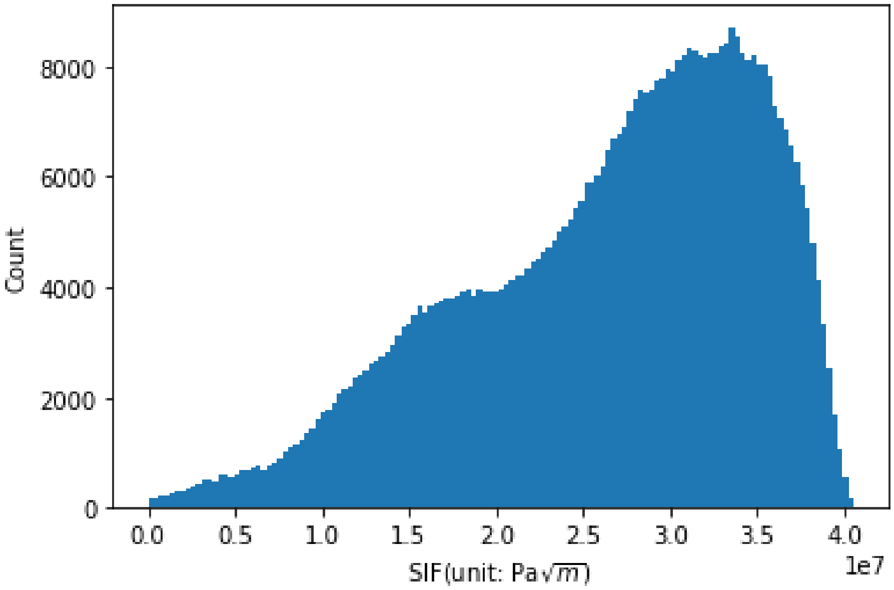

Figure 4.16: Histogram of SIF

a range. If directly using Monte Carlo simulation in each defined range to simulate possible combinations of crack lengths and then employing Kriging model to predict the SIF in term of generating the CPT, the required computation power is impossible to be satisfied. In order to reduce the demand of computation, the look-up table is used to determine the lower and upper bounds of SIF given any combination of crack lengths. The determined lower and upper bounds are used to search the states of SIF which includes these bounds. The conditional probability insides the located states of SIF is determined by uniform distribution while the conditional probabilities outside the states are set as 0. For example, if the states for *left top*, *right top*, *left bottom* and *right bottom* are 9mm-10mm, 7mm-8mm, 15mm-16mm, and 12mm-13mm respectively, then the lower bound of SIF of left top crack can be determined by searching the look-up table for the combination of 9mm, 8mm, 16mm, and 13mm. The upper bound of SIF of left top can be obtained by checking the look-up table for the combination of 10mm, 7mm, 15mm, and 14mm. The SIF of left top crack reaches upper bound when left top crack is the largest in its state while the rest three

Conditional Probability	$SIF_{left\ top}$	$SIF_{right\ top}$	$SIF_{left\ bottom}$	$SIF_{right\ bottom}$
Condition Sequence	$a_{left\ top}$ $a_{right\ top}$ $a_{left\ bottom}$ $a_{right\ bottom}$	$a_{right\ top}$ $a_{left\ top}$ $a_{right\ bottom}$ $a_{left\ bottom}$	$a_{left\ bottom}$ $a_{left\ top}$ $a_{right\ bottom}$ $a_{right\ top}$	$a_{right\ bottom}$ $a_{left\ bottom}$ $a_{right\ top}$ $a_{left\ top}$

Table 4.17: Sequences of Crack Lengths in Determining CPTs of SIF

crack lengths are the smallest in their states. Similarly, the lower bound of SIF of left top crack is obtained with left top crack being the smallest in its state while the rest three crack lengths being largest in their states. This interesting phenomena also indicates the interaction among four cracks.

After having the CPT for SIF of left top crack given the combination of crack lengths of the four cracks, the CPTs for right top, left bottom, and right bottom can be obtained by switching the sequence of parents nodes of SIF due to the symmetrical design, i.e. change the order of cracks. For example, considering the left-right symmetric, the CPT of SIF of left top crack given crack lengths in the order of *left top*, *right top*, *left bottom* and *right bottom* is the same with the CPT of right top crack given crack lengths in the order of *right top*, *left top*, *right bottom* and *left bottom*, i.e. $P(SIF_{left\ top}|a_{left\ top}, a_{right\ top}, a_{left\ bottom}, a_{right\ bottom}) = P(SIF_{right\ top}|a_{right\ top}, a_{left\ top}, a_{right\ bottom}, a_{left\ bottom})$, where a represents crack length. Similarly, the CPTs of SIF of left bottom and right bottom cracks can be determined as summarized in Table 4.17.

4.6.6 Results and Conclusions

The developed model is validated and evaluated on the data collected from the experiment of the fifth hexagon specimen. The gathered data is crack length measured every 100000 cycles until structure failure by machinist scale with respect to applied tension cycles, Table 4.18. The predicted crack length can be treated as time series data and each observation updates the distribution, thus, the prediction from DBN is recorded every time after inputting an evidence, i.e. input the observation from 100000 cycles to 300000 cycles into time slices T1 to T3 and record the prediction for 400000 cycles from time slice T4. The prediction generated by *Hugin* software is a probability table with respect to the defined states of a random variable, which can be exported as a CSV file for further analysis.

Cycles	*Left Top (MS)*	*Left Bottom(MS)*	*Right Top(MS)*	*Right Bottom(MS)*
100000	2.00	2.30	2.65	2.40
200000	5.50	5.50	5.65	4.50
300000	8.25	8.00	8.50	7.50
400000	11.40	11.00	11.75	9.80
500000	13.25	14.10	14.80	11.80
600000	14.70	17.50	19.00	12.60
700000	14.70	23.50	25.00	12.60
800000	14.70	30.75	31.50	12.60
867111	14.70	34.20	37.50	12.60

Table 4.18: Validation Data Collected from the Fifth Hexagon Experiment (unit: *mm*; MS = Machinist Scale)

By combining the updated probabilities with states of crack length, the predicted crack length is calculated as the expectation. Since each states is a discretized range and the predicted probability describe the chance of crack length being in this range, the expectation is obtained by summing the product of each predicted probability with the corresponding center of each state. Even though nine observations are recorded in the fifth hexagon experiment, only eight comparisons are generated in terms of comparing the performance of the developed model with records because the last observation generates no prediction. The first prediction before inputting any evidence comes from the initial states of the system. The comparison between predicted crack length and recorded crack length for four cracks are plotted in Figure 4.17. The predicted crack length is plotted as pink diamonds while the recorded crack length is shown as blue squares. The X axis represents the number of evidence input into the model. In order to display the shadowing effect, the four plot have the same range on Y axis. The variability of the distribution is less than 1 *mm* so the 50% range is not plotted here. As shown in the figure, the prediction for four cracks is slightly biased after only inputting the first evidence, then with more observations, the model adjust itself and makes the overall predictions matching record very well. The biggest challenge in this model is predicting the shadow effect, which means if the network can forecast which crack will be dominant in the degradation process. From the record, we can know that the left bottom and right top crack start to being dominant since 500000 - 600000 cycles, corresponding to the sixth prediction after inputting five evidence. As shown in Figure 4.17a and Figure 4.17d, after inputting five evidence, the model predicts that the crack length of left top and right bottom stops growing while the crack length of left bottom and right top keep growing with a relatively larger growth rate. This results indicate that the developed model is capable to forecast the dominant crack during the deterioration process. This result successfully demonstrate the developed model can simulate the system-level behavior of complex structural system and make accurate predictions. The independent data from experiment evaluates the performance of DBN bringing more confidence in applying DBN to real-world applications.

The updating of SIF is also extracted from CSV file exported from *Hugin*. The data is probabilities with respect to the states of SIF which is plot with bars as shown in Figure 4.18. Each bar is plotted on the center of corresponding state representing a probability. The highest bar means the probability of being in that state is the highest. The width of the bar has no specific meaning. The Y axis for Figure 4.18a and Figure 4.18d have range 0-1 while the Y axis in Figure 4.18b and 4.18c is limited to 0.6 for a clear demonstration. The distribution of the SIF is updated after inputting each observation of crack length. For a clear illustration of updating process, the distribution of SIF after inputting the evidence of 100000, 300000, 500000, 700000, and 867111 cycles are plotted. The distribution after inputting evidence of 867111

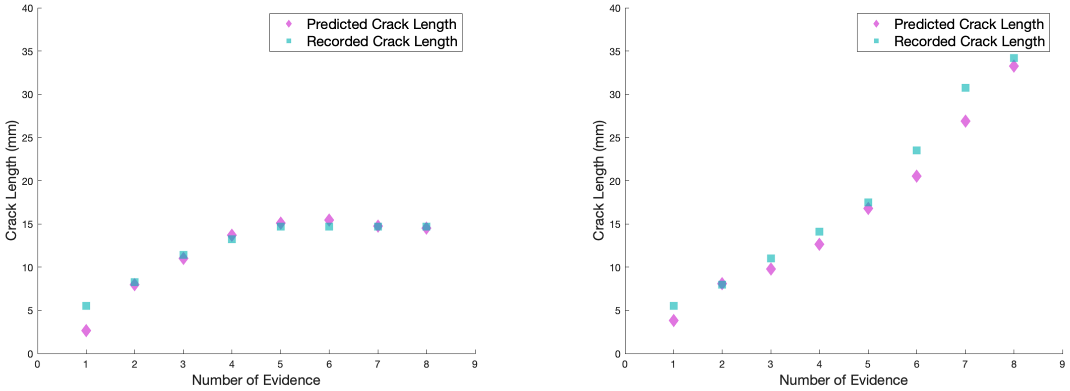

(a) Crack Length of Left Top (b) Crack Length of Left Bottom

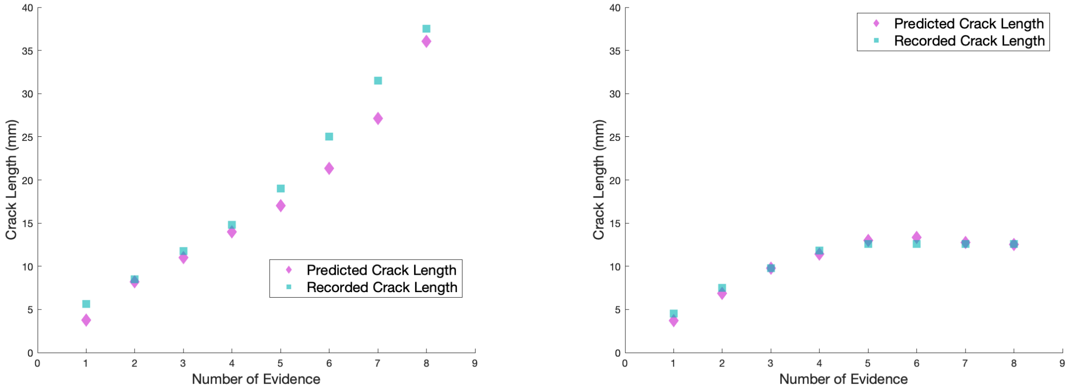

(c) Crack Length of Right Top (d) Crack Length of Right Bottom

Figure 4.17: Predicted Crack Length from the Developed DBN model

cycles is included in terms of investigating the SIF during final structure failure. As shown in Figure 4.18a and Figure 4.18d, the SIF of left top and right bottom crack has similar updating process which matches the fact that these two crack have similar crack propagation in experiment. The SIF of left top and right bottom change slightly before 500000 cycle since the four cracks have similar propagation, i.e. no crack is dominant. This also explains that the SIF of four cracks before 500000 cycles has similar locations indicating a similar SIF. With applying more cycles, the left bottom and right top crack start to take dominant since 500000 cycles, thus, the SIF of left top and right bottom cracks decrease to the range of 20 $MPa\sqrt{m}$ - 25 $MPa\sqrt{m}$ while the SIF of left bottom and right top crack increase due to being dominant. The shadowing effect can be clearly observed from the change of SIF after 500000 cycles, i.e. the left top and right bottom cracks are shadowed by left bottom and right top crack resulting a smaller SIF and slow crack growth, while the dominant cracks have a rapid crack growth due to the increased SIF. The distribution of SIF at 867111 cycles demonstrates the status of structure around the moment of failure. In other words, the left top and right bottom crack have a SIF close to zero while the left bottom and right top crack have their largest SIF around 35 $MPa\sqrt{m}$. It should be noted that the bar of left top and right bottom crack located at 5 $MPa\sqrt{m}$ does not indicate the SIF is 5 $MPa\sqrt{m}$ since the bar is plotted at the center of state. It should be interpreted that the SIF is small enough to fall into the bin with smallest SIF and the model is confident with the prediction since the probability is 1. The updating of SIF clearly demonstrates the status of cracks during degradation process including the shadowing effect, which provides a supplement view for understanding the crack propagation in the experiment.

Usually, the material property are different at different locations of a steel plate. The model includes a hyperparamter of material property m to count for this effect. The updating of material property m is investigated and plotted in Figure 4.19. The

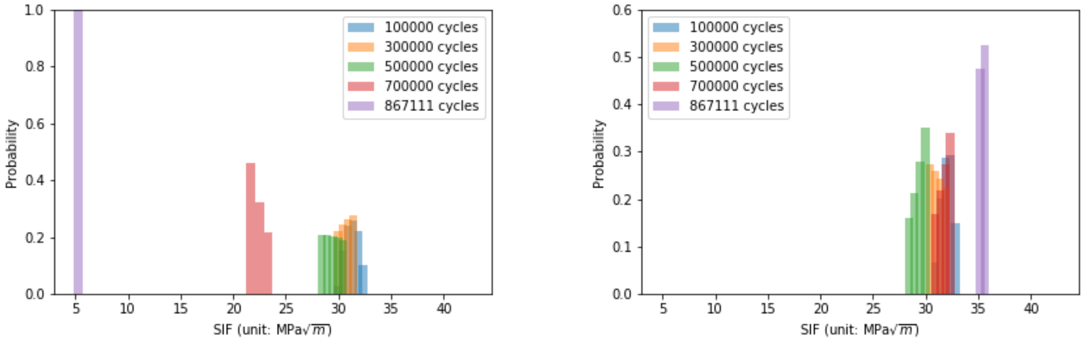

(a) SIF Updating of Left Top

(b) SIF Updating of Left Bottom

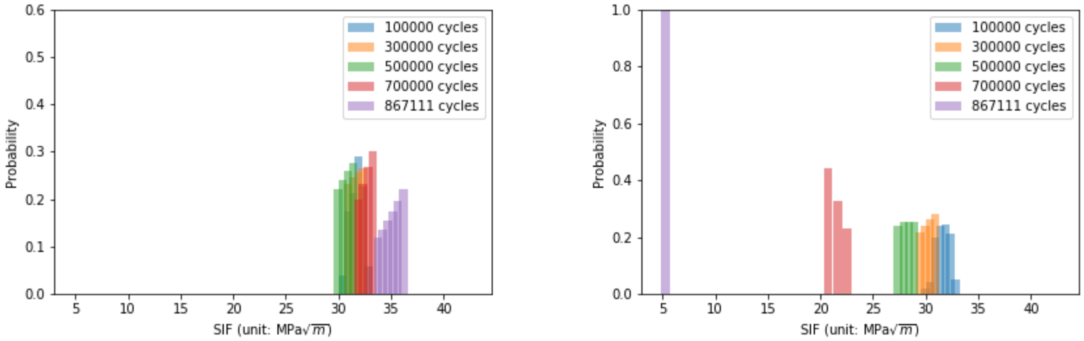

(c) SIF Updating of Right Top

(d) SIF Updating of Right Bottom

Figure 4.18: SIF Updating of Four Cracks from the Developed DBN model

X axis indicates the states of m while the Y axis represents the probability. Since the probability distribution has a bell-shape, quadratic interpolation is applied to achieve a smooth plot. It should be noted that the plot does not represent probability density but probability. For a clear demonstration and considering the fact that material property changes less with increasing number of evidence, the plot includes the probability of m at 100000, 300000, 500000, and 700000 cycles. With one observations of crack length inputted into the model, the material properties m for four are similar with the highest probability around 2.6. With one more observation, the m of four cracks increase with left top and right bottom centered around 2.9 and left bottom and right top centered around 2.75 and 2.85 respectively. This result indicates that the model updates its distribution of m after given more evidence. Beginning from 500000 cycles when the left bottom and right top crack start to take dominant, the model adjusts its predictions for m of the left top and right bottom by decreasing the center of distribution while increasing the prediction for m of the left bottom and right top. In other words, the model estimates that four locations have roughly similar material properties before left bottom and right top crack become dominant, then the model adjusts its estimation due to two dominant cracks by predicting the dominant cracks have larger m than the shadowed cracks. This prediction means that higher m is associated with the area of dominant crack which makes sense. Even the variances of distribution changes slightly which can be improved in future by tuning the hyperparameter of m, the updating still can demonstrate the inference process of DBN with observation of crack lengths.

Compared to the DBN built in Section 4.5, the updated model has a much more accurate prediction of crack length and the ability to forecast the emergence of the dominant crack. The updated model removes the assumption that each crack is a single edge notch in isolation as well as the emperical approximation of SIF. Instead, an Abaqus model and a Kriging model are used to build a look-up table for SIF

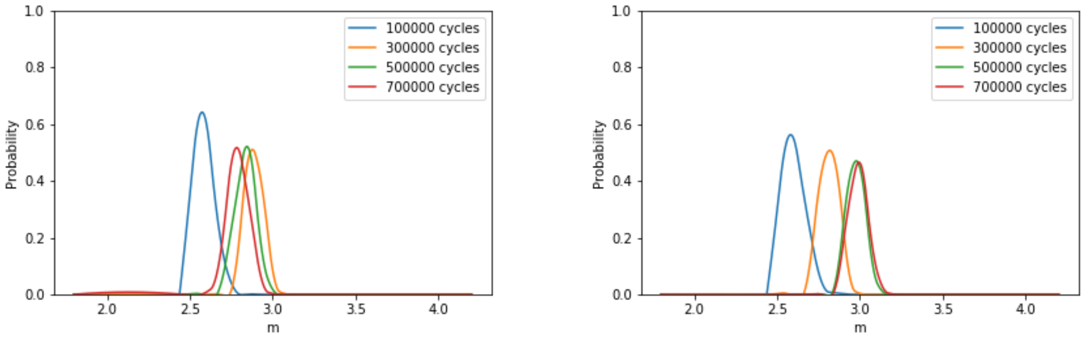

(a) m Updating of Left Top

(b) m Updating of Left Bottom

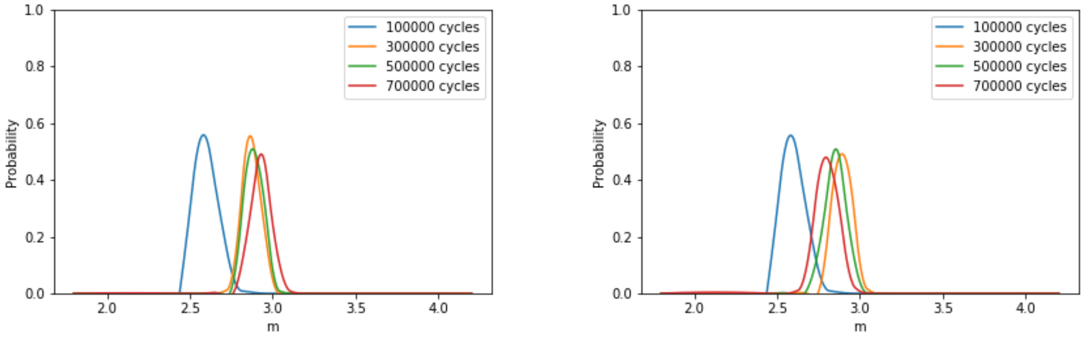

(c) m Updating of Right Top

(d) m Updating of Right Bottom

Figure 4.19: m Updating of Four Cracks from the Developed DBN model

with respect to combinations of four crack lengths increasing the agreement between numerical model and hexagon specimen. Besides connecting four cracks through hyperparameter, the updated model better describes the interaction by including the connection between crack lengths and SIF. The performance of updated model is evaluated by independent experimental data proves the ability of DBN in modeling system-level structural behavior in a degradation process.

4.7 Conclusions

The task of modeling hexagon specimen, a complex structural system, is tackled in this section in four steps. The DBN for a single crack with simulated input validates the fatigue growth model and the updating power of the DBN. Then, the model is expanded to two cracks with the interaction modeled by hyperparameters. As inputting simulated observations, the developed DBN can distinguish the two cracks and make predictions accordingly. The hyperparameter method is applied in modeling the degradation process of hexagon specimen. The prediction performance as well as updating of nominal stress and material property are investigated. Even the model doesn't forecast which crack will become dominant, the model is able to adjust to observations quickly and make acceptable predictions. Finally, an updated model is developed based on Temporal Clone. FEA-based SIFs are used instead of nominal stress and the dependence between crack length and SIF is included. The performance of this model is increased and the prediction matches experiment records very well. The updated model can forecast the dominant crack based on observations of crack length. The successful evaluation of the performance of DBN by independent experimental data lays solid foundation for applying the DBN method in digital twin research.

CHAPTER V

Conclusions

5.1 Summary

The object of this PhD research is to evaluate the performance of DBN in modeling system-level structural degradation using independent experimental data. This work is done to refine the concept of digital twins, by providing the community with both a dataset for future model validation as well as an explicit investigation into the power of DBNs. By selecting crack propagation to characterize the structure deterioration, a lab-level experiment was designed and conducted to collect crack length and maximum reaction force associated with applied tension cycles. The laboratory experiment aimed to simulate several properties of real-world complex marine structures including structure redundancy, component dependence, and component-to-system integration. A diamond-shaped specimen was designed initially followed by a upgraded hexagon-shaped design. Two new methods were developed for measuring crack length based on computer vision and DIC technology, which could be applied to structures for measuring crack length in terms of monitoring the structural health. The performance of computer vision based method was evaluated by a standard eccentrically-loaded single edge crack tension specimen. Five hexagon specimens were machined and tested using a MTS 810 material testing system. The first two experiments focused on validating the design and the developed methods for measuring crack length. In the third experiment, strain gauges were deployed to monitor the structural status in degradation process. All the developed methods measuring crack length as well as strain gauge monitoring system were employed in the fourth and fifth experiment of hexagon specimen. The recorded crack length and maximum reaction force proved that the design successfully reflected the properties of real-world complex structural system. The gathered data from the experiment is not only employed to evaluate the performance of DBN model but also support the exploration and research of future digital twin approaches.

Based on DBN, a numerical model simulating the structural degradation was built and evaluated with the independent data from the hexagon experiment. First, the propagation of a single crack was modeled using a DBN and evaluated with simulated evidence of crack length, which verified the capability of the DBN in modeling crack growth of individual components. Then, the concept of hyperparameters was introduced to deal with crack propagation on two interacting components. The dependence between cracks was modeled through a stress hyperparameter. The model was able to distinguish the two cracks when provided with simulated observations. Then a DBN model with hyperparameters was built to simulate the degradation process of the hexagon specimen. The four cracks were modeled as single edge notch and connected through hyperparameter of nominal stress and material property m. The performance of developed DBN was evaluated with observations collected from the hexagon experiment. Even though the model had a relatively large prediction of crack growth, its prediction was able to match the trend of observed crack length. This model was unable to forecast the dominant crack and shadowing effect among cracks, but it could still adjust with evidence quickly in terms of making accurate predictions. The updating of nominal stress and material property m was investigated to understand the structure's status. The nominal stress and material property were able to reflect the difference between dominant and shadowed cracks. Finally, an updated model was developed by adding the connections between crack length and SIF which was missing in the former model. The corresponding CPT of SIF with respect to crack length was obtained through a batch of Abaqus modeling with Python script and a Kriging model. In addition to the dependence between crack length and SIF, the model also included a hyperparameter of material property m. This model predicted crack length based on observations which matched the experiment data very well. Compared to the previous model, the updated model was able to foresee the dominant crack and predicted the shadowing effect successfully. The capability of DBN in modeling system-level structural degradation was clearly demonstrated through this investigation, which used independent, physical crack growth data in place of simulated growth data.

5.2 Contributions

The contribution of this work can be summarized in the following points,

- A laboratory scale experiment, with acceptable expense and short time span, has been designed and conducted to mimic the key characteristics of much larger marine structural systems, including component dependence, structural redundancy, and component-to-system integration.
- Two new methods have been developed for measuring crack length based on computer vision and DIC. The novel computer vision method, developed and initially validated in this work, can approximate crack lengths rapidly on complex structural specimens with multiple cracks.
- A large experimental dataset, capturing complex system-level dynamics of the structure system, has been generated from the tests for demonstrating digital twin methodologies and supporting the exploration of future digital twin models.

- Four different DBN modeling strategies for crack growth problems have been investigated from single crack to multiple cracks, simulated data to independent experiment data, laying solid foundation for applying the DBN method in digital twin research.

- A new high-fidelity system-level DBN approach, using a mix of FEA analysis and Kriging models to model component interaction during the degradation of a complex system, has been developed in this work, delivering an accurate prediction of crack growth in the degradation of complex structural system.

- The performance of the developed model is verified by independent data serving as the first marine-specific assessment of a structural digital twin against independent experimental dataset.

5.3 Recommendations for Future Work

The recommendations for future works are summarized as follows,

- The developed methods for crack length measurement should be investigated in terms of automation. The computer vision based method can be automated regarding cropping images and matching pixel distance to real-world length. The DIC based method can be improved by automatically defining region of interest and determining the turning point in terms of finding crack length. The DIC method can be further expanded regarding locating the crack tip.

- The DBN updating accuracy could potentially be improved by including more hyperparameters to describe the correlations better. Tuning hyperparameters is also a key points in terms of increasing the model performance.

- Refined discretization of random variables is promising in enhancing model performance. However, increasing number of states can increase the computation demands exponentially. Thus, the optimized discretization of random variables can be further investigated aiming to find a balance between accuracy and computation cost.

- The state space explosion problem could potentially be reduced by exploring a more concise approach to model the SIF interactions, such as a single parameter instead of using all crack lengths.

- A common difficulty of DBNs in modeling complex structural system is the size of CPTs grows exponentially with increasing number of states and complex dependence, resulting in a slow inference. A potential approach employing API and more computation power could be investigated in terms of speeding up the inference and making a faster real-time prediction.

- The strain gauge data collected from the experiment, as well as the resisting force gathered during the test, can be explored to improve the DBN updating accuracy.

- The comparison of future reliability predictions between the developed DBN network in this work and other proposed structural reliability methods can be further explored and summarized.

- The experiment can be expanded by including corrosion to reflect the real-world structure degradation better.

- The developed DBN can be explored and expanded to Influence Diagram to assist in making decisions in term of optimized maintenance strategy.

BIBLIOGRAPHY

BIBLIOGRAPHY

Abaei, M. M., R. Abbassi, V. Garaniya, S. Chai, and F. Khan (2018), Reliability assessment of marine floating structures using Bayesian network, *Applied Ocean Research*, *76*, 51–60, doi:10.1016/J.APOR.2018.04.004.

Andersen, S. K., K. G. Olesen, F. V. Jensen, and F. Jensen (1989), Hugin-a shell for building bayesian belief universes for expert systems., in *IJCAI*, vol. 89, pp. 1080–1085.

Anderson, T. L. (2005), *Fracture mechanics: fundamentals and applications*, CRC press.

ASTM, E. (2008), Standard test method for crack-tip opening displacement (ctod) fracture toughness measurement.

ASTM, I. (2011), *Standard test method for measurement of fatigue crack growth rates*, ASTM International.

Bhandari, J., F. Khan, R. Abbassi, V. Garaniya, and R. Ojeda (2017), Pitting Degradation Modeling of Ocean Steel Structures Using Bayesian Network, *Journal of Offshore Mechanics and Arctic Engineering*, *139*(5), 051,402, doi:10.1115/1.4036832.

Boyen, X., and D. Koller (1998), Tractable inference for complex stochastic processes, in *Proceedings of the Fourteenth conference on Uncertainty in artificial intelligence*, pp. 33–42, Morgan Kaufmann Publishers Inc.

Brauser, S., L.-A. Pepke, G. Weber, and M. Rethmeier (2010), Deformation behaviour of spot-welded high strength steels for automotive applications, *Materials Science and Engineering: A*, *527*(26), 7099–7108.

Dagum, P., A. Galper, and E. Horvitz (1992), Dynamic network models for forecasting, in *Proceedings of the eighth international conference on uncertainty in artificial intelligence*, pp. 41–48, Morgan Kaufmann Publishers Inc.

Ditlevsen, O., and H. O. Madsen (1996), *Structural reliability methods*, vol. 178, Wiley New York.

Doshi, K., and S. Vhanmane (2013), Probabilistic fracture mechanics based fatigue evaluation of ship structural details, *Ocean Engineering*, *61*, 26–38.

Du, Y., F. Diaz, R. Burguete, and E. Patterson (2011), Evaluation using digital image correlation of stress intensity factors in an aerospace panel, *Experimental Mechanics*, *51*(1), 45–57.

Earnshaw, P., and J. Lawford (1966), *Low-speed wind-tunnel experiments on a series of sharp-edged delta wings*, HM Stationery Office London.

Garbatov, Y., and C. G. Soares (2012), Uncertainty assessment of fatigue damage of welded ship structural joints, *Engineering structures*, *44*, 322–333.

Gordo, J. M., and C. G. Soares (2008), Compressive tests on short continuous panels, *Marine Structures*, *21*(2-3), 113–137.

Hugin Expert, A. (), S (2012) hugin api reference manual, version 7.6, *Hugin Expert A/S, Aalborg, Denmark.*

Jensen, F., U. B. Kjærulff, M. Lang, and A. L. Madsen (2005), Hugin-the tool for bayesian networks and influence diagrams, in *Probabilistic Graphical Models*, pp. 212–221.

Jensen, F. V., and F. V. (1996), *An introduction to Bayesian networks*, 178 pp., Springer.

Kahle, D., T. Savitsky, S. Schnelle, and V. Cevher (2008), JUNCTION TREE ALGORITHM.

Khan, R. A., and S. Ahmad (2010), Probabilistic fatigue safety analysis of oil and gas risers under random loads, in *ASME 2010 29th international conference on ocean, offshore and arctic engineering*, pp. 345–352, American Society of Mechanical Engineers Digital Collection.

Kimoto, K., S. Ueno, and S. Hirose (2006), Image-based sizing of surface-breaking cracks by sh-wave array ultrasonic testing, *Ultrasonics*, *45*(1-4), 152–164.

Kjærulff, U. (1995), dhugin: A computational system for dynamic time-sliced bayesian networks, *International journal of forecasting*, *11*(1), 89–111.

Koller, D., and N. Friedman (2009), *Probabilistic graphical models: principles and techniques*, MIT press.

Korb, K. B., and A. E. Nicholson (2010), *Bayesian Artificial Intelligence, Second Edition*, 2nd ed., CRC Press, Inc., Boca Raton, FL, USA.

Kwon, K., D. M. Frangopol, and M. Soliman (2011), Probabilistic fatigue life estimation of steel bridges by using a bilinear s-n approach, *Journal of Bridge Engineering*, *17*(1), 58–70.

Lee, D., H. Tippur, M. Kirugulige, and P. Bogert (2009), Experimental study of dynamic crack growth in unidirectional graphite/epoxy composites using digital image correlation method and high-speed photography, *Journal of composite materials*, *43*(19), 2081–2108.

Lee, J.-u. (2018), Application of strain gauge method for investigating influence of ship shaft movement by hydrodynamic propeller forces on shaft alignment, *Measurement*, *121*, 261–275.

Li, C., and S. Mahadevan (2018), Efficient approximate inference in bayesian networks with continuous variables, *Reliability Engineering & System Safety*, *169*, 269–280.

Liu, M., Y. Gan, D. A. Hanaor, B. Liu, and C. Chen (2015), An improved semi-analytical solution for stress at round-tip notches, *Engineering fracture mechanics*, *149*, 134–143.

Liu, P.-L., and A. Der Kiureghian (1986), Multivariate distribution models with prescribed marginals and covariances, *Probabilistic Engineering Mechanics*, *1*(2), 105–112.

Longo, R., S. Vanlanduit, J. Vanherzeele, and P. Guillaume (2010), A method for crack sizing using laser doppler vibrometer measurements of surface acoustic waves, *Ultrasonics*, *50*(1), 76–80.

Lu, N., M. Noori, and Y. Liu (2016), Fatigue reliability assessment of welded steel bridge decks under stochastic truck loads via machine learning, *Journal of Bridge Engineering*, *22*(1), 04016,105.

Luque, J., and D. Straub (2016), Reliability analysis and updating of deteriorating systems with dynamic bayesian networks, *Structural Safety*, *62*, 34–46.

Madsen, A. L., F. Jensen, U. B. Kjaerulff, and M. Lang (2005), The hugin tool for probabilistic graphical models, *International Journal on Artificial Intelligence Tools*, *14*(03), 507–543.

Maes, M. (2003), Modelling Infrastructure Deterioration Risks Using Bayesian Mixtures, *International Journal of Modelling and Simulation*, *23*(1), 43–51, doi: 10.1080/02286203.2003.11442254.

Maes, M. A., and M. Dann (2007), Hierarchical Bayes methods for systems with spatially varying condition states, doi:10.1139/L07-049.

Maes, M. A., M. R. Dann, K. W. Breitung, and E. Brehm (2008), Hierarchical modeling of stochastic deterioration, in *Proceedings of the 6th International Probabilistic Workshop, CA Graubner, H. Schmidt, D. Proske, TU Darmstadt, eds*, pp. 111–124.

Matweb (1999), Properties of ASTM A36 steel, plate.

Monsalve-Giraldo, J., C. Dantas, and L. Sagrilo (2016), Probabilistic fatigue analysis of marine structures using the univariate dimension-reduction method, *Marine Structures*, *50*, 189–204.

Murphy, K. P. (1994), Dynamic Bayesian Networks: Representation, Inference and Learning, *Tech. rep.*

Murphy, K. P. (2001), An introduction to graphical models, *Tech. rep.*

Nakamura, S., and K. Suzumura (2012), Experimental study on fatigue strength of corroded bridge wires, *Journal of Bridge Engineering*, *18*(3), 200–209.

Nixon, M., and A. S. Aguado (2012), *Feature extraction and image processing for computer vision*, Academic Press.

Peters, W., and W. Ranson (1982), Digital imaging techniques in experimental stress analysis, *Optical engineering*, *21*(3), 213,427.

Pohler, C., A. Stavovy, J. Beach, and F. Borriello (1979), A technology base for aluminum ship structures, *Naval Engineers Journal*, *91*(5), 33–44.

Rabiei, E., E. L. Droguett, and M. Modarres (2016), A prognostics approach based on the evolution of damage precursors using dynamic bayesian networks, *Advances in Mechanical Engineering*, *8*(9), 1687814016666,747.

Resch, M., D. Nelson, H. Yuce, and G. Ramusat (1985), A surface acoustic wave technique for monitoring the growth behavior of small surface fatigue cracks, *Journal of Nondestructive Evaluation*, *5*(1), 1–7.

Ritch, R., R. Frederking, M. Johnston, R. Browne, and F. Ralph (2008), Local ice pressures measured on a strain gauge panel during the ccgs terry fox bergy bit impact study, *Cold Regions Science and Technology*, *52*(1), 29–49.

Rosenberg, A. (2010), Lecture 10: Junction Tree Algorithm CSCI 780 -Machine Learning.

Rossini, M., P. R. Spena, L. Cortese, P. Matteis, and D. Firrao (2015), Investigation on dissimilar laser welding of advanced high strength steel sheets for the automotive industry, *Materials Science and Engineering: A*, *628*, 288–296.

Saad-Eldeen, S., Y. Garbatov, and C. G. Soares (2012), Effect of corrosion degradation on ultimate strength of steel box girders, *Corrosion Engineering, Science and Technology*, *47*(4), 272–283.

Saad-Eldeen, S., Y. Garbatov, and C. Guedes Soares (2013), Experimental assessment of corroded steel box-girders subjected to uniform bending, *Ships and Offshore Structures*, *8*(6), 653–662.

Saad-Eldeen, S., Y. Garbatov, and C. G. Soares (2016a), Experimental strength analysis of steel plates with a large circular opening accounting for corrosion degradation and cracks subjected to compressive load along the short edges, *Marine Structures*, *48*, 52–67.

Saad-Eldeen, S., Y. Garbatov, and C. G. Soares (2016b), Ultimate strength analysis of highly damaged plates, *Marine Structures*, *45*, 63–85.

Sabra, K. G., and S. Huston (2011), Passive structural health monitoring of a high-speed naval ship from ambient vibrations, *The Journal of the Acoustical Society of America*, *129*(5), 2991–2999.

Saenz, E. E., L. A. Carlsson, G. C. Salivar, and A. M. Karlsson (2014), Fatigue crack propagation in polyvinylchloride and polyethersulfone polymer foams, *Journal of Sandwich Structures & Materials*, *16*(1), 42–65.

Schirmann, M., C. Wincott, J. Gose, and M. Collette (2018), Exploration of algorithms and frameworks for surface platform digital twins, *Naval Engineers Journal*, *130*(3), 66–68.

Schleich, B., N. Anwer, L. Mathieu, and S. Wartzack (2017), Shaping the digital twin for design and production engineering, *CIRP Annals*, *66*(1), 141–144.

Schneider, R., S. Thöns, and D. Straub (2017), Reliability analysis and updating of deteriorating systems with subset simulation, *Structural Safety*, *64*, 20–36.

Shapiro, L. G., and G. Stockman (2001), Computer vision: Theory and applications.

Sobel, I., and G. Feldman (1968), A 3x3 Isotropic Gradient Operator for Image Processing, never published but presented at a talk at the Stanford Artificial Project.

Souza, G., and B. Ayyub (2000), Probabilistic fatigue life prediction for ship structures using fracture mechanics, *Naval engineers journal*, *112*(4), 375–397.

Stewart, M. G., and J. A. Mullard (2007), Spatial time-dependent reliability analysis of corrosion damage and the timing of first repair for RC structures, *Engineering Structures*, *29*(7), 1457–1464, doi:10.1016/J.ENGSTRUCT.2006.09.004.

Straub, D. (2009), Stochastic modeling of deterioration processes through dynamic bayesian networks, *Journal of Engineering Mechanics*, *135*(10), 1089–1099.

Süli, E., and D. F. Mayers (2003), *An introduction to numerical analysis*, Cambridge university press.

Sutton, M., J. Turner, Y. Chao, H. Bruck, and T. Chae (1992), Experimental investigations of three-dimensional effects near a crack tip using computer vision, *International journal of fracture*, *53*(3), 201–228.

Sutton, M. A., J. Yan, X. Deng, C.-S. Cheng, and P. Zavattieri (2007), Three-dimensional digital image correlation to quantify deformation and crack-opening displacement in ductile aluminum under mixed-mode i/iii loading, *Optical Engineering*, *46*(5), 051,003.

Vrouwenvelder, T. (2004), Spatial correlation aspects in deterioration models, in *Proceedings 2nd International Conference on Lifetime-Oriented Design Concepts*.

Weber, P., G. Medina-Oliva, C. Simon, and B. Iung (2012), Overview on Bayesian networks applications for dependability, risk analysis and maintenance areas, *Engineering Applications of Artificial Intelligence*, *25*(4), 671–682, doi: 10.1016/J.ENGAPPAI.2010.06.002.

Williams, C. K., and C. E. Rasmussen (2006), *Gaussian processes for machine learning*, vol. 2, MIT press Cambridge, MA.

Wong, K.-Y. (2004), Instrumentation and health monitoring of cable-supported bridges, *Structural control and health monitoring*, *11*(2), 91–124.

Xu, M. C., and C. G. Soares (2013), Experimental study on the collapse strength of wide stiffened panels, *Marine Structures*, *30*, 33–62.

Zhu, J., Y.-J. Wang, and M. Collette (2014), A multi-objective variable-fidelity optimization method for genetic algorithms, *Engineering Optimization*, *46*(4), 521–542.

Zhu, J., W. Zhang, and X. Li (2019), Fatigue damage assessment of orthotropic steel deck using dynamic bayesian networks, *International Journal of Fatigue*, *118*, 44–53.